Novel Composite Hydrogen-Permeable Membranes for Nonthermal Plasma Reactors for the Decomposition of Hydrogen Sulfide

Final Report
REVISED

October 1, 2003
September 30, 2007

Morris D. Argyle
John F. Ackerman
Suresh Muknahallipatna
Jerry C. Hamann
Stanislaw Legowski
Gui-Bing Zhao
Sanil John
Ji-Jun Zhang
Linna Wang

December 29, 2007
REVISED March 4, 2008

DE-FC26-03NT41963

University of Wyoming
Department of Chemical and Petroleum Engineering
Department of Electrical and Computer Engineering
Dept. 3295
1000 East University Avenue
Laramie, WY 82071

Disclaimer

Abstract

The goal of this experimental project was to design and fabricate a reactor and membrane test cell to dissociate hydrogen sulfide (H_2S) in a nonthermal plasma and to recover hydrogen (H_2) through a superpermeable multi-layer membrane. Superpermeability of hydrogen atoms (H) has been reported by some researchers using membranes made of Group V transition metals (niobium, tantalum, vanadium, and their alloys), but it was not achieved at the moderate pressure conditions used in this study. However, H_2S was successfully decomposed at energy efficiencies higher than any other reports for the high H_2S concentration and moderate pressures (corresponding to high reactor throughputs) used in this study.

Several pulsed corona discharge (PCD) reactors were fabricated and used during this project. Prior to experiments involving H_2S, methane (CH_4) was used as a non-toxic reactant to evaluate the performance of the reactor. These experiments were also valuable for determining the potential to co-process H_2S and CH_4 as a method of sweetening natural gas. The products of the direct methane conversion experiments included hydrogen, acetylene, and higher hydrocarbons. The reactor was a co-axial cylinder (CAC) corona discharge reactor, pulsed with a thyratron switch. The reactor was designed to accommodate relatively high flow rates (655×10^{-6} m^3/s), representing a pilot scale easily converted to commercial scale. Parameters expected to influence methane conversion, including pulse frequency, charge voltage, capacitance, residence time, and electrode material, were investigated. Conversion, selectivity and energy consumption were measured or estimated. C_2 and C_3 hydrocarbon products were analyzed with a mass spectrometer (MS). Methane conversions as high as 51% were achieved. The products were typically 50-60% acetylene, 20% propane, 10% ethane and ethylene, and 5% propylene. First law thermodynamic energy efficiencies for the system (electrical and reactor) were estimated to range from 6 to 38%, with the highest efficiencies occurring at short residence time and low power input (low specific energy), where conversion is the lowest (less than 5%). The highest methane conversion of 51% occurred at a residence time of 18.8 s with a flow rate of $39.4\times10^{-6}m^3/s$ (5 ft^3/h) and a specific energy of 13,000 J/l using niobium and platinum coated stainless steel tubes as cathodes. Under these conditions, the first law efficiency for the system was 8%. Under similar reaction conditions, methane conversions were ~50% higher with niobium and platinum coated stainless steel cathodes than with a stainless steel cathode.

The effect of capacitance, cathode material, gas flow rate (residence time) and specific energy on methane conversion, energy efficiency and product selectivity were all examined during the methane experiments. Ethane and acetylene appeared to be formed primarily from dimerization of CH_3 radicals and CH radicals, respectively, while ethylene appeared to be formed mainly from the dehydrogenation of ethane. At the same power input, low capacitance with high pulse frequency is more advantageous for methane conversion and energy efficiency than operation at high capacitance with low pulse frequency. A platinum coated stainless steel cathode resulted in a weak catalytic effect on methane conversion. The activation energies for plasma methane conversion using stainless steel, platinum coated stainless steel, and niobium tubes were nearly the same. With increasing specific energy input, the energy efficiency for methane conversion has a minimum value, while the selectivity of acetylene has a maximum value. Comparison of methane conversion for different types of plasma reactors shows that the pulsed corona discharge is a promising alternative method for methane conversion at low

temperature. The different electrical properties and plasma reaction behaviors of CH_4 and H_2S suggest that the co-processing of sour natural gas to selectively remove sulfur may not be feasible with this type of pulsed corona discharge reactor. However, these methane experiments provided valuable insight on the interrelation among the reactor operating parameters that were advantageous to the H_2S decomposition experiments that were conducted for the remainder of the project.

This pulsed corona discharge (PCD) reactor was used to dissociate H_2S into hydrogen and sulfur. With this reactor, a nonthermal plasma could not be produced in pure H_2S, even at discharge voltages of up to 30 kV, because of the high dielectric strength of pure H_2S (~2.9 times higher than air). Therefore, H_2S was diluted in another gas with a lower breakdown voltage (or dielectric strength). Breakdown voltages of H_2S in four balance gases (Ar, He, N_2 and H_2) were measured at different H_2S concentrations and pressures. Breakdown voltages are proportional to the partial pressure of H_2S and the balance gas. H_2S conversion and the reaction energy efficiency depend on the balance gas and H_2S inlet concentrations. With increasing H_2S concentrations, H_2S conversion initially increases, reaches a maximum, and then decreases. H_2S conversion in atomic balance gases, such as Ar and He, is more efficient than that in diatomic balance gases, such as N_2 and H_2. These observations can be explained by a proposed reaction mechanism of H_2S dissociation in different balance gases. The results show that nonthermal plasmas are effective for dissociating H_2S into hydrogen and sulfur. Visual observation shows that the corona is not uniform throughout the reactor. The corona is stronger near the top of the reactor in argon, while nitrogen and mixtures of argon or nitrogen with H_2S produce stronger coronas near the bottom of the reactor. Both of these effects appear to be explainable base on the different electron collision interactions with monatomic versus polyatomic gases.

A series of experiments varying reactor operating parameters, including discharge voltage, discharge capacitance, and pulse frequency at constant reactor power input, mixtures of balance gases (argon and nitrogen), reactant flow rate and direction, and pulse waveform all show optimization potential for future reactor design and operation. At constant reactor power input (100 W), low capacitance, high pulse frequency, and low voltage operation appear to provide the highest conversion and the highest energy efficiency for H_2S decomposition, similar to the results obtained with methane as the reactant. The trigger waveform of the pulse appears to have a significant effect on H_2S conversion. Nearly all of the experiments in this study were conducted with square waveforms, but recent data indicate that a sinusoidal waveform may be more advantageous. While monatomic gases, such as argon, appear to be the best single diluents, mixtures of argon and nitrogen may produce even higher H_2S conversions and energy efficiencies. Reactor throughput studies that varied the flow rate through the reactor indicate that there is a trade-off between reactor throughput and energy efficiency. Although higher energy efficiencies are obtained at higher flow rates, lower conversions are also achieved, resulting in the need for larger reactors and higher recycle rates. There will be an economic optimum between lower operating costs resulting from the higher energy efficiency operation and the higher capital cost resulting from higher flow rates. Finally, flow direction relative to the direction of gravity does not appear to be an important operating parameter.

A metal infiltrated porous ceramic membrane was prepared using vanadium as the metal and an alumina tube. Experiments with this type of membrane, as well as with pure niobium and

thermal stainless steel and platinum coated stainless steel membranes showed no plasma driven permeation or superpermeability. A small test cell with a continuous plasma discharge was designed and constructed to test the membranes and to provide basic science data on superpermeability. No hydrogen permeation was observed in this cell, even under a variety of thermal and plasma conditions that should have produced significant amounts of atomic hydrogen. Superpermeability appears to occur only at very high vacuum conditions with specially prepared membrane surfaces.

Table of Contents

List of Graphical Materials

List of Tables

Introduction

Gas streams containing hydrogen sulfide (H_2S) are encountered in almost all current and potential-fossil fuel based energy extraction and processing systems. Examples of such streams include:

- Sour gas (>5.7 mg H_2S/m^3 natural gas) in the natural gas industry;[1]
- Effluent gas streams from hydrodesulfurization units in the petroleum refining industry;
- Product gas streams from gasification of coal;[2]
- Hydrothermal gas vent streams from the ocean floor;[3] and
- Geothermal and volcanic sources.[4]

As an example, the map in Figure 1 shows major natural gas sources containing H_2S in the United States.

Figure 1. Major H_2S-containing natural gas reservoirs in the continental United States[5]

Between 15 to 25 percent of natural gas in the United States may contain hydrogen sulfide,[5] while worldwide, the figure could be as high as 30 percent. The exact number of sour wells in the United States is not known, though natural gas deposits in Arkansas, southeastern New Mexico, western Texas, and north-central Wyoming have been identified as sour.[5] Hydrogen sulfide occurs naturally in the geologic formations in the Rocky Mountains, the midcontinent, the Permian Basin, and the Michigan and Illinois Basins.[5] As more natural gas development occurs in these areas, the number of sour wells will likely increase because new drilling is increasingly focused on deep gas formations that tend to be sour.[5]

H_2S must be removed from natural gas because of its extreme toxicity and corrosivity. At natural gas processing facilities, the sour gas is passed through a solvent that absorbs the H_2S but not the hydrocarbons (natural gas). The solvent is then heated, driving the H_2S from the solution. The most common solvents are functionalized amines, which are organic derivatives of ammonia. The process tends to be energy intensive.

The conventional treatment method for H_2S is the Claus process, which produces elemental sulfur and water by the net reaction: $H_2S + O_2 \rightarrow S + H_2O$. The reaction is inefficient because the valuable potential product hydrogen (H_2) is converted into water. The transformation of hydrogen in a weakly bound state in H_2S to a strongly bound state in H_2O results in the loss of a potential source of H_2. Hydrogen sulfide would have a much higher economic value if both sulfur and chemically pure hydrogen could be recovered instead of merely sulfur. Therefore, processes for direct dissociation of H_2S into H_2 and sulfur are desirable.

Many methods have been investigated to dissociate H_2S into its constituent elements, including thermal decomposition, both noncatalytic and catalytic, electrochemical methods,

photochemical processes, and plasma methods.[6] Compared to electrochemical and photochemical methods, thermal decomposition and plasma decomposition are promising because of relatively low energy consumption.[7] However, the thermal decomposition reaction of H_2S is endothermic, with low equilibrium conversions even at high temperatures.[8] For example, thermal decomposition of H_2S has an equilibrium conversion of 12% at 1273 K (1000°C) and 1 atmosphere pressure and that decreases to less than 1% at temperatures below 823 K (550°C). Therefore, two methods have been proposed to overcome the thermodynamic limitation of H_2S conversion. One is product removal by condensation of the sulfur and separation of the hydrogen with membranes.[6] The other is creation of a nonthermal equilibrium environment for H_2S conversion, as found in nonthermal plasmas. Nonthermal plasmas are characterized by low gas temperature and high electron temperature wherein high energy electrons are produced in the gas while the bulk temperature of the gas is unchanged. Nonthermal plasma is a partially ionized gas that provides a source of chemically active species, including radicals, excited neutrals, and ions, which can promote chemical reactions at ambient temperatures. Therefore, nonthermal plasmas overcome the disadvantage of the need for high temperatures because the majority of the electrical energy goes into the production of energetic electrons rather than into gas heating. For reactions that are thermodynamically unfavorable and for which low equilibrium conversions are obtained even at high reaction temperatures, nonthermal plasmas have an advantage over thermal processes because thermal equilibrium is not required to be achieved.

A Pulsed Corona Discharge Reactor (PCDR) was chosen to investigate H_2S conversion because (1) PCD plasmas have been extensively investigated and used in methane[12] and NO_x conversion[10,11,12,13] and (2) comparison of energy efficiency of methane conversion among three

types of nonthermal plasma reactors (PCD, microwave, and silent discharge) shows that PCD reactors are one to two orders of magnitude more energy efficient than the other two.[14]

As discussed previously, plasmas are a source of radicals, ions, and excited atoms and molecules. H_2S decomposition in our plasma reactor forms H atoms because the average electron energy in corona discharges (10 eV) is greater than the dissociation energy for hydrogen molecules (4.4 eV) and the energy for direct electron collision dissociation of H_2S (~4eV). Both of these processes form H atoms. Metal membranes have been reported to be superpermeable to H atoms in a process called plasma-driven permeation. There is a substantial increase in the permeation flux through a metallic membrane exposed to an incident flux of hydrogen atoms compared to an equivalent flux of hydrogen molecules.[15] However, this process has only been reported at relatively high vacuum conditions (pressures of a few torr or less).[15] One of the hypotheses of this project was that superpermeability could be produced at higher pressures. High-purity hydrogen could be produced in our reactor by if the cathode or the anode were a superpermeable metallic membrane.

References

1. http://www.naturalgas.org/naturalgas/processing_ng.asp#sulphur
2. Abbasian, J.; Rehmat, A.; Leppin, D.; Banerjee, D.D., 1990. H_2S removal from fuel gas during coal gasification. Preprints ACS – Fuel Chem Div., 35, 196.
3. Pace, N.R., 1997. A Molecular View of Microbial Diversity and the Biosphere. Science, 276, 734.
4. Watts, S. F., 2000. The mass budgets of carbonyl sulfide, dimethyl sulfide, carbon disulfide and hydrogen sulfide - phytoplankton production in the surface ocean Atmospheric Environment, 34, 761.
5. References in Skrtic, L., 2006. Hydrogen Sulfide, Oil and Gas, and People's Health. Master's thesis, University of California, Berkeley, CA.
6. Zaman, J.; Chakma, A., 1995. Production of hydrogen and sulphur from hydrogen sulphide. Fuel Processing Technology, 41, 159.
7. Cox, B. G.; Clarke, P. F.; Pruden, B. B., 1998. Economics of thermal dissociation of H_2S to produce hydrogen. International Journal of Hydrogen Energy, 23, 531.

8. Kaloidas, V. E.; Papayannakos, N. G., 1987. Hydrogen production from the decomposition of hydrogen sulphide. Equilibrium studies on the system $H_2S/H_2/S_i$, (i=1,…,8) in the gas phase. International Journal of Hydrogen Energy, 12, 403.
9. Yao, S.; Nakayama, A.; Suzuki, E., 2001. Acetylene and hydrogen from pulsed plasma conversion of methane. Catalysis Today, 71, 219.
10. Zhao, G. -B.; Hu, X.; Plumb, O. A.; Radosz, M., 2004. Energy consumption and optimal reactor configuration for nonthermal plasma conversion of N_2O in Nitrogen and N_2O in Argon. Energy & Fuels, 18, 1522.
11. Zhao, G. -B.; Hu, X.; Yeung, M.C.; Radosz, M., 2004. Nonthermal plasma reactions of dilute nitrogen oxide mixtures: NO_x in nitrogen. Industrial & Engineering Chemistry Research, 43, 2315.
12. Zhao, G. -B.; Garikipati, S. V. B. J.; Hu, X.; Argyle, M. D.; Radosz, M., 2005. Effect of reactor configuration on nitric oxide conversion in nitrogen plasma. AIChE Journal, 51, 1813.
13. Zhao, G. -B.; Hu, X.; Argyle, M. D.; Radosz, M., 2005. Effect of CO_2 on nonthermal-plasma reactions of nitrogen oxides in N_2. Part I: ppm-level concentrations. Industrial & Engineering Chemistry Research, 44, 3925.
14. Zhao, G. -B.; John, S.; Zhang, J. -J.; Wang, L.; Mukhnahallipatna, S.; Hamann, J.; Ackerman, J.; Argyle, M.D.; Plumb, O.A., 2006. Methane conversion in pulsed corona discharge reactors. Chemical Engineering Journal, 125, 67.
15. Pick M. A., 1987. The dependence of the hydrogen concentration in metals on the surface of impurities. Journal of Nuclear Materials, 145-147, 297.

Executive Summary

Hydrogen sulfide (H_2S) is a potential resource for the production of molecular hydrogen (H_2) that is currently being lost because the established industrial Claus process converts H_2S into water and elemental sulfur. The motivation for this project was to recover H_2 from H_2S by combining plasma reactor processing with multi-layer membranes to efficiently dissociate H_2S and recover the H_2 in a pure form. The membranes were proposed to function by plasma-driven permeation, which is also called superpermeation, by forming atomic hydrogen in the plasma, which has much higher permeability through metallic membranes compared to molecular hydrogen. However, plasma-driven permeation appears to be effective only at relatively high vacuum pressures, while this project processed H_2S at pressures near industrial conditions above atmospheric pressure. The project was successful at decomposing H_2S at energy efficiencies higher than any other reports for the high H_2S concentration and moderate pressures (corresponding to high reactor throughputs) used in this study.

The project had 6 main tasks: staffing, procurement of equipment and supplies, membrane fabrication, permeation cell fabrication, membrane evaluation, and reports and briefings. The project was staffed continuously for 4 years by a graduate student and for about 2.5 years by several post-doctoral researchers. Four types of membranes were proposed in this study: thermal dense metals (such as stainless steel or platinum coated stainless steel), superpermeable metals (such as niobium or vanadium), ceramics infiltrated with superpermeable metals, and thin films of superpermeable metals. The first three types of membranes were fabricated (stainless steel and platinum coated stainless steel, bulk niobium, vanadium, and tantalum, and vanadium infiltrated porous ceramics), but superpermeation was never observed. Two experimental reactors and a permeation cell were fabricated and used extensively for methane and H_2S decomposition experiments. The methane experiments were performed to prove the reactor safety with a nontoxic reactant prior to using toxic H_2S. Also, the potential for co-processing H_2S and natural gas, as a method for sweetening natural gas, was an additional motivation for the CH_4 experiments, but they suggest that co-processing may not be feasible.

The direct methane conversion experiments produced hydrogen, acetylene, and higher hydrocarbons utilizing a co-axial cylinder corona discharge reactor, pulsed with a thyratron switch. Parameters expected to influence methane conversion including pulse frequency, charge voltage, capacitance, residence time, and electrode material were investigated. Power input appears to be the most important parameter, but the other parameters appear to have some smaller independent effects. Conversion, selectivity, and energy consumption were measured or estimated. The products were measured and analyzed by standard mass spectroscopic techniques. Methane conversions as high as 51% were achieved. The products were typically 50-60% acetylene, 20% propane, 10% ethane and ethylene, and 5% propylene. Thermodynamic energy efficiencies for the system are estimated to range from 6 to 38%, with the highest efficiencies occurring at short residence time and low power input (low specific energy), where conversion is the lowest (less than 5%). The effect of cathode material was probed using stainless steel, platinum coated stainless steel, and niobium membrane tubes. Under similar reaction conditions, methane conversions were ~50% higher with the niobium membrane and platinum coated stainless steel cathodes than with a stainless steel cathode. At the highest methane conversion of 51%, the energy efficiency for the system was 8%.

One of the reactors that was built permitted visual observation of the corona and sampling along the length of the reactor. The H_2S was diluted with four different gases (helium, argon, nitrogen, and H_2) because the breakdown voltage of pure H_2S is too high to form a plasma

in pure H_2S streams with the present reactor geometry. The minimum charge voltages required to establish a corona in each of these four gas mixtures was established. This data provided mechanistic insight on the decomposition of H_2S in plasmas that suggests that direct electron collision with H_2S and excitation of balance gas molecules, followed by subsequent reaction with H_2S, are the dominant reaction pathways. The energy efficiency for the H_2S decomposition is the highest that has been reported at reaction conditions that are above atmospheric pressures and >2% H_2S concentrations. The efficiency is better than all previous reports, including those at sub-atmospheric pressures and low H_2S concentrations, with the exception of some low pressure, low concentration microwave plasmas. The highest energy efficiency recorded translates into a cost of hydrogen production of about \$6/kg H_2 produced, assuming an electricity cost of \$0.06/kWh. While this hydrogen cost is still 2-4 times the desired level offered by the current industrial hydrogen production process (steam methane reforming), it represents a significant improvement relative to other plasma processes.

A series of experiments varying reactor operating parameters, including discharge voltage, discharge capacitance, and pulse frequency at constant reactor power input, mixtures of balance gases (argon and nitrogen), reactant flow rate and direction, and pulse waveform all show optimization potential for future reactor design and operation. At constant reactor power input (100 W), low capacitance, high pulse frequency, and low voltage operation appear to provide the highest conversion and the highest energy efficiency for H_2S decomposition, similar to the results obtained with methane as the reactant. The trigger waveform of the pulse appears to have a significant effect on H_2S conversion. Mixtures of balance gases may produce even higher H_2S conversions and energy efficiencies. Reactor throughput studies that varied the flow rate through the reactor indicate that there is a trade-off between reactor throughput and energy efficiency. Although higher energy efficiencies are obtained at higher flow rates, lower conversions are also achieved, resulting in the need for larger reactors and higher recycle rates. Thus, there is an economic optimum between lower operating costs resulting from the higher energy efficiency operation and the higher capital cost resulting from higher flow rates.

Superpermeability, or plasma driven permeation, of atomic hydrogen was not demonstrated during the project. By analogy with literature reports on the active species in NO_x decomposition plasmas, the active H atoms may exist in significant concentrations only very near (within a few millimeters) of the reactor anode. The anode is approximately 12 mm away from the membrane in the reactors used in this study, which makes it improbable that the H atoms can reach the membrane surface before combining to form molecular H_2, which has very low permeability at the near ambient temperatures in the reactor. Further, at atmospheric pressure, the mean free path of atomic hydrogen is on order of micrometers, which makes it more unlikely that it will survive without recombination to form molecular H_2 before reaching the membrane. A small membrane test cell was designed and used to obtain basic scientific data on plasma driven permeation, but even with vacuum pressures and high temperatures, no permeation was observed, suggesting that specialized surface preparation, such as ion sputtering, is also required, but is not feasible under the industrial conditions simulated in this study. A third reactor has been designed and built that will combine the anode with the hydrogen membrane and thus place the membrane in close proximity to the source of the active species. This design provides the highest likelihood of producing plasma driven permeation.

Two papers have been published in peer-reviewed journals and three presentations at a regional American Chemical Society/American Institute of Chemical Engineers (AIChE) meeting and two national AIChE meetings have been made as a result of this research.

Section 1
Methane Conversion in Pulsed Corona Discharge Reactors

1.1 Introduction

The initial experiments conducted during the project involved the decomposition of methane (CH_4) to produce hydrogen (H_2) and higher hydrocarbons. There are three primary reasons that methane was used initially instead of hydrogen sulfide (H_2S). First, the time required for approval to use H_2S was underestimated. Before the project began, a lab specifically designed for these H_2S experiments was constructed several miles away from populated areas, presumably with all necessary approvals from the University of Wyoming Environmental Health and Safety Office. However, the Environmental Health and Safety Office imposed new requirements each time we attempted to initiate H_2S experiments, which led to several months of delay before H_2S use was authorized. During this period, we decided to begin experiments with a nontoxic reactant (since methane was approved for use) to prove the design and safe operation of the pulsed corona discharge reactor. Secondly, as the primary purpose of the project was to develop novel hydrogen membranes that operate by plasma-driven permeation, methane conversion in the reactor provided an excellent source of hydrogen for the initial membrane tests. Finally, as noted in the introduction to this report and in the proposal, sour natural gas streams are a significant source of H_2S. The potential for using pulsed corona discharge reactors to sweeten sour natural gas by selectively removing H_2S is a compelling idea. These CH_4 experiments provided important data to evaluate potential operations for co-processing H_2S and natural gas.

The conversion of natural gas (typically 75% by weight methane) to hydrogen and more valuable higher hydrocarbons, including acetylene, is also of great importance to the petrochemical industry. Gaseous plasma is a good source for generating chemically active

species, including radicals, electronic excited states, and ions. Direct conversion of methane using various plasma processing technologies, including thermal arc plasma, dielectric-barrier discharge, microwave plasma, and corona discharge, has been studied for many years and has received significant recent attention. Thermal arc plasma is the only plasma technology for converting methane to acetylene that has been demonstrated on an industrial scale.[1] This process, known as the Huels process, has been practiced for more than 50 years, but the energy consumption is high due to the extremely high temperature (about 2000 K).[1] Although the selectivity for acetylene formation is high (72.9%), the gas contains a number of higher unsaturated hydrocarbons and extensive gas purification is required.[2] Nonthermal plasma technologies are characterized by low gas temperature and high electron temperature because high energy electrons are produced in the gas while the bulk temperature of the gas is unchanged. Nonthermal plasmas overcome the disadvantage of high temperature because the majority of the electrical energy goes into the production of energetic electrons rather than into gas heating. For reactions that are thermodynamically unfavorable and for which low equilibrium conversions are obtained at high reaction temperatures, nonthermal plasmas have an advantage over thermal processes because thermal equilibrium is not achieved. Therefore, nonthermal plasmas are currently being investigated as a promising alternative near-ambient temperature method to convert methane to higher hydrocarbons.[3]

Extensive recent research has shown that the hydrocarbon product distribution from a plasma reactor is determined by the type of nonthermal plasma discharge. For example, in a dielectric barrier discharge reactor, ethane is the most abundant reaction product and only small amounts of unsaturated hydrocarbons are formed.[4, 5] In microwave plasma reactors, the product distribution shifts with increasing power input, from ethane to ethylene and finally to acetylene.[6-

[9] However, the energy efficiency of microwave driven methane conversion is very low, from 0.2% to 3.3%, as reported by Huang and Suib[9] and Onoe *et al.*[6] High selectivity for acetylene is reported only in pulsed corona discharge reactors (PCDR's). Yang[5] compared the acetylene selectivity between corona discharge and dielectric barrier discharge reactors. In a corona discharge, the acetylene selectivity reaches 60%, while the acetylene selectivity is less than 6% in a dielectric barrier discharge. In a co-axial cylinder (CAC) reactor configuration, Zhu *et al.*[10] reported about 70% selectivity to acetylene. Kado *et al.*[11] obtained acetylene with approximately 94% selectivity in a point-to-point (PTP) reactor. They also reported mechanistic pathways of methane conversion in a PTP reactor using isotopic tracer experiments.[12]

The rate of methane conversion in pulsed corona reactors is consistently higher than that reported for microwave or silent discharge.[13] The combination of high methane reaction rates and high selectivity to acetylene has resulted in a number of recent research efforts on methane conversion in PCDR's. These systematic investigations of methane conversion in PCDR's[13-18] have included reports of over 85% acetylene selectivity in a pulsed corona discharge at high pulse frequency in a CAC reactor[15] and in a PTP reactor.[17] The effects of pulse voltage rise time, reaction temperature, pulse voltage, pulse frequency, gas flow rate, electrode arrangement, and reactor configuration (CAC reactor and PTP reactor) on methane conversion and product selectivities were analyzed. Pulse frequency has been reported as the most important factor influencing acetylene selectivity and methane reaction rate.[15] A pulse power supply with a frequency up to 10 kHz with a PTP type reactor provided the optimum combination for acetylene and hydrogen production.[14]

Although extensive investigations have been reported for methane conversion in PCDR's, further study is necessary to clarify several issues. First, the effect of the pulse-forming

capacitance (the capacitance of the charging capacitor) on methane reaction rate and product selectivities is of interest. For NO_x conversion in pulsed corona discharges, many investigations[19-22] have concluded that the pulse-forming capacitance affects energy transfer efficiency from the external circuit to the reactor. However, there are no studies that explore the effect of the pulse-forming capacitance on methane conversion. Second, the effect of the cathode material on methane reaction rate and product selectivities has not received attention. The role of electrode material in plasma-induced reactions is disputed, specifically whether metal electrodes serve simply as conductors of electricity or exhibit a catalytic effect.[23] Tanaka *et al.*[24] and Luo *et al.*[23] found that the metal surfaces of the anode have clear catalytic effects for ammonia synthesis and NO decomposition, respectively. However, there are no results that illustrate the effect of cathode material on methane conversion. Third, the effect of gas flow rate or residence time on methane reaction rate is important. Yao *et al.*[15] found that gas flow rate did not significantly affect methane conversion rate in a very small CAC reactor (0.01m diameter × 0.15 m long). Although Yao *et al.*[17] reported that a PTP reactor with high pulse frequency (up to 10 kHz) can provide high methane reaction rate, scale-up of such PTP reactors is not straightforward. All pulsed corona discharge reactors used for methane conversion have been small, with low flow rates ($<2 \times 10^{-4}$ mol·s^{-1}) that are far from practical for commercial operation.[13-18] The design and characterization of larger reactors that can accommodate high throughput are critical if these reactors are to be applied successfully in commercial operations.

The goals of this work are to investigate the effect of pulse-forming capacitance, cathode materials, gas flow rates, and specific energy input on methane conversion and product distribution in large-scale co-axial cylinder PCDR's.

1.2 Experimental

Figure 1.1 shows a diagram of the experimental system. The system consists of a reactor with an electrical system built around a thyratron switch, a flow control and distribution system, and a gas sampling system. The reactor is oriented vertically, with the gas flow from bottom to top. Experiments were conducted using three different metal tubes as the cathode: stainless steel, stainless steel coated with a 100 nm thick layer of platinum, and niobium. The cathode is 0.024 m in diameter and 0.914 m in length for the stainless steel and platinum coated stainless steel tubes and 0.60 m in length for the niobium tube, while the anode is a stainless steel wire 1 mm in diameter passing axially through the center of the tube.

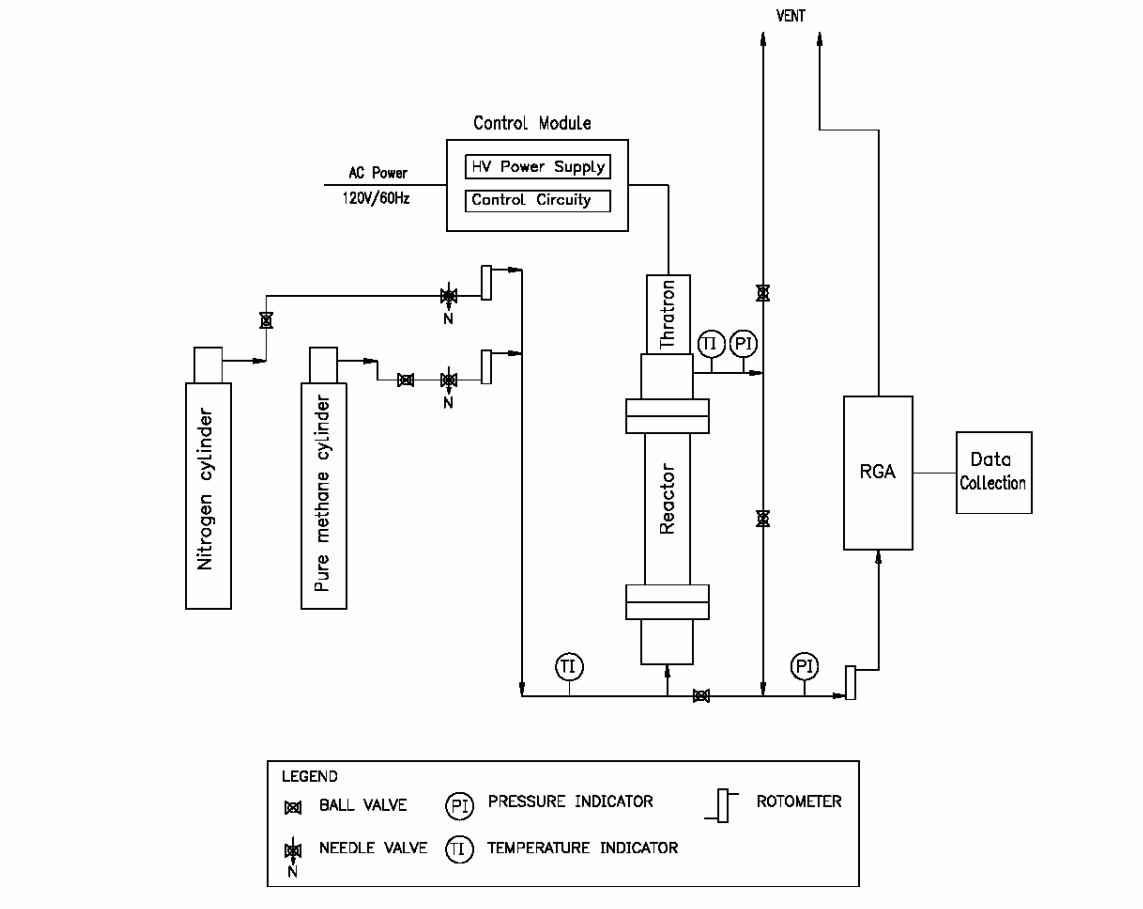

Figure 1.1 Experimental setup

The wire is positively charged, while the tube is grounded. The gas flowing through the reactor tube is converted to plasma by high voltage discharge from the reactor anode.

Figure 1.2 contains an electrical circuit diagram of the discharge reactor. The electrical circuit of the plasma reactor and the processes of charging and discharging used in this work are quite similar to previous plasma reactor designs used for NO_x conversion in nonthermal plasma.[25] The only difference is that a thyratron switch is used to initiate the corona discharge in this work, while a hydrogen switch was used in the previous work. The electrical system can deliver charge voltages from 10 kV to 25 kV at pulse frequencies from 0 to 1000 Hz. The capacitor bank provides space for four "doorknob" capacitors, in increments of 640 pF. The capacitance of the rest of the electrical system is negligible. The thyratron switch element is cooled with compressed air. The capacitors are charged to the desired voltage using a 40 kV oil-cooled high voltage power supply. A thyratron switch is connected directly to the anode of the reactor. On triggering the thyratron, the stored energy in the capacitors is discharged in a few nanoseconds to the anode, giving rise to a high rate of change of voltage (dV/dt) on the anode.

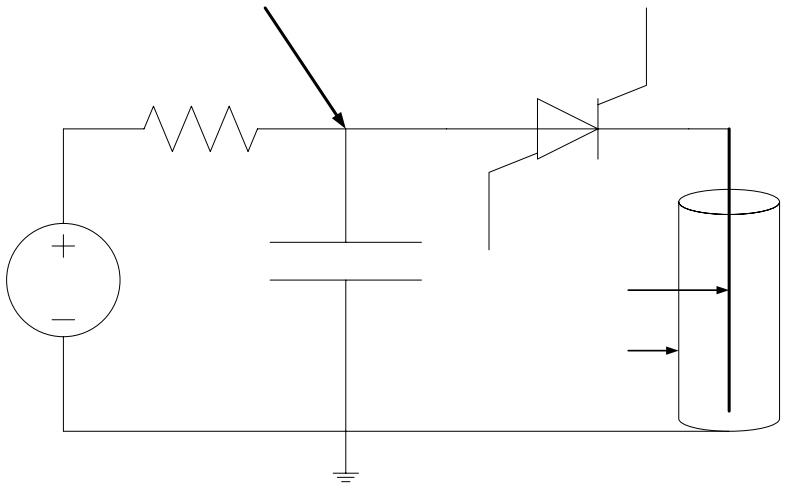

Figure 1.2. Reactor electrical circuit diagram.

This process of charging and discharging the capacitors is repeated based on the thyratron trigger frequency leading to sustained current streamers or plasma. Once triggered, the thyratron will shut off only if the cathode potential becomes higher than the anode potential or the current reaches zero. The anode potential is always higher than the cathode potential and the cathode potential is near zero once the corona is produced. After the corona begins, the current reaches zero only after the capacitor discharges completely. In this way, the energy released by the capacitors per pulse can be calculated from $\frac{1}{2}CV_c^2$, where C is the pulse forming capacitance as shown in Table 1.1 and V_c is the constant charge voltage before discharge (20 kV for these experiments). The power consumed, W ($J \cdot s^{-1}$), was calculated as the product of the input energy per pulse and the pulse frequency, $\frac{1}{2}fCV_c^2$, where f is pulse frequency in Hz.

In a hydrogen switch based reactor, both reactor pressure and losses in the reactor due to resistance and inductance can cause the switch to open before the capacitor has discharged completely, which would introduce an error in the power calculations based on $\frac{1}{2}CV_c^2$. However, our previous work showed that 97-98% of energy stored in the capacitors are discharged in to the hydrogen switch based reactor.[26] By using a thyratron switch, the energy stored in the capacitance can be completely discharged into the plasma. One issue introduced by using a thyratron switch is the thyratron cathode is not grounded, which requires the triggering and heating circuit of the thyratron to be electrically isolated using an isolation transformer. This makes the reactor bulky and more expensive. Also, due to the ungrounded cathode, the radio frequency (RF) emission from the thyratron switch is significant and causes malfunctions of the high voltage and current measuring equipment (an oscilloscope). Measurements of instantaneous voltage and current are not reliable due to this RF emission.

The experimental test matrix is shown in Table 1.1. The high purity methane (Air Gas Company, 99.97%) reactant gas flow rates shown in Table 1.1 are reported at the PCDR entrance conditions of ambient temperature (~300K) and 161.4 kPa**.** Stable products were measured with an online Residual Gas Analyzer (RGA, Stanford Research Systems, Inc. QMS100), which is a mass spectrometer with quadrupole probe.

Table 1.1. Experimental matrix

Cathode material	Tube length (m)	Flowrate ($\times 10^{-5}$ $m^3 \cdot s^{-1}$)	Capacitance (pF)	Charge voltage (kV)
SS	0.914	2.47, 3.71, 4.94, 7.41, 9.88	1920	20
Pt/SS	0.914	2.47	1280, 1920	20
Nb	0.609	2.47	1920	20

Gas products are sampled through a capillary tube of 2.6 m length from reactor outlet to the RGA. To perform quantitative measurements, the instrument was calibrated for H_2, CH_4, C_2H_2, C_2H_4, C_2H_6, C_3H_6 and C_3H_8 using gases of certified composition (ultra high purity gases from US Welding and certified binary gas mixtures of He and the respective hydrocarbons from US Airgas). The hydrocarbon samples in the source chamber are ionized to create fragments of different masses. Each specific hydrocarbon has its own characteristic peak. The intensity of each selected ion in the mass spectrum can be described mathematically as follows:[27]

$$I(M) = \sum_j S(M, j) \cdot P(j) \tag{1}$$

where $I(M)$ is the measured current intensity at mass M, $S(M, j)$ is the sensitivity factor of component j at mass M, and $P(j)$ is the partial pressure for component j. The number of selected current intensities must be greater than the number of components to obtain quantitative results.

The complex sample spectra are deconvoluted using the linear least squares method, which can be expressed as:

$$\vec{P} = (S^t \cdot S)^{-1} \cdot S^t \cdot \vec{I} \tag{2}$$

where $\vec{P}$ is the vector of estimated partial pressure for every component, $\vec{I}$ is the vector containing the measured current intensities, $\boldsymbol{S}$ is the two dimensional matrix containing the sensitivity factor of each component at specified mass M, and $\boldsymbol{S}^t$ is the transpose of **S**. The sensitivity factor for each component was obtained using both the pure gas and mixtures of certified composition. The fragmentation factor of a specific species at each mass M (i.e., ratio of ionic signal at mass M to the ion signal at the principle mass peak) is determined from the pure gas. The sensitivity factor of N_2 is obtained from the RGA manufacturer. The sensitivity factors of H_2 and He are determined from binary gas mixtures of H_2 + N_2 (49.34% H_2 in N_2, US Airgas) and He + N_2 (0.972% He in N_2, 50.32% He in N_2, and 98.96% He in N_2, US Airgas) because there is no overlap of ionic peaks of N_2 and H_2 or N_2 and He. Then, binary gas mixtures of He and hydrocarbons with different certified concentration are used to determine sensitivity factors for each hydrocarbon because there is no overlap of ionic peaks of He and the hydrocarbons.

Gas products were sampled when steady-state was reached, which required 20 minutes at low gas flow rate (2.47×10^{-5} $m^3 \cdot s^{-1}$) and 5 minutes at high gas flow rate (9.88×10^{-5} $m^3 \cdot s^{-1}$). For each parameter set, at least two experiments were performed to assure that the results are repeatable. The complex sample spectra of gas products were deconvoluted using the linear least squares method described above to obtain mole fractions of each species. All experimental data were reproducible within a ±10% error limit, including the RGA and flow measurement uncertainties.

The atomic hydrogen balance at the reactor inlet and outlet was used to estimate the molar flow rate of gas products at the reactor outlet:

$$N_o = \frac{4 \cdot N_{i,CH_4}}{4 \cdot x_{CH_4} + 2 \cdot x_{H_2} + 2 \cdot x_{C_2H_2} + 4 \cdot x_{C_2H_4} + 6 \cdot x_{C_2H_6}} \quad (1)$$

where N_{i,CH_4} is the molar flow rate of methane at the reactor inlet ($mol \cdot s^{-1}$), N_o is the molar flow rate of the gas phase at the reactor outlet ($mol \cdot s^{-1}$), and x_i is the measured mole fraction of species i at the reactor outlet. The molar flow rate of all major species at the reactor outlet can be obtained from Equation 1. Although hydrocarbon products containing up to three carbons were measured using the RGA, only methane and C_2 species were included in Equation 1 because the experimental results showed that the major products were H_2, C_2H_2, C_2H_4 and C_2H_6, with only traces of higher hydrocarbons, consistent with previously reported results.[7, 10, 15-18] Material balance calculations show that Equation 1 is accurate for all power inputs below ~225 W. However, Equation 1 is less accurate for experimental combinations of high power input and low gas flow rate because C_4+ hydrocarbons that formed were not detected by the RGA and hydrogen-containing carbonaceous solids were observed in the reactor following these experiments. The amount of carbon deposition was estimated from the carbon balance as follows:

$$N_{o,C} = N_{i,CH_4} - N_o \cdot [x_{CH_4} + 2 \cdot (x_{C_2H_2} + x_{C_2H_4} + x_{C_2H_6})] \quad (2)$$

where $N_{o,C}$ is the molar rate of carbon deposition in the reactor ($mol \cdot s^{-1}$). The solid carbonaceous deposits were analyzed by magic angle spinning (MAS) nuclear magnetic resonance (NMR) spectroscopy (Bruker Avance DRX-700).

Several parameters used to describe the experimental results are defined as follows:

(1) Specific energy input, E_s ($kJ \cdot mol^{-1}$):

$$E_s = \frac{W}{1000 \cdot u \cdot 64.7} \tag{3}$$

where u is gas flowrate ($m^3 \cdot s^{-1}$) of UHP methane and 64.7 is the constant number of moles per unit reactor volume (mol m^{-3}) at 161.4 kPa and 300 K.

(2) Methane conversion (%):

$$X = \left[1 - \frac{N_{o,CH_4}}{N_{i,CH_4}}\right] \cdot 100 \tag{4}$$

where $N_{o,CH4}$ is the molar flow rate of methane at the reactor outlet.

(3) Selectivity for hydrocarbons, hydrogen, and carbon, (%):

$$S_{CnHm} = \frac{n \cdot N_{o,CnHm}}{CH_{4\,\mathrm{conv}}} \cdot 100 \tag{5}$$

$$S_{H_2} = \frac{0.5 \cdot N_{o,H_2}}{CH_{4\,\mathrm{conv}}} \cdot 100 \tag{6}$$

$$S_C = \frac{N_{o,C}}{CH_{4\,\mathrm{conv}}} \cdot 100 \tag{7}$$

where $N_{o,CnHm}$ and $N_{o,H2}$ are molar flow rates of hydrocarbon and hydrogen at the reactor outlet, respectively, $N_{o,C}$ is the molar rate of carbon deposition within the reactor, and CH_{4conv} is the reaction rate of methane ($mol \cdot s^{-1}$). These definitions of selectivity are consistent with those used by other investigators.[8, 10] Carbon selectivity includes all products with more than four carbons. As reported in the Results and Discussion section, the carbon selectivity was negligible for most experiments and only became measurable at power inputs greater than 225 W.

As discussed above, the major products of methane conversion are C_2H_2, C_2H_4, C_2H_6, C, and H_2. The resulting reactions are all endothermic:

$$CH_4 \rightarrow C + 2H_2 \qquad \Delta H_1^o = 74.9\, kJ / mol\, CH_4 \tag{R1}$$

$$CH_4 \rightarrow \frac{1}{2}C_2H_2 + \frac{3}{2}H_2 \qquad \Delta H_2^o = 188.2\,kJ/mol\,CH_4 \qquad \text{(R2)}$$

$$CH_4 \rightarrow \frac{1}{2}C_2H_4 + H_2 \qquad \Delta H_3^o = 100.9\,kJ/mol\,CH_4 \qquad \text{(R3)}$$

$$CH_4 \rightarrow \frac{1}{2}C_2H_6 + \frac{1}{2}H_2 \qquad \Delta H_4^o = 32.5\,kJ/mol\,CH_4 \qquad \text{(R4)}$$

Energy efficiency is defined as the ratio of the minimum energy required to convert methane to C, C_2H_2, C_2H_4 and C_2H_6 to the actual energy input in the reactor.

(4) Energy efficiency (%):

$$E = \frac{1000 \cdot (N_{o,C} \cdot \Delta H_1^0 + 2 \cdot N_{o,C_2H_2} \cdot \Delta H_2^0 + 2 \cdot N_{o,C_2H_4} \cdot \Delta H_3^0 + 2 \cdot N_{o,C_2H_6} \cdot \Delta H_4^0)}{W} \times 100 \qquad (8)$$

1.3 Results and Discussion

1.3.1 Product distribution. Figures 1.3(a), (b) and (c) show the reactor product distribution as a function of power input at a flowrate of 2.47×10^{-5} $m^3 \cdot s^{-1}$ and pulse-forming capacitance of 1920 pF for the stainless steel tube (SS), platinum coated stainless steel tube (Pt/SS), and the niobium (Nb) tube, respectively. As mentioned previously, the major products were H_2, C_2H_2, C_2H_4 and C_2H_6, with only traces of higher hydrocarbons, except at power inputs >~225 W. The methane concentration decreases with increasing power input, indicating that methane conversion increases with increasing power input. Meanwhile, concentrations of H_2 and C_2H_2 increase with increasing power input. The C_2H_6 concentration initially increases with increasing power input, but reaches a maximum at about 300 W power input and then decreases. At low power input (less than 200 W), C_2H_4 is not detectable. The C_2H_4 concentration begins to increase from zero near the point where the C_2H_6 concentration reaches a maximum. With further increases in power input, the C_2H_4 concentration reaches a maximum and then decreases [Figures 1.3(a) and (b)]. The trends of the C_2H_4 and C_2H_6 concentrations with power input suggest that C_2H_4 formation is primarily a result of dehydrogenation of C_2H_6. The

concentrations of C_2H_4 and C_2H_6 are always less than 2 mol%, while the concentration of C_2H_2 reaches nearly 10 mol%. The concentration of C_2H_2 is always greater than 2 mol% even when C_2H_4 is not detectable (at power inputs less than 200 W), which suggests that C_2H_2 formation occurs via dimerization of CH radicals in the streamer channels instead of by dehydrogenation of C_2H_4.

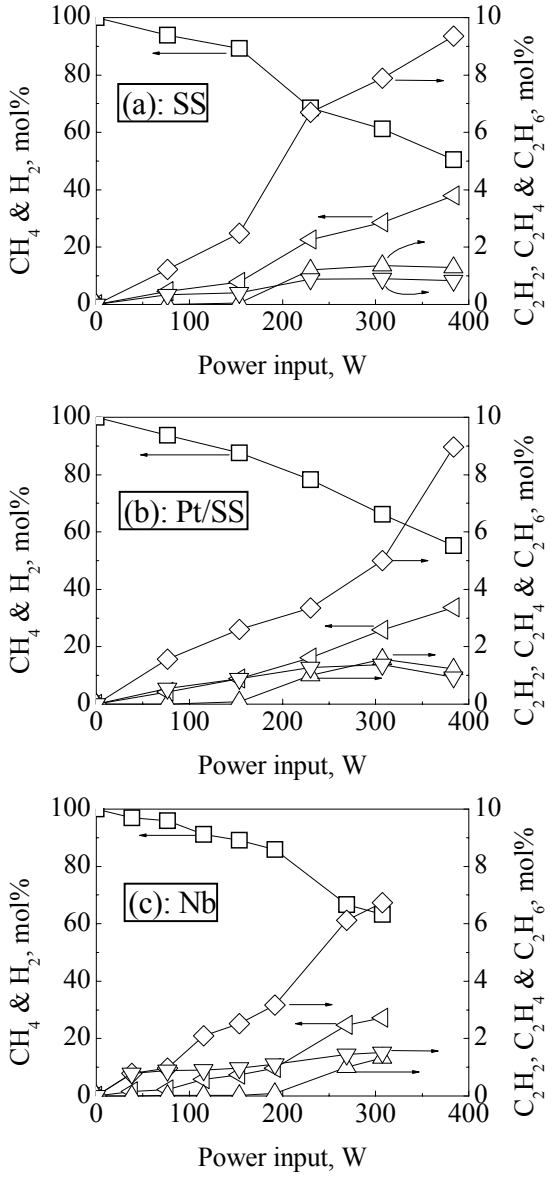

Figure 1.3. Reactor outlet gas concentrations as a function of power input at a flowrate of 2.47×10^{-5} $m^3 \cdot s^{-1}$ and pulse-forming capacitance of 1920 pF. (a) SS tube, (b) Pt/SS tube, (c) Nb tube (□: CH_4, ◇: C_2H_2, △: C_2H_4, ▽: C_2H_6, ◁: H_2)

In corona discharges, a high-voltage, short-duration (<100 ns)[22, 28] electrical discharge between non-uniform electrodes is used to produce streamers through the growth of electron avalanches formed by electron collision ionization events in the gas. A streamer is a region of highly ionized gas where a wide range of active radicals and chemical species are formed through electron collision reactions with the background gas. These active species, in turn, initiate bulk phase reactions that lead to methane conversion. Therefore, all active species are first formed in the streamer.

Many investigators[4, 7, 12, 15, 29, 30] have explored the mechanism of CH, CH_2 and CH_3 radical formation. The generally accepted mechanism is via direct electron collision reactions with methane (E1a-c),

$$e + CH_4 \rightarrow CH_3 + H + e \quad \text{(E1a)}$$

$$e + CH_4 \rightarrow CH_2 + H + H + e \quad \text{(E1b)}$$

$$e + CH_4 \rightarrow CH + H + H + H + e \quad \text{(E1c)}$$

which initiate the subsequent dimerization reactions responsible for formation of higher hydrocarbons. However, the relative importance of electron collision reactions E1a-c and the yields of CH, CH_2 and CH_3 radicals depend on energy input per pulse and specific reactor configuration. Kado *et al.*[12] explored experimentally the mechanism of CH_4 decomposition in a point-to-point reactor using isotopically labeled reactants and products. They showed that the dominant reaction pathways include direct dissociation of methane into CH and atomic C radicals, which then dimerize to form C_2H_2 and C_2 radicals. The C_2 radicals are subsequently hydrogenated to form acetylene, which produces C_2D_2 and C_2HD in the presence of D_2 added to the reaction mixture. Yao *et al.*[15] performed an experimental investigation on methane conversion in plasma reactors with CAC reactor configuration, with cylinder diameter of 10 mm,

cylinder length of 150 mm, and anode wire diameters of 0.5 mm and 2.9 mm. At an energy input of 7.5 mJ/pulse, they proposed that the major products of electron collision with methane are CH and CH_2 radicals based on the observed product selectivities. Kirikov *et al.*[29] investigated theoretically the free radical formation mechanism formation mechanism in a pulsed surface discharge plasma reactor with two parallel electrodes situated on a dielectric plate and found that the primary products are CH and CH_3 radicals when the energy input per pulse is larger than 20 mJ. When the energy input is larger than 30 mJ/pulse, the concentration of the CH radicals exceeds the concentration of CH_3 radicals, which is about three orders of magnitude higher than the CH_2 radical concentration.

Although the reactor geometry used in this work is very different from that analyzed by Kirikov *et al.*[29], our results appear to be consistent with their theoretical results.[29] For an energy input of 384 mJ/pulse with our larger reactor and reactant flow rates, the results of Figure 1.3 suggest that the majority of the radicals formed in the discharge channel are CH radicals, with a smaller number of CH_3 radicals, and very small numbers of CH_2 radicals because the concentration of C_2H_2 is far larger than that of C_2H_6 and C_2H_4, and the concentration of C_2H_4 is close to zero at power inputs less than 200 W. The results are consistent with CH radicals as the main active species leading to the synthesis of C_2H_2 through the following rapid reactions:[7, 31]

$$CH + CH \rightarrow C_2H_2 \qquad k = 1.20 \times 10^{14}\ cm^3 \cdot mol^{-1} \cdot s^{-1} \qquad \text{(R5)}$$

$$CH + CH_3 \rightarrow C_2H_3 + H \qquad k = 3.01 \times 10^{13}\ cm^3 \cdot mol^{-1} \cdot s^{-1} \qquad \text{(R6)}$$

$$C_2H_3 + H \rightarrow C_2H_2 + H_2 \qquad k = 1.20 \times 10^{13}\ cm^3 \cdot mol^{-1} \cdot s^{-1} \qquad \text{(R7)}$$

This would explain the increase in C_2H_2 concentration with increasing power input. CH_3 radicals appear to be the main active species leading to the formation of C_2H_6 through the following reaction:[7, 31]

$$CH_3 + CH_3 \rightarrow C_2H_6 \qquad k = 3.61 \times 10^{13}\ cm^3 \cdot mol^{-1} \cdot s^{-1} \qquad (R8)$$

Dehydrogenation of C_2H_6 to C_2H_4 is highly temperature dependent:[7, 31]

$$H + C_2H_6 \rightarrow C_2H_5 + H_2 \qquad k = 1.44 \times 10^9 T^{1.5} \exp(-3730/T)\ cm^3 \cdot mol^{-1} \cdot s^{-1} \qquad (R9)$$

where T is in K and

$$H + C_2H_5 \rightarrow C_2H_4 + H_2 \qquad k = 3.01 \times 10^{13}\ cm^3 \cdot mol^{-1} \cdot s^{-1} \qquad (R10)$$

At ambient temperatures, the reaction rate for R9 is negligible and only contributes to C_2H_4 formation at higher temperatures. In this work, the temperature is close to ambient at low power inputs, leading to negligible C_2H_4 formation via dehydrogenation of C_2H_6. However, the reactor temperature increases with increasing power input, especially near the outlet, leading to dehydrogenation of C_2H_6.

To verify the importance of thermal reactions to C_2H_4 formation from C_2H_6, the temperature profile within the reactor must be known. However, the temperature cannot be measured accurately because the thyratron RF emission heavily disturbs thermocouple signals. Mechanical, bimetallic thermometers placed in the reactor outlet stream proved to be relatively unresponsive and displayed near ambient temperatures, despite the fact that the reactor external support casing (a 0.05 m diameter stainless steel tube concentric to the reactor cathode) was hot to the touch (>350 K) near the reactor outlet. Therefore, the hydrogen switch based reactor (used for NO_x conversion in our previous work[22, 25, 28, 32-37]) with the same reactor geometry as the thyratron-based reactor (tube length: 0.914 m; tube diameter: 0.024m, wire diameter: 1 mm) was used during methane conversion to estimate the temperatures in the thyratron-based reactor. Figure 1.4 shows the measured reactor tube wall temperature function of specific energy input. The data were obtained 0.16 m from the reactor outlet after 10 minutes of operation at a reactor inlet flow rate of $9.76 \times 10^{-5}\ m^3 \cdot s^{-1}$ and pressure of 175 kPa of pure methane. The tube wall

temperature linearly increases with increasing specific energy input. Based on extrapolation of Figure 1.4 and heat transfer calculations, the estimated temperature at the center of the reactor at a power input of 200 W (corresponding to a specific energy input of 125 kJ·mol^{-1}) is ~853 K, which is sufficient to initiate a significant rate of C_2H_6 dehydrogenation based on the rate constant for R9 and the measured outlet C_2H_6 concentration. The experimental results for C_2H_4 and C_2H_6 concentrations shown in Figure 1.3 are consistent with these arguments.

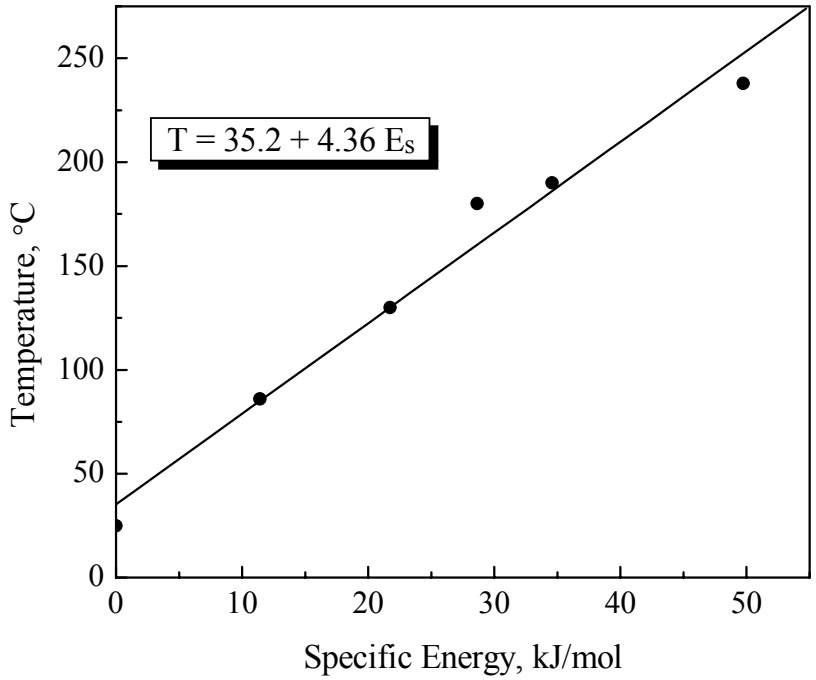

Figure 1.4. Temperature of external reactor tube wall of 0.16 m from the outlet as a function of specific energy (measured in a geometrically-similar hydrogen switch-based plasma reactor).

Figure 1.5 shows the H/C ratio of the outlet gas as a function of power input at the same conditions as Figure 1.3. If the H/C ratio of the outlet gas is equal to 4, the material balance indicates that the formation of C_3+ hydrocarbons and the deposition of carbonaceous material within the reactor are negligible. The results of Figure 1.5 show that C_3+ hydrocarbons or carbonaceous deposits are formed only at power inputs higher than ~225 W, which is consistent

with our experimental observation. Carbonaceous solid deposition was observed only at pulse frequencies higher than 800 Hz, corresponding to 307 W power input at 1920 pF capacitance. Lighter liquid hydrocarbons, such as benzene, were probably formed in the power interval between 225 and 307 W (in which no solid deposits were observed in the reactor and yet the H/C ratio was calculated as >4), but these species were not detectable with the RGA. Therefore, although no solid deposits were observed in the reactor, the mass balance calculation accounted for these species as missing carbon. This assumption is consistent with analysis of the carbonaceous residues by NMR that showed they consisted of polynuclear aromatic compounds, which were probably formed from lighter molecular weight aromatic intermediates.

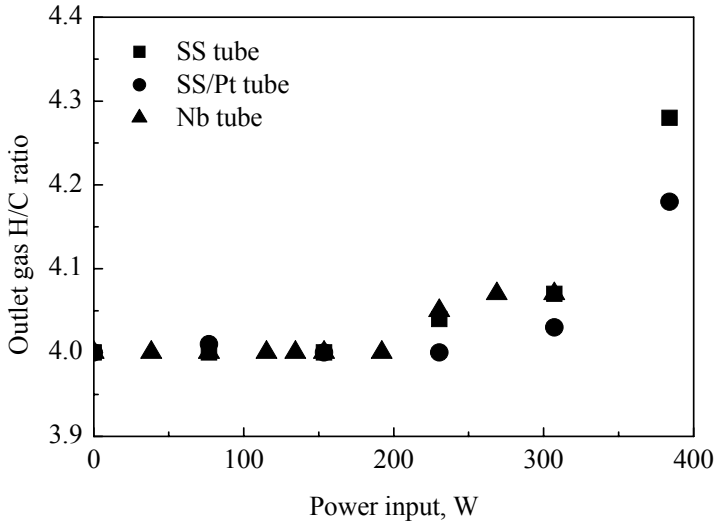

Figure 1.5. The H/C ratio of outlet gas as a function of power input at a flowrate of 2.47 × 10^{-5} $m^3 \cdot s^{-1}$ and pulse-forming capacitance of 1920 pF.

1.3.2 The effect of capacitance. Figure 1.6 shows the effect of capacitance on methane conversion, energy efficiency and product selectivity for the Pt/SS tube at a flowrate of 2.47 × 10^{-5} $m^3 \cdot s^{-1}$. Two capacitances are compared in this figure: filled symbols correspond to 1920 pF, while open symbols correspond to 1280 pF. At a given power input >150 W, methane

conversion and energy efficiency are higher for the 1280 pF results compared to those obtained at 1920 pF, as shown in Figure 1.6(a).

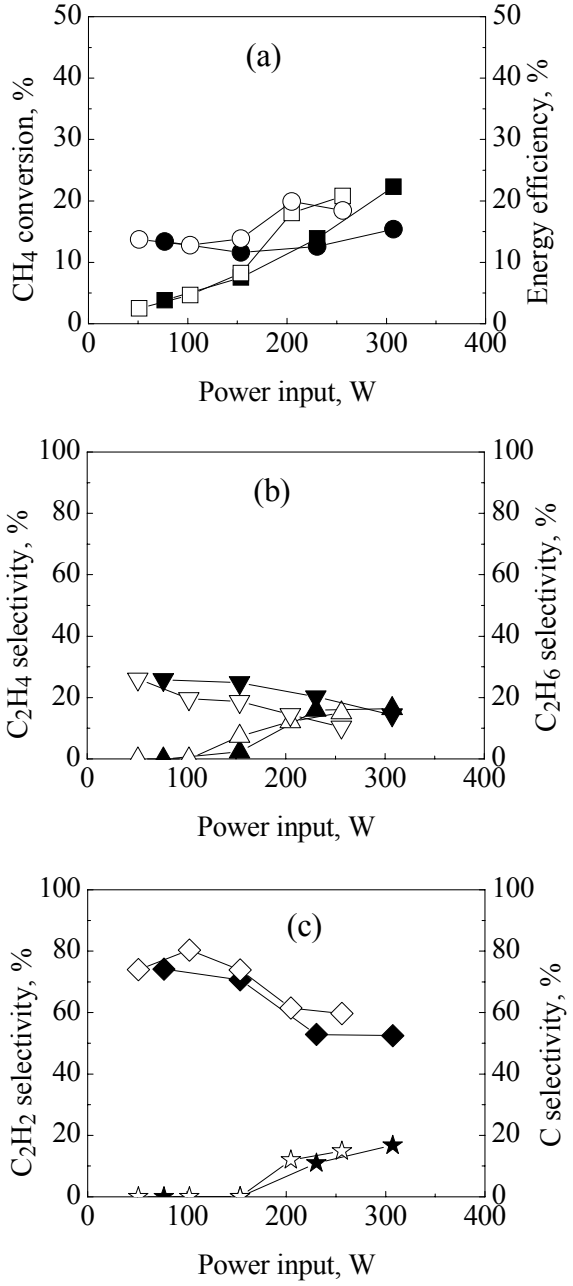

Figure 1.6. The effect of capacitance on methane conversion and product selectivity for Pt/SS tube at a flowrate of 2.47 × 10^{-5} $m^3 \cdot s^{-1}$.(1920 PF, ■: CH_4 conversion, ●: Energy efficiency, ◆: C_2H_2 selectivity, ▲: C_2H_4 selectivity, ▼: C_2H_6 selectivity, ★: Carbon selectivity. 1280 PF, □: CH_4 conversion, ○: Energy efficiency, ◇: C_2H_2 selectivity, △: C_2H_4 selectivity, ▽: C_2H_6 selectivity, ☆: Carbon selectivity)

The selectivity for C_2H_6 at 1280 pF is lower than that at 1920 pF, while C_2H_4 selectivities are approximately the same for both levels of capacitance (Figure 1.6(b)). The C_2H_2 selectivity at 1280 pF is slightly higher than that for 1920 pF, while carbon selectivity does not appear to change with capacitance (Figure 1.6(c)).

Identical power inputs can be achieved using high capacitance and low pulse frequency or low capacitance with high pulse frequency, as discussed previously. The results of Figure 1.6 indicate that operation of the PCDR at low capacitance with high pulse frequency is better than operation at high capacitance with low pulse frequency because methane conversion, energy efficiency, and acetylene selectivity (which is a more valuable product than ethane) are slightly higher at low capacitance with high pulse frequency. These results are consistent with the results of Yao *et al.*,[15] who found that high pulse frequency promotes acetylene formation and improves methane conversion.

In addition, Uhm and Lee[19] reported that reactor capacitance plays a pivotal role in the energy efficiency of nonthermal plasma reactors. Mok *et al.*[20] found that when the pulse-forming capacitance is five times larger than the geometric capacitance of the reactor, the energy efficiency was maximized. Chung *et al*.[21] found the maximum energy efficiency for NO conversion in a PCDR when the pulse-forming capacitance is 3.4 times larger than the reactor capacitance. The NO reactor results should be relevant because both CH_4 and NO reactions originate with similar electron collision reactions.[7, 31] These findings indicate that the energy efficiency of a PCDR can be improved by keeping the ratio of pulse-forming capacitance to reactor capacitance low, typically 3-5. The capacitance of a co-axial cylinder is defined as:[38]

$$C_R = \frac{2\pi\varepsilon L}{\ln(R/r)} \tag{9}$$

where ε is the permittivity of CH_4, L is the length of the reactor, R is the inner radius of the cathode (reactor tube) and r is the outer radius of the anode (central wire). As our reactor has a capacitance of 18.3 pF, the ratio of the pulse-forming capacitance (C_P) to reactor capacitance (C_R) for our reactor configuration is:

$$\frac{C_P}{C_R} = \frac{C_P}{18.3} \tag{10}$$

Therefore, by decreasing pulse-forming capacitance from 1920 pF to 1280 pF, the ratio of the pulse-forming capacitance to the reactor capacitance decreases from 105 to 70. Although both values are far larger than the optimal ratio suggested by Mok *et al.*[20] and Chung *et al.*,[21] our results indicate a trend toward improved conversion and energy efficiency as the ratio is decreased toward the optimum.

1.3.3 The effect of cathode material. Figure 1.7 illustrates the effect of cathode material on methane conversion, energy efficiency, and selectivity of C_2H_4, C_2H_6, C_2H_2 and carbon for the SS and Pt/SS tubes at the same experimental conditions. For power inputs less than ~225 W, methane conversion for both SS and Pt/SS cathodes is nearly the same. However, at higher power inputs, methane conversion and energy efficiency for the Pt/SS cathode are slightly higher than for the SS cathode [Figure 1.7(a)], suggesting that the Pt coating may have a small catalytic effect on methane conversion. Platinum is a known catalyst for methane conversion.[39, 40] However, Pt catalytic reactions typically require high reaction temperature (723 to 773 K).[41] The temperature of the cathode and the outlet gas in our experiments increased with increasing power input (and could easily exceed 750 K), which would enhance any catalytic effect of the Pt coated cathode and would be consistent with the experimental results in Figure 1.7(a).

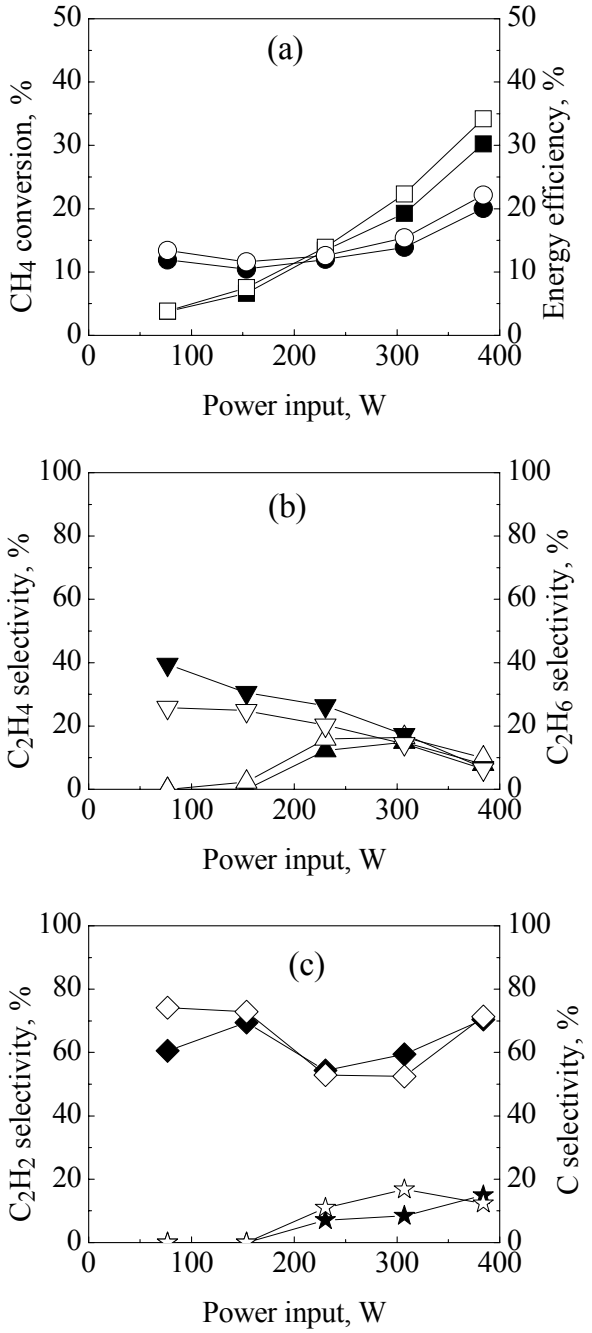

Figure 1.7. The effect of cathode material on methane conversion and product selectivity for SS tube and Pt/SS tube at a flowrate of 2.47×10^{-5} $m^3 \cdot s^{-1}$ and pulse-forming capacitance of 1920 pF. (SS tube, ■: CH_4 conversion, ●: Energy efficiency, ◆: C_2H_2 selectivity, ▲: C_2H_4 selectivity, ▼: C_2H_6 selectivity, ★: Carbon selectivityPt/SS tube, □: CH_4 conversion, ○: Energy efficiency, ◇: C_2H_2 selectivity, △: C_2H_4 selectivity, ▽: C_2H_6 selectivity, ☆: Carbon selectivity)

A Pt coated anode may be more effective as a catalyst than the cathode, as suggested by the results of Eichwald *et al.*,[42] who used a mathematical model to simulate the dynamics of streamer discharges in flue gas. They found the temperature close to the wire (anode) is much higher (>800 K) than the temperatures near the tube wall (cathode) because of the strong electric field in the vicinity of the wire. Therefore, a platinum coated anode should provide a larger catalytic effect than a Pt coated cathode, as evidenced by the strong catalytic effect reported by Luo *et al.*[23] for a Pt coated stainless steel rod anode used for NO conversion.

Figure 1.7(b) shows that C_2H_6 selectivity is slightly lower and C_2H_4 selectivity is slightly higher for the platinum coated cathode compared to the plain stainless steel tube. Low C_2H_6 selectivity and high C_2H_4 selectivity for the Pt coated cathode is consistent with the known ability of platinum to dehydrogenate alkanes,[41] in this case of C_2H_6 to C_2H_4.

Comparison of C_2H_2 and carbon selectivities shows no distinct trends between the stainless steel and platinum coated stainless steel cathodes.

1.3.4 The effect of gas flowrate. Figures 1.8(a) and (b) show the effect of gas flow rate on methane conversion, energy efficiency and product selectivity for the stainless steel tube at power inputs of 154 W and 307 W, respectively. Figure 1.8(a) illustrates that at low power input, methane conversion decreases and energy efficiency increases with increasing gas flow rate. Selectivity to acetylene and hydrogen decreases with increasing gas flow rate, while selectivity to ethane increases with increasing gas flow rate. No carbon and ethylene were detected at this lower power input, consistent with the results in Figures 1.3 and 1.5. With increasing gas flow rate, specific energy input decreases at the same overall power input. Therefore, methane conversion decreases with increasing gas flow rate. At high gas flow rate and lower methane conversion, decreasing rates of radical recombination reactions, such as

methane formation by recombination reaction of H and CH_3 radicals, results in higher energy efficiency at higher gas flow rates. However, high gas flow rates also decrease the concentration of H radicals in the streamers, indicating that the dehydrogenation rate of CH_3 to CH is reduced, which leads to decreasing selectivity for acetylene and increasing C_2H_6 selectivity with increasing gas flow rate. Selectivity for hydrogen decreases with increasing gas flow rate (following the trend for C_2H_2) because methane conversion to acetylene (R2) produces three times as much hydrogen as methane conversion to ethane (reaction R4).

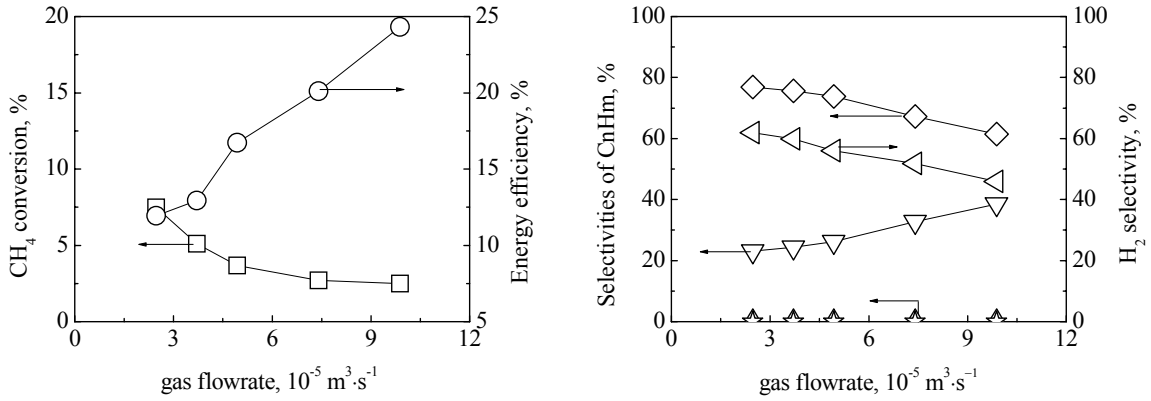

(a) 400 Hz, 154 W power input

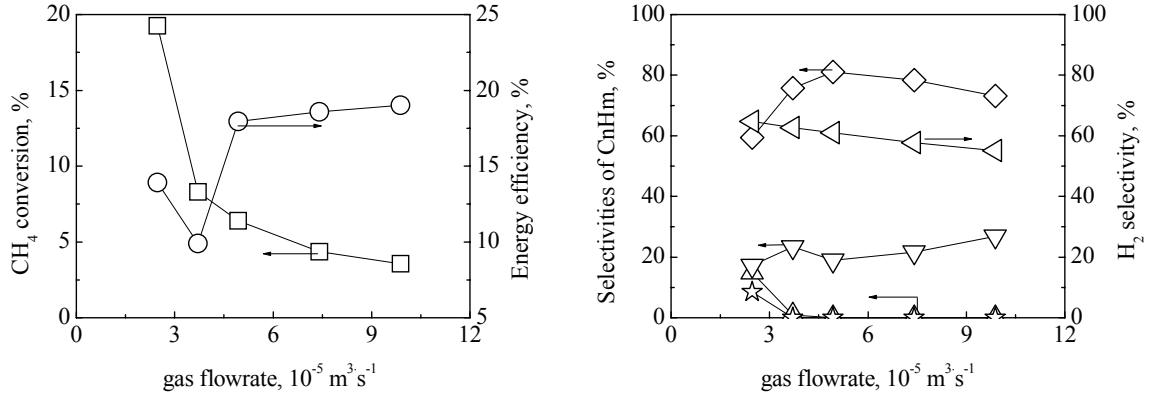

(b) 800 Hz, 307 W power input

Figure 1.8. The effect of gas flowrates on methane conversion and product selectivity for SS tube at a pulse-forming capacitance of 1920 pF. (□: CH_4 conversion, ○: Energy efficiency, ◇: C_2H_2 selectivity, △: C_2H_4 selectivity, ▽: C_2H_6 selectivity, ☆: Carbon selectivity, ◁: H_2 selectivity)

At higher power inputs, as shown in Figure 1.8(b), similar trends are observed when the gas flow rate is greater than 4×10^{-5} $m^3 \cdot s^{-1}$. However, at low gas flow rates, the same trends do not hold because a minimum in energy efficiency and a maximum in C_2H_2 selectivity occur and carbon deposition is observed at the lowest gas flow rate. These observations are explained in the following section.

1.3.5 The effect of specific energy input. Specific energy combines the effects of power input and gas flow rate, as shown in Equation 3. Figure 1.9 presents the effect of specific energy input on methane conversion and product selectivity for the entire range of power input and flow rate for the stainless steel cathode.

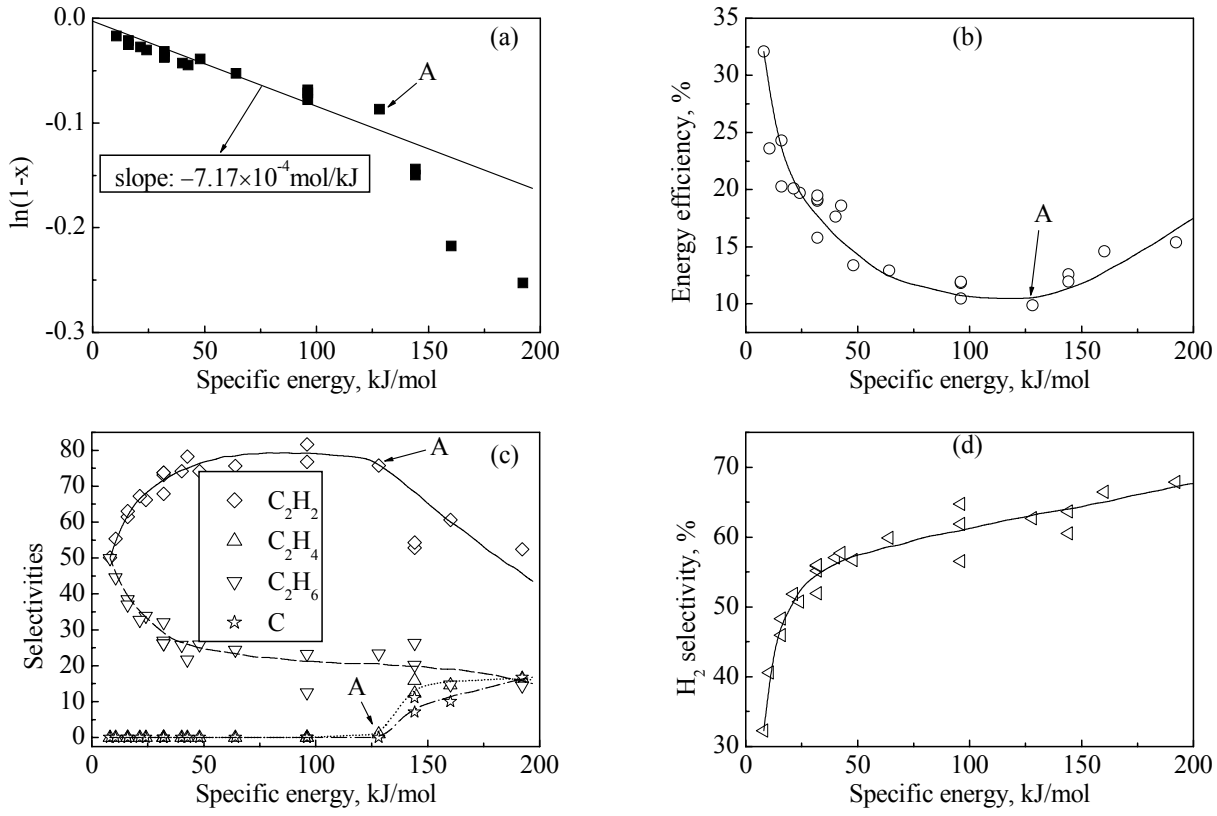

Figure 1.9. The effect of specific energy input on (a) ln(1-X), (b) energy efficiency, (c) acetylene, ethane, ethane, and carbon selectivities, and (d) H_2 selectivity for the SS cathode.

In the PCDR, activation and conversion of methane occur by collision of methane molecules with energetic electrons:[29]

$$CH_4 + e \rightarrow CH_n + (4\text{-}n)H \rightarrow \text{products} \qquad \text{(R11)}$$

During the formation of products shown in R11, methane dehydrogenation is the rate determining step because electron collision reaction of methane determines the subsequent product selectivity and methane reaction rate.[29] Therefore, the net reaction rate for methane conversion can be written as

$$-d[CH_4]/dt = k_0 n_e [CH_4] \qquad (11)$$

where $[CH_4]$ is the mole concentration of methane ($mol \cdot m^{-3}$), n_e is the electron concentration ($mol \cdot m^{-3}$), and k_0 is the rate constant ($m^3 \cdot mol^{-1} \cdot s^{-1}$). Assuming that the electron concentration is proportional to power input,[25] Equation 11 can be solved in terms of methane conversion (X) as

$$\ln(1-X) = -k_0 \cdot \alpha \cdot W \cdot V/u \qquad (12)$$

where α is the proportionality constant for electron concentration with power input and V is the reactor volume. Substituting Equation 3 into Equation 11 produces the following result:

$$\ln(1-X) = -k \cdot E_s \qquad (13)$$

where k is a proportionality constant with units of $mol \cdot kJ^{-1}$.

Figure 1.9(a) shows that ln(1–X) vs. E_s has a linear relationship for specific energies less than about 130 $kJ \cdot mol^{-1}$ (point A). The slope of ln(1–X) vs. E_s in this region is 7.17×10^{-4} $mol \cdot kJ^{-1}$, which provides a value for the proportionality constant, k.

Figure 1.9(b) shows the effect of specific energy input on energy efficiency. Energy efficiency initially decreases with increasing specific energy input until reaching a minimum at ~130 $kJ \cdot mol^{-1}$ (point A) and then increases. Reactor temperature increases with increasing specific energy input, the most pronounced effect being at the outlet. Yao *et al.*[15] found that the

impedance of methane decreases with increasing gas temperature. Low impedance of methane at high temperature leads to more inefficient energy delivery from the external circuit to the reactor. Therefore, energy efficiency initially decreases with increasing specific energy input. However, after the reactor temperature reaches a critical value, thermal reactions, especially dehydrogenation reactions, may begin to be significant because their rates increase exponentially with temperature (e.g., reaction R9).[7] These thermal reactions can further enhance methane conversion. As discussed earlier in association with Figure 1.4, the estimated temperature in the reactor at a specific energy input of 125 $kJ \cdot mol^{-1}$ is 853 K. Therefore, thermal reactions are likely the reason for the observed increase in energy efficiency with increasing specific energy input at high specific energy. If the reactor were adiabatic and all energy input were dissipated in heating the gas, the calculated methane temperature is about 2000 K at a specific energy input of 130 $kJ \cdot mol^{-1}$. The actual temperatures in our non-adiabatic reactor are well below 2000 K, but at an estimated ~853 K, they appear to be high enough to initiate thermal reactions. The onset of thermal reactions would explain the lack of linearity between $\ln(1-X)$ and E_s [Figure 1.9(a)] at specific energy inputs >~130 $kJ \cdot mol^{-1}$ and the resulting minimum value for energy efficiency in methane conversion observed at low gas flowrates (corresponding to high specific energy input) [Figure 1.8(b)].

Figure 1.9(c) shows the effect of specific energy input on selectivity of acetylene, ethylene, ethane and carbon. Acetylene selectivity initially increases with increasing specific energy input, but after reaching a maximum at 130 $kJ \cdot mol^{-1}$ (point A), it decreases with further increases in specific energy. The selectivities for ethylene and carbon are initially zero. Near the point where acetylene selectivity reaches a maximum and begins to decrease, the ethylene and carbon selectivities increase with increasing specific energy input. These results are consistent

with those shown in Figures 1.8(a) and (b), which have been discussed previously. The data imply an increase in ethylene selectivity due to ethane dehydrogenation. At specific energies >~130 kJ·mol^{-1}, dehydrogenation of acetylene apparently results in deposition of carbonaceous residues, consistent with the results of other studies conducted at higher reaction temperatures.[2, 43] Formation of solid carbonaceous deposits from acetylene would also explain the decrease in acetylene selectivity with increasing specific energy. Similar reasoning explains the trend in acetylene selectivity in Figure 1.8(d).

Figure 1.9(d) shows the effect of specific energy input on the hydrogen selectivity. At specific energy inputs less than 50 kJ·mol^{-1}, the hydrogen selectivity increases rapidly with increasing specific energy input, corresponding to the similar increase in acetylene selectivity and the decrease in ethane selectivity shown in Figure 1.9(c). At specific energy inputs greater than 50 kJ·mol^{-1}, the selectivity of hydrogen slowly increases with increasing specific energy input.

Figures 1.10(a) and (b) show a plot of ln(1–X) vs. E_s for the Pt/SS and Nb tubes, respectively. The slope of ln(1–X) vs. E_s for the Pt/SS and Nb tubes are slightly higher than that for the SS tube, supporting the earlier conjecture that the cathode material has only a weak catalytic effect on methane conversion, as illustrated in Figure 1.7.

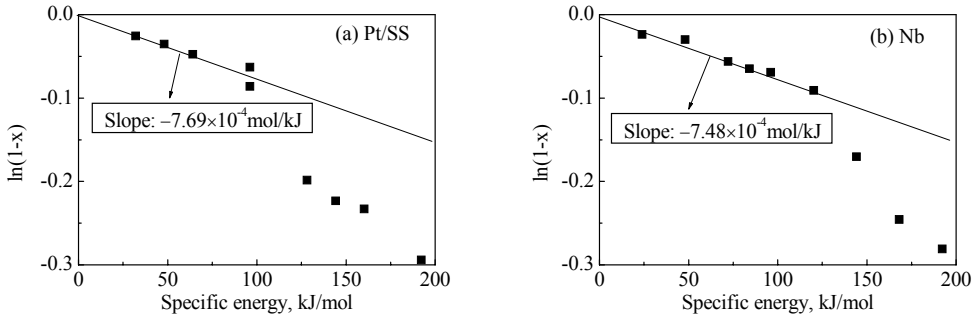

Figure 1.10. Plot of ln(1-X) vs specific energy input (a) Pt/SS tube; (b) Nb tube

Table 1.2 compares energy efficiency and operating conditions for plasma methane conversion in different types of plasma reactors. Microwave discharge and dielectric barrier discharge plasmas have low energy efficiencies (<~3%). For corona discharge reactors, energy efficiency in a PTP reactor with high pulse frequency is highest (~50%),[17] even higher than the commercialized Huels process. However, the PTP reactor is very small and operates with low gas throughput. The reactor in this work processes gas flow rates that are one order of magnitude larger than the PTP reactor studied by Yao *et al.*[15, 17] and over 100 times larger than the PTP reactor used by Kado *et al.*[12] The highest energy efficiency achieved in this study, 33%, is higher than the CAC corona discharge reactor reported by Yao et al[15] and close to that reported for the Huels process. However, methane conversion at this highest energy efficiency is only ~2%, as compared to 70.5% in Huels process.[1]

Table 1.2. Comparison of plasma processes for methane conversion

Literature	Plasma mode	CH_4 flowrate ($mol \cdot s^{-1}$)	Frequency (Hz)	Energy efficiency (%)
Fincke *et al.*[2]	thermal arc	0.098	[-]	25.2
Fincke *et al.*[2]	**thermal arc (Huels process)**	**26.45**	**[-]**	**33.2**
Yao *et al.*[17]	corona discharge (PTP reactor)	2.03×10^{-4}	9.92 k	51.38
Yao *et al.*[15]	corona discharge (CAC reactor)	1.02×10^{-4}	8.0 k	17.69
This work	**corona discharge (CAC reactor)**	**1.60×10^{-3} ~ 6.40×10^{-3}**	**0.1 ~ 1 k**	**10-32**
Yang[5]	Dielectric barrier discharge	4.74×10^{-5}	10 ~ 40 k	<1
Huang and Suib[9]	Microwave	2.07×10^{-5} ~ 2.54×10^{-4}	2.45 G	0.2-3.3

1.4 Conclusions

This work shows that capacitance, cathode material, gas flowrate and specific energy each have an effect on methane conversion, energy efficiency and product selectivity in co-axial cylinder pulsed corona discharge reactors. The formation of ethane and acetylene is apparently the result of dimerization of CH_3 and CH radicals, respectively, while the formation of ethylene results from the dehydrogenation of ethane. At the same power input, low capacitance with high pulse frequency results in for higher methane conversion and energy efficiency than operation at high capacitance with low pulse frequency. Cathodes constructed from platinum coated stainless steel may exhibit a slight catalytic effect on methane conversion. Further, with increasing specific energy input, the energy efficiency for methane conversion has a minimum value, while the selectivity of acetylene has a maximum value. With improved reactor designs, pulsed corona discharge reactors may provide a viable alternative method for methane conversion at low temperatures.

The relative ease of direct methane decomposition indicates that co-processing methane and H_2S to preferentially remove the sulfur as a method of sweetening natural gas may not be feasible. As will be seen in Section 2, the electrical properties of H_2S require more severe reaction conditions compared to methane to initiate decomposition. Under the same reactor operating conditions that produced a strong corona discharge in pure methane, no corona was formed in pure H_2S. Therefore, methane would likely decompose extensively before sufficient amounts of H_2S were removed to meet natural gas pipeline specifications. The potential for producing sulfur-containing hydrocarbons is also high, which would produce unacceptable products. However, the methane experiments provided useful information on the interrelation

among reactor power input, pulse frequency, pulse forming capacitance, and charge voltage to provide direction for the H_2S experiments that are described in Sections 2 and 3.

1.5 References

1. Holmen, A.; Olsvik, O.; Rokstad, O. A., Pyrolysis of natural gas: chemistry and process concepts. *Fuel Processing Technology* **1995,** 42, 249-67.
2. Fincke, J. R.; Anderson, R. P.; Hyde, T.; Detering, B. A.; Wright, R.; Bewley, R. L.; Haggard, D. C.; Swank, W. D., Plasma thermal conversion of methane to acetylene. *Plasma Chemistry and Plasma Processing* **2002,** 22, (1), 105-136.
3. Thanyachotpaiboon, K.; Chavadej, S.; Caldwell, T. A.; Lobban, L. L.; Mallinson, R. G., Conversion of methane to higher hydrocarbons in AC nonequilibrium plasmas. *AIChE Journal* **1998,** 44, (10), 2252-2257.
4. Yang, Y., Methane Conversion and Reforming by Nonthermal Plasma on Pins. *Industrial & Engineering Chemistry Research* **2002,** 41, (24), 5918-5926.
5. Yang, Y., Direct Non-oxidative Methane Conversion by Non-thermal Plasma: Experimental Study. *Plasma Chemistry and Plasma Processing* **2003,** 23, (2), 283-296.
6. Onoe, K.; Fujie, A.; Yamaguchi, T.; Hatano, Y., Selective synthesis of acetylene from methane by microwave plasma reactions. *Fuel* **1997,** 76, (3), 281-282.
7. Heintze, M.; Magureanu, M.; Kettlitz, M., Mechanism of C2 hydrocarbon formation from methane in a pulsed microwave plasma. *Journal of Applied Physics* **2002,** 92, (12), 7022-7031.
8. Heintze, M.; Magureanu, M., Methane conversion into acetylene in a microwave plasma: Optimization of the operating parameters. *Journal of Applied Physics* **2002,** 92, (5), 2276-2283.
9. Huang, J.; Suib, S. L., Dimerization of methane through microwave plasmas. *J. Phys. Chem.* **1993,** 97, (37), 9403-9407.
10. Zhu, A.; Gong, W.; Zhang, X.; Zhang, B., Coupling of methane under pulse corona plasma (I) - in the absence of oxygen. *Science in China, Series B: Chemistry* **2000,** 43, (2), 208-214.
11. Kado, S.; Sekine, Y.; Fujimoto, K., Direct synthesis of acetylene from methane by direct current pulse discharge. *Chemical Communications* **1999**, (24), 2485-2486.
12. Kado, S.; Urasaki, K.; Sekine, Y.; Fujimoto, K.; Nozaki, T.; Okazaki, K., Reaction mechanism of methane activation by using non-equilibrium pulsed discharge at room temperature. *Fuel* **2003,** 82, (18), 2291-2297.
13. Yao, S.; Nakayama, A.; Suzuki, E., Methane conversion using a high-frequency pulsed plasma: discharge features. *AIChE Journal* **2001,** 47, (2), 419-426.
14. Yao, S.; Nakayama, A.; Suzuki, E., Acetylene and hydrogen from pulsed plasma conversion of methane. *Catalysis Today* **2001,** 71, (1-2), 219-223.
15. Yao, S.; Nakayama, A.; Suzuki, E., Methane conversion using a high-frequency pulsed plasma: important factors. *AIChE Journal* **2001,** 47, (2), 413-418.
16. Yao, S. L.; Suzuki, E.; Meng, N.; Nakayama, A., Influence of Rise Time of Pulse Voltage on the Pulsed Plasma Conversion of Methane. *Energy & Fuels* **2001,** 15, (5), 1300-1303.

17. Yao, S. L.; Suzuki, E.; Meng, N.; Nakayama, A., A high-efficiency reactor for the pulsed plasma conversion of methane. *Plasma Chemistry and Plasma Processing* **2002,** 22, (2), 225-237.
18. Yao, S. L.; Suzuki, E.; Nakayama, A., The pyrolysis property of a pulsed plasma of methane. *Plasma Chemistry and Plasma Processing* **2001,** 21, (4), 651-663.
19. Uhm, H. S.; Lee, W. M., An Analytical Theory of Corona Discharge Plasmas. *Phys. Plasmas* **1997,** 4, (9), 3117-3128.
20. Mok, Y. S.; Ham, S. W.; Nam, I. S., Evaluation of Energy Utilization Efficiencies for SO_2 and NO Removal by Pulsed Corona Discharge Process. *Plasma Chemistry and Plasma Processing* **1998,** 18, (4), 535-550.
21. Chung, J. W.; Cho, M. H.; Son, B. H.; Mok, Y. S.; Namkung, W., Study on reduction of energy consumption in pulsed corona discharge process for NOx removal. *Plasma Chemistry and Plasma Processing* **2000,** 20, (4), 495-509.
22. Zhao, G.-B.; Garikipati, S. V. B. J.; Hu, X.; Argyle, M. D.; Radosz, M., Effect of Reactor Configuration on Nitric Oxide Conversion in Nitrogen Plasma. *AIChE J* **2005,** 51, (6), 1813-1821.
23. Luo, J. S., Steven L.; Hayashi, Yuji; Matsumoto, Hiroshige., Emission Spectroscopic Studies of Plasma-Induced NO Decomposition and Water Splitting. *Journal of Physical Chemistry A* **1999,** 103, (31), 6151-6161.
24. Tanaka, S.; Uyama, H.; Matsumoto, O., Synergistic effects of catalysts and plasmas on the synthesis of ammonia and hydrazine. *Plasma Chemistry and Plasma Processing* **1994,** 14, (4), 491-504.
25. Zhao, G.-B.; Hu, X.; Yeung, M. C.; Plumb, O. A.; Radosz, M., Nonthermal Plasma Reactions of Dilute Nitrogen Oxide Mixtures: NO_x in Nitrogen. *Industrial & Engineering Chemistry Research* **2004,** 43, (10), 2315-2323.
26. Hu, X.; Zhao, G.-B.; Legowski, S. F.; Radosz, M., Moisture Effect on NOx Conversion in a Nonthermal Plasma Reactor. *Environmental Engineering Science* **2005,** 22, (6), 854-869.
27. Didden, C.; Duisings, J., On-line measurement of a liquid reactor feed with a mass spectrometer. *Process Control and Quality* **1992,** 3, (1-4), 263-271.
28. Zhao, G.-B.; Garikipati, S. V. B. J.; Hu, X.; Argyle, M. D.; Radosz, M., The Effect of Gas Pressure on NO Conversion Energy Efficiency in Nonthermal Nitrogen Plasma. *Chem. Eng. Sci.* **2005,** 60, (7), 1927-1937.
29. Kirikov, A. V.; Ryzhov, V. V.; Suslov, A. I., Kinetics of free radicals in the plasma of a spark discharge in methane. *Technical Physics Letters* **1999,** 25, (10), 794-795.
30. Denisov, G. V.; Kuznetsov, D. L.; Novoselov, Y. N.; Tkachenko, R. M., Influence of the parameters of a pulsed electron beam on the removal of nitrogen oxides from flue gases. *Technical Physics Letters* **1998,** 24, (8), 601-602.
31. Baulch, D. L.; Cobos, C. J.; Cox, R. A.; Esser, C.; Frank, P.; Just, T.; Kerr, J. A.; Pilling, M. J.; Troe, J.; al., e., Evaluated kinetic data for combustion modeling. *Journal of Physical and Chemical Reference Data* **1992,** 21, (3), 411-734.
32. Zhao, G.-B.; Hu, X.; Plumb, O. A.; Radosz, M., Energy Consumption and Optimal Reactor Configuration for Nonthermal Plasma Conversion of N_2O in Nitrogen and N_2O in Argon. *Energy & Fuels* **2004,** 18, (5), 1522-1530.
33. Zhao, G.-B.; Hu, X.; Argyle, M. D.; Radosz, M., Effect of CO_2 on Nonthermal-Plasma Reactions of Nitrogen Oxides in N_2. Part II: Percent-level Concentrations. *Ind. Eng. Chem. Res.* **2005,** 44, (11), 3935-3946.

34. Zhao, G.-B.; Hu, X.; Argyle, M. D.; Radosz, M., Effect of CO_2 on Nonthermal-Plasma Reactions of Nitrogen Oxides in N_2. Part I: ppm-level Concentrations. *Ind. Eng. Chem. Res.* **2005,** 44, (11), 3925-3934.
35. Zhao, G.-B.; Hu, X.; Argyle, M. D.; Radosz, M., N Atom Radicals and $N_2(A^3\Sigma_u^+)$ Found to be Responsible for Nitrogen Oxides Conversion in Non-thermal Nitrogen Plasma. *Ind. Eng. Chem. Res.* **2004,** 43, (17), 5077-5088.
36. Zhao, G.-B.; Garikipati, S. V. B. J.; Hu, X.; Argyle, M. D.; Radosz, M., Effect of Oxygen on Nonthermal-Plasma Reactions of Nitrogen Oxides in Ntrogen. *AIChE J* **2005,** 51, (6), 1800-1812.
37. Zhao, G.-B.; Argyle, M. D.; Radosz, M., Effect of CO on Conversion of NO and N_2O in Nonthermal Argon Plasma. *Journal of Applied Physics* **2006,** 99, (11), 113302/1-113302/14.
38. Shin, D. N.; Park, C. W.; Hahn, J. W., Detection of $OH(A^2\Sigma^+)$ and $O(^1D)$ emission spectrum generated in a pulsed corona plasma. *Bulletin of the Korean Chemical Society* **2000,** 21, (2), 228-232.
39. Eswaramoorthy, M.; Niwa, S.; Toba, M.; Shimada, H.; Raj, A.; Mizukami, F., The conversion of methane with silica-supported platinum catalysts: the effect of catalyst preparation method and platinum particle size. *Catalysis Letters* **2001?,** 71, (1-2), 55-62.
40. Souza, M. M. V. M.; Schmal, M., Methane Conversion to Synthesis Gas by partial Oxidation and CO_2 Reforming over Supported Platinum Catalysts. *Catalysis Letters* **2003,** 91, (1-2), 11-17.
41. Waku, T.; Biscardi, J. A.; Iglesia, E., Catalytic dehydrogenation of alkanes on Pt/Na-[Fe]ZSM5 and staged O_2 introduction for selective H_2 removal. *Journal of Catalysis* **2004,** 222, (2), 481-492.
42. Eichwald, O.; Yousfi, M.; Hennad, A.; Benabdessadok, M. D., Coupling of Chemical Kinetics, Gas Dynamics, and Charged Particle Kinetics Models for the Analysis of NO Reduction from Flue Gases. *J. Appl. Phys.* **1997,** 82, (10), 4781-4794.
43. Blitz, M. A.; Beasley, M. S.; Pilling, M. J.; Robertson, S. H., Formation of the propargyl radical in the reaction of $^1CH_2$ and C_2H_2: experiment and modeling. *Physical Chemistry Chemical Physics* **2000,** 2, (4), 805-812.

Section 2

Breakdown voltages and H_2S conversions for various concentrations of H_2S in balance gases (Ar, He, N_2 and H_2)

2.1 Introduction

Direct dissociation of H_2S has been investigated using various plasma processing technologies, including arc discharge or thermal plasmas, microwave plasma, glow discharge, silent discharge, and pulsed corona discharge. Dalaine et al.[15,16] investigated H_2S conversion in gas systems with 0-100 ppm H_2S in air using gliding arc discharges. This type of reactor is rather inefficient, with an energy consumption of 500 eV/H_2S molecule dissociated. The theoretical minimum energy requirement for the decomposition of H_2S is over three orders of magnitude less than this. For the reaction: $H_2S(g) \rightarrow H_2(g) + S(s)$, $\Delta H_{298} = 0.21$ eV/H_2S = 20.3 kJ/mol. A large amount of work on microwave decomposition of H_2S has been carried out in former Soviet Union,[3,5,6,7,8,9], where both laboratory and pilot units were reportedly used for the decomposition of pure H_2S or mixtures with CO_2 with a very low energy consumptions of ~0.76 eV/H_2S. Encouraged by these reports of high conversions and low energy requirements, a joint project for H_2S conversion using microwave plasmas was undertaken by The Alberta Hydrogen Research Program, the Atomic Energy of Canada, and Shell Canada Limited. Unfortunately, this group reported the energy consumption for H_2S conversion to be about 4.5 eV/H_2S[14] and thus was unable to reproduce the low energy consumption reported by the Russian researchers. All microwave plasma experiments for H_2S conversion were performed at pressures below 1 atmosphere, which requires additional energy consumption for compression and vacuum costs. Traus et al.[33,34] investigated conversion of H_2S at 10-100% concentrations in Ar, N_2, and H_2 in a silent discharge reactor and a rotating glow discharge reactor. They concluded that the energy consumption for H_2S conversion in a rotating glow discharge reactor (~27 eV/H_2S) is less than

that in a silent discharge reactor (~81 eV/H_2S). In addition, Abolentsev et al.[1] and Ma et al.[25] investigated decomposition of low (ppm) concentrations of H_2S in different balance gases including air, N_2, H_2, He, and CH_4 using a silent discharge reactor. H_2S conversion in pulsed corona discharge reactors was also investigated by several investigators.[4,21,28,38] These investigations were conducted at low H_2S concentrations (<2%) with high (>100 eV/H_2S) energy consumption, which are not practical conditions for commercial application.

Despite this extensive research on H_2S conversion, many questions remain unanswered. First, all of the research described above has been performed either below atmospheric pressure or at low H_2S concentrations (<2%). H_2S conversion at pressures above atmospheric and at high H_2S concentrations is desirable to determine if nonthermal plasmas have potential for industrial application.

Second, there are no reports on the breakdown voltage of H_2S at pressures higher than atmospheric and H_2S concentrations >2%. Gases at normal temperatures and pressures contain very low concentrations of current carriers (free electrons and ions) and therefore behave as insulators. In an electric field, any electrons or ions present are accelerated over a distance corresponding to their mean free path between collisions. If they gain enough kinetic energy to ionize gas molecules, they create new current carriers which in turn ionize more molecules. This avalanche-like process forms channels of conducting plasma called streamers. The electrical resistance of the gas between the electrodes becomes nearly zero. This transition of a gas between the insulating and conducting states is known as breakdown. The voltage at which it occurs is called the breakdown voltage. The specific breakdown voltage depends on the gas, as well as on the electrode geometry, the electrode composition, and the gas pressure.[24] Breakdown voltage data are important because they define the operating limits for the reaction. H_2S is an

electronegative gas with a high dielectric strength of about 2.9.[12] Common gases like air, N_2, H_2, He, and Ar have very low dielectric strengths of 1, 1, 0.5, 0.15, 0.18, respectively.[24] Therefore, much higher applied voltages are required for electrical breakdown of H_2S compared to these gases in the same reactor geometry. In addition, electrons are accelerated over the mean free path of gas molecules during the process of electrical breakdown.[41] As the mean free path of gas molecules increases with decreasing gas pressure, individual electrons gain more kinetic energy in low pressure plasmas than in high pressure plasmas under otherwise similar operating conditions,[41] which causes the breakdown voltage of a gas to decrease with decreasing gas pressure. Therefore, the electrical breakdown of H_2S at either low pressure or low H_2S concentration in a balance gas with a low dielectric strength is comparatively easy, whereas, the electrical breakdown of H_2S at pressures above atmospheric and at high H_2S concentrations is more difficult.

Third, the mechanism of H_2S conversion in the plasma is not clear. Since the ionization potential of H_2S (10.4 eV) is considerably lower than He (24.6 eV), Ar (15.8 eV), N_2 (15.6 eV), H_2 (15.4 eV), CH_4 (12.6 eV), O_2 (12.1 eV), and H_2O (12.6 eV), [24] Ma et al.[25] and Helfritch[21] proposed that the H_2S conversion mechanism in any of these gases involves ionization of H_2S ($e + H_2S \rightarrow H_2S^+ + 2e$) and subsequent charge neutralization with dissociation ($H_2S^+ + e \rightarrow HS + H$). Abolentsev et al.[1] proposed an alternate three step mechanism for H_2S conversion: (1) the balance gas (M) is ionized to M^+, (2) H_2S^+ is formed by charge transfer reaction ($M^+ + H_2S \rightarrow M + H_2S^+$), and (3) H_2S is dissociated by reaction with an ionized H_2S molecule ($H_2S^+ + H_2S \rightarrow H_3S^+ + HS$). However, neither of these mechanisms may appropriately represent the actual process because the ionization degree in nonthermal plasmas is quite low. A recent investigation by Zhao et al.[44] showed that ionization reactions in nonthermal plasmas are negligible.

Alternately, Traus et al.[33,34] proposed that radicals, such as H and HS, formed in the plasma are responsible for H_2S conversion.

2.2 Experimental

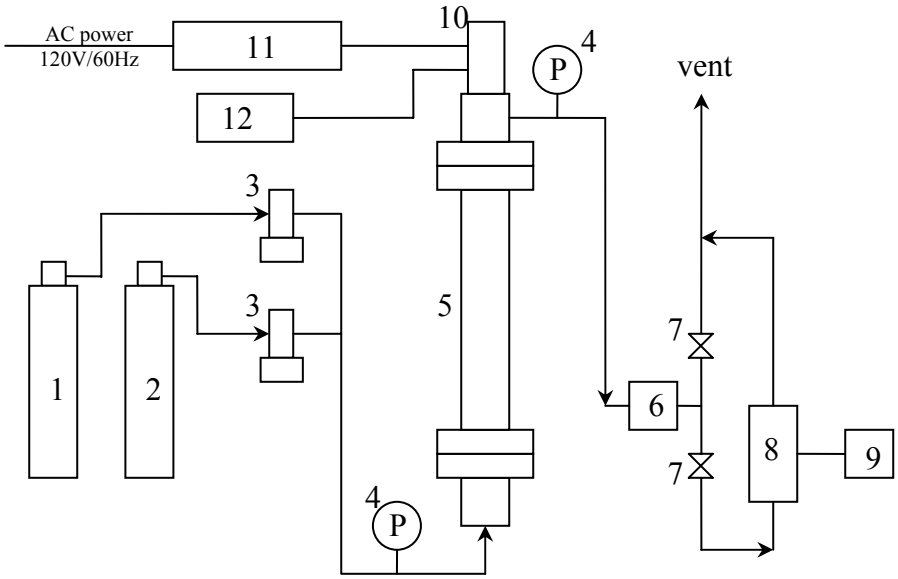

Figure 2.1. Experimental setup
1. H_2S gas cylinder, 2. balance gas cylinder (Ar, He, N_2, H_2), 3. mass flow controller, 4. pressure gauge, 5. pulsed corona discharge reactor, 6. sulfur condenser, 7. valve, 8. RGA, 9. data collection computer, 10. thyratron switch, 11. HV power supply and control circuit, 12. discharge waveform recorder.

Figure 2.1 shows a diagram of the experimental system. The system consists of a reactor with an electrical system built around a thyratron switch, a flow control and distribution system, and a gas sampling system. The reactor was oriented vertically, with the gas flow from bottom to top. The electrical system can deliver charge voltages from 6.9 kV to 30 kV at pulse frequencies from 0 to 1000 Hz. The capacitor bank provides space for four doorknob capacitors in increments of 640 pF. The capacitors were charged to the desired voltage using a 40 kV oil-cooled high voltage power supply. On triggering the thyratron, the stored energy in the capacitors is discharged in a few nanoseconds to the anode, giving rise to a high rate of change

of voltage (dv/dt) on the anode. This process of charging and discharging the capacitors is repeated based on the thyratron trigger frequency leading to sustained current streamers or plasma. Electrical breakdown during corona discharge can be detected by a discharge waveform recorder. The cathode was a stainless steel tube with 0.024 m in diameter and 0.914 m in length, while the anode was a stainless steel wire 0.001 m in diameter passing axially through the center of the tube. The wire was positively charged, while the tube was grounded. The gas flowing through the reactor tube was converted to plasma by the high voltage discharge from the reactor anode. A sulfur trap immersed in ice water at the reactor discharge was filled with stainless steel wool to enhance heat transfer and surface area for sulfur vapor removal from the exit gas.

The four gas mixtures of H_2S in Ar, H_2S in He, H_2S in N_2, and H_2S in H_2 were prepared by mixing ultra high purity (UHP) H_2S with the UHP balance gas. Gas mixtures flowed through PCDR at entrance conditions of ambient temperature (~300K) and a controlled pressure. The highest pressure used in this work was 5.0 bar. The desired entrance mole fraction of H_2S was achieved by setting flowrates of H_2S and the balance gas using two well-calibrated mass flow controllers. The energy released by the capacitors per pulse was calculated from $\frac{1}{2}CV_c^2$, where C is the pulse forming capacitance, fixed at 1920 PF in this work, and V_c is the constant charge voltage before discharge. The power consumed, W ($J \cdot s^{-1}$), was calculated as the product of the input energy per pulse and the pulse frequency, $\frac{1}{2}fCV_c^2$, where f is the pulse frequency in Hz. The gas leaving the sulfur condenser was analyzed using an online Residual Gas Analyzer (RGA, Stanford Research Systems, Inc. QMS100), which is a quadrupole mass spectrometer. To perform quantitative measurements, an internal standard method[37] was used to calibrate the ion signal response at an m/z ratio of 34 with the H_2S mole fraction, in which the balance gas was used as an internal standard. The calibration results are shown in Figure 2.2.

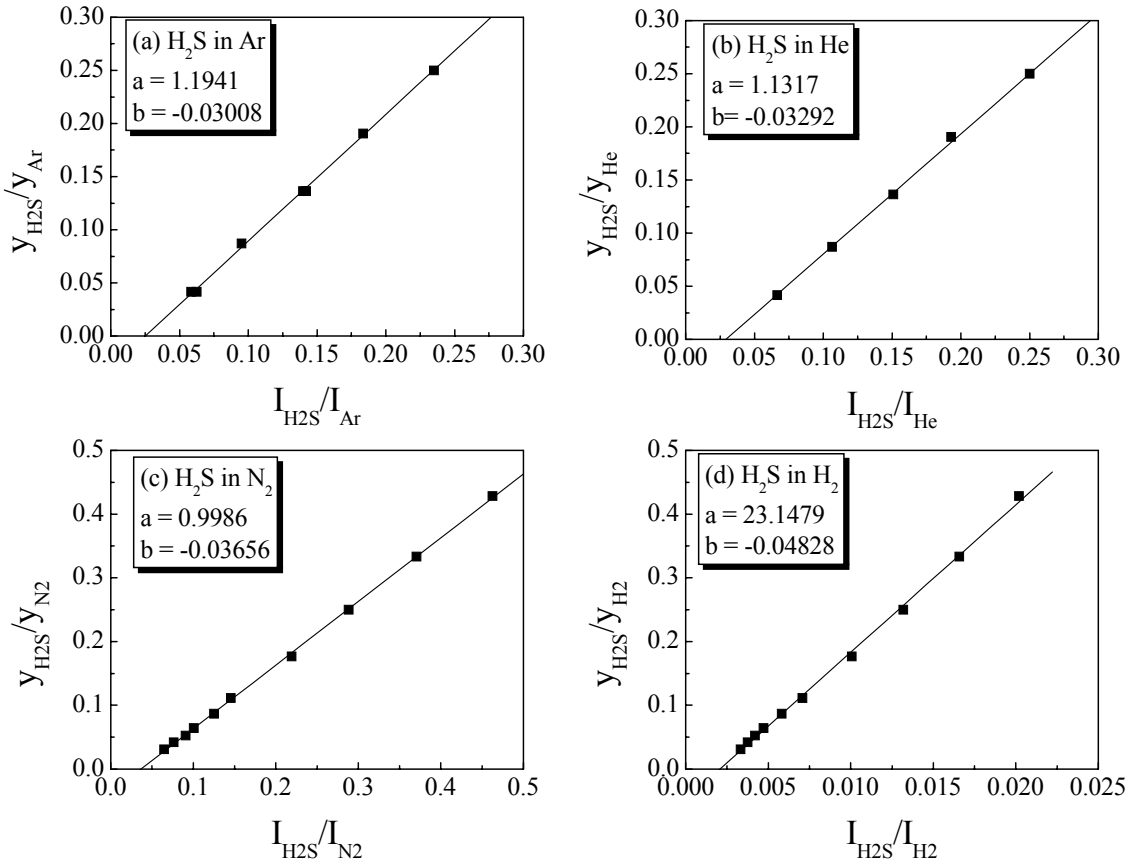

Figure 2.2. Calibration plots for H_2S relative to the balance gas used as an internal standard.

Figure 2.2 shows the ratio of the H_2S and balance gas mole fractions as a function of the measured H_2S and balance gas intensities, which show a linear relationship:

$$\frac{y_{H_2S}}{y_B} = a \cdot \frac{I_{H_2S}}{I_B} + b \tag{1}$$

where y is the mole fraction of gas, I is the ion current from RGA, and the subscript B represents the balance gas of Ar, He, N_2, of H_2. Therefore, the measured ion current ratio of H_2S and the balance gas can be used to determine the mole fraction ratio, K, of H_2S and the balance gas from Figure 2.2. For a binary gas mixture at the reactor entrance, the mole fraction of H_2S and the balance gas can be calculated from

$$y_{i,H_2S} = \frac{K_i}{K_i + 1} \tag{2}$$

$$y_{i,B} = \frac{1}{K_i + 1} \tag{3}$$

where the subscript i represents the inlet gas. When the corona discharge is on, H_2S dissociates into H_2 and sulfur. For the balance gases Ar, He, and N_2, the effluent gas mixture is the ternary system including H_2 because sulfur is captured by the sulfur condenser. However, the mole fraction of balance gas at the reactor outlet is the same as that at the reactor inlet because H_2S dissociation is an equimolar gas phase reaction when the sulfur product is condensed. The outlet H_2S mole fraction can be determined from

$$y_{o,H_2S} = K_o \cdot y_{i,B} \tag{4}$$

where the subscript o represents the outlet gas. For the balance gas H_2, the outlet H_2S mole fraction is

$$y_{o,H_2S} = \frac{K_o}{K_o + 1} \tag{5}$$

Therefore, the conversion of H_2S in the PCDR is calculated from

$$X_{H_2S} = \frac{y_{i,H_2S} - y_{o,H_2S}}{y_{i,H_2S}} \tag{6}$$

Conversion rate and energy consumption of H_2S conversion are calculated from

$$r = \frac{PF}{RT} \cdot y_{i,H_2S} \cdot X_{H_2S} \ (\text{mol} \cdot \text{s}^{-1}) \tag{7}$$

$$En = \frac{W}{r} \cdot 1.0364 \times 10^{-5} \ (\text{eV} \cdot \text{molecule}^{-1}) \tag{8}$$

where P is the gas pressure, F is the gas flowrate, T is the temperature, and R is the gas constant.

For each parameter set, at least two experiments were performed to assure that the results are repeatable. All experimental data were reproducible within a ±10% error limit, including the RGA and flow measurement uncertainties.

2.3 Results and Discussion

2.3.1 Breakdown voltage of H_2S in the various balance gases. Gas breakdown voltage depends on the specific reactor configuration, especially the electrode configuration and structure. Breakdown voltages of many pure gases have been investigated in both uniform and non-uniform fields[11]. For uniform fields, the breakdown voltage usually follows Paschen's law, which states that breakdown voltage, V_b, is a function of nd only, where n is the gas number density (molecules·cm^{-3}) and d is the distance between the electrodes. For non-uniform fields, the breakdown voltage is a function of nr, where r is the radius of curvature of the electrode surface at the point where the highest value of the electric field strength occurs.[11] For the PCDR used in this work, r is the radius of wire anode. For many pure gases in non-uniform fields, the breakdown voltage is proportional to nr at pressures higher than 0.5 bar.[11]

Gas breakdown can be detected by the discharge waveform recorder, shown in Figure 2.1. In addition, the discharge noise from PCDR can also be clearly heard when the corona discharge occurs. The breakdown voltage was determined by increasing the charge voltage in increments of 0.1 kV from a low value at which no discharge occurs until the discharge is detected by both the discharge waveform recorder and the audible noise from the reactor. The measured breakdown voltages at different pressures for pure Ar, H_2, and N_2 are shown in Figure 2.3. For this reactor, the anode radius, r, is 0.0005 m and the inlet temperature is 300 K. At these conditions, nr is proportional to gas pressure. The results presented in Figure 2.3 show that breakdown voltage is proportional to gas pressure, which is consistent with previous reports.[11]

Breakdown voltages of pure N_2 measured at flow rates of 1.18×10^{-4} SCM·s^{-1} and 7.87×10^{-6} SCM·s^{-1} are almost the same, which indicates no effect of gas flowrate on breakdown voltage. In addition, pulse frequencies above 300 Hz do not affect breakdown voltage.

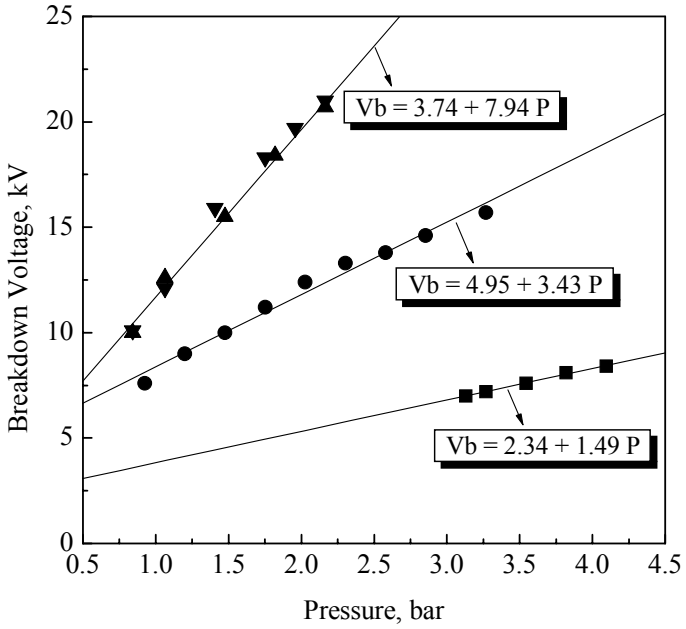

Figure 2.3. Breakdown voltage of pure gases as a function of pressure.
(■): Ar at 1.18×10^{-4} SCM·s^{-1} and 400 Hz; (●): H_2 at 1.18×10^{-4} SCM·s^{-1} and 400 Hz; (▲): N_2 at 1.18×10^{-4} SCM·s^{-1} and 400 Hz; (▼): N_2 at 7.87×10^{-6} SCM·s^{-1} and 400 Hz

Breakdown of pure He occurred at any pressure from 0.8 to 5.0 bar at the lowest charge voltage of 6.9 kV used in this work. However, breakdown of pure H_2S did not occur over the entire operation range for our reactor, which included pressures from 0.8 to 5.0 bar and charge voltages from 6.9 to 30 kV. These results and results in Figure 2.3 indicate that the order of increasing breakdown voltage at constant pressure is: He < Ar < H_2 < N_2 < H_2S, which is consistent with the order of increasing dielectric strength of these gases[12,24] (dielectric strength of He: 0.15, Ar: 0.18, H_2: 0.50, N_2: 1.0, H_2S: 2.9).

Because no corona was formed in pure H_2S at the maximum charge voltage (30 kV) with this reactor geometry, H_2S was mixed with another gas with lower dielectric strength to initiate electrical discharge. He, Ar, N_2, and H_2 were used as balance gases in this work because they do not produce byproducts in the corona.

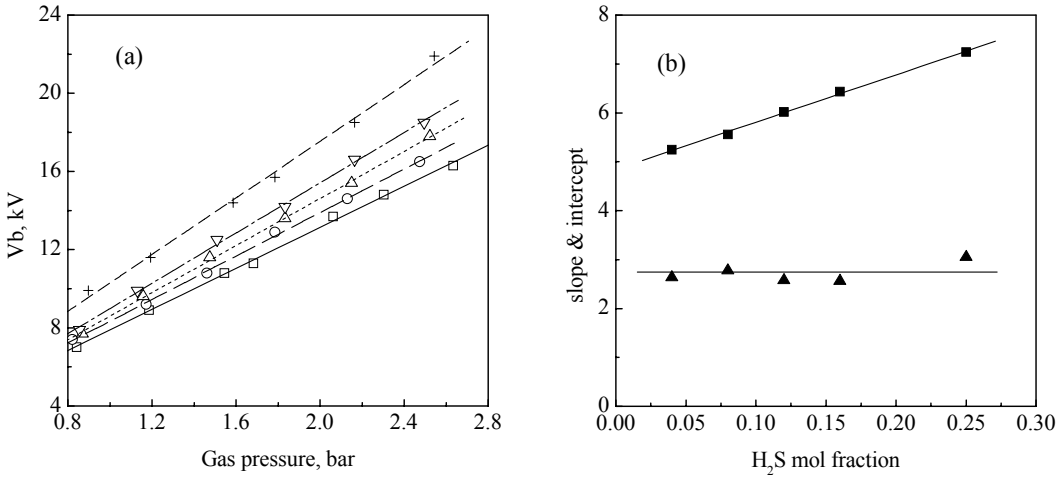

Figure 2.4. Breakdown voltage of H_2S in H_2. (a) Breakdown voltage as a function of total gas pressure. Experimental data: (□): 4% H_2S, (○): 8% H_2S, (△): 12% H_2S, (▽): 16% H_2S, (+): 25% H_2S; linear regression: (—): 4% H_2S, (– –): 8% H_2S, (···): 12% H_2S, (– · –): 16% H_2S, (---): 25% H_2S. (b) Slope and intercept from linear regression in (a) as a function of H_2S mole fraction. (■): slope m_i; (▲): intercept n_i.

As neither gas flowrate nor pulse frequency (>300 Hz) affect breakdown voltage, gas breakdown experiments were performed at a fixed gas flowrate of 1.18×10^{-4} SCM·s^{-1} and a pulse frequency of 400 Hz. Figure 2.4 shows the breakdown voltage of H_2S in H_2. At each fixed H_2S concentration, the breakdown voltage is proportional to total gas pressure, as shown in Figure 2.4(a), according to

$$V_b = m_i \cdot P_t + n_i \tag{9}$$

where P_t is the total gas pressure in bar and m_i and n_i are the slope and the intercept at a specific H_2S mole fraction, respectively. Figure 2.4(b) shows the slope m_i and the intercept n_i as a

function of H_2S mole fraction. These results show that the slope m_i is proportional to H_2S mole fraction and the intercept n_i is essentially constant. Therefore Equation (9) can be rewritten as

$$V_b = (a_1 \cdot y_{H_2S} + b_1) \cdot P_t + n = a_1 \cdot P_{H_2S} + b_1 \cdot (P_{H_2S} + P_{H_2}) + n \qquad (10)$$

where a_1 and b_1 are the slope and the intercept for the linear relationship of m_i and H_2S mole fraction, respectively, and P_{H_2S} and P_{H_2} are the partial pressure of H_2S and H_2, respectively. Equation 10 can be further simplified as

$$V_b = a_2 \cdot P_{H_2S} + b_2 \cdot P_{H_2} + c \qquad (0.8 \text{ bar} < P_t < 3.6 \text{ bar}) \qquad (11)$$

where $a_2 = a_1 + b_1$, $b_2 = b_1$, and $c = n$. Equation (11) indicates that breakdown voltage is proportional to the partial pressures of the components in binary gas mixtures. Parameters a_2, b_2, and c were obtained through a least-square regression analysis by application of Equation (11) to mixtures of H_2S in Ar, H_2S in He, H_2S in N_2, and H_2S in H_2,. The breakdown voltages (V_b) are,

H_2S in Ar: V_b (kV) = 22.2 × P_{H_2S} (bar) + 2.52 × P_{Ar} (bar) + 6.48 (12a)

H_2S in He: V_b (kV) = 16.2 × P_{H_2S} (bar) + 2.42 × P_{He} (bar) + 3.35 (12b)

H_2S in N_2: V_b (kV) = 16.1 × P_{H_2S} (bar) + 6.44 × P_{N_2} (bar) + 4.00 (12c)

H_2S in H_2: V_b (kV) = 15.2 × P_{H_2S} (bar) + 4.74 × P_{H_2} (bar) + 2.70 (12d)

These correlations are valid for total absolute pressures between 0.8 and 3.6 bar and geometrically similar coaxial cylinder reactor systems. Figure 2.5 shows the experimental results and the fitted data using Equations 12(a)-(d). Most experimental data matched the fitted data, except for low concentrations (<4%) of H_2S in Ar. In this exceptional case, an increase in gas pressure causes the breakdown voltage to deviate from linearity at intermediate pressures

before returning to linearity with a similar slope with a new intercept. Similar experimental results are obtained for 2% H_2S in Ar, but the reason for this exception is not yet clear.

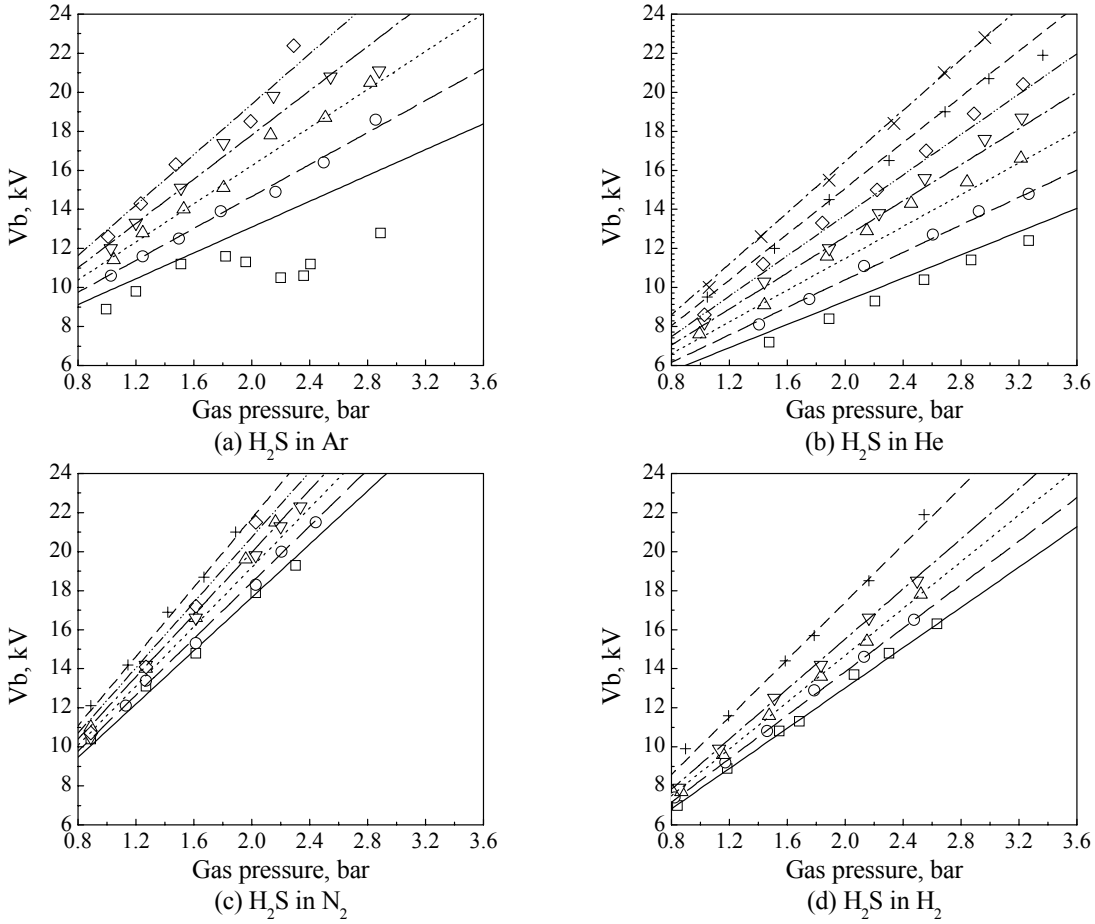

Figure 2.5. Breakdown voltage as a function of total gas pressure (a) H_2S in Ar; (b) H_2S in He; (c) H_2S in N_2; (d) H_2S in H_2. Experimental data: (□): 4% H_2S; (○): 8% H_2S; (△): 12% H_2S; (▽): 16% H_2S; (◇): 20% H_2S; (+): 25% H_2S; (×): 30% H_2S**.** Calculated data: (—): 4% H_2S; (– –): 8% H_2S; (···): 12% H_2S; (– · –): 16% H_2S; (– · · –): 20% H_2S; (---): 25% H_2S; (- · -): 30% H_2S.

2.3.2 H_2S conversion in various balance gases. Experiments on H_2S conversion in Ar, He, N_2, and H_2 were carried out at a fixed pulse frequency of 400 Hz, charge voltage of 17 kV (corresponding to power input of 110 W), reactor pressure of 1.34 bar, and gas flowrate of 1.18 $\times$ 10^{-4} SCM·s^{-1}, corresponding to a gas residence time of 4.25 s in the reactor. As shown in

Figure 2.5, the charge voltage of 17 kV is higher than all breakdown voltages for gas mixtures of H_2S in Ar, H_2S in He, H_2S in N_2, and H_2S in H_2 at the total pressure of 1.34 bar, which confirmed that electrical discharges occur. Sulfur deposits in the sulfur condenser, as well as the reactor tube and outlet, further confirmed the active discharge. The presence of sulfur was confirmed by energy dispersive spectroscopy. The first two principal peaks for orthorhombic α-sulfur were observed in the X-ray diffraction data.

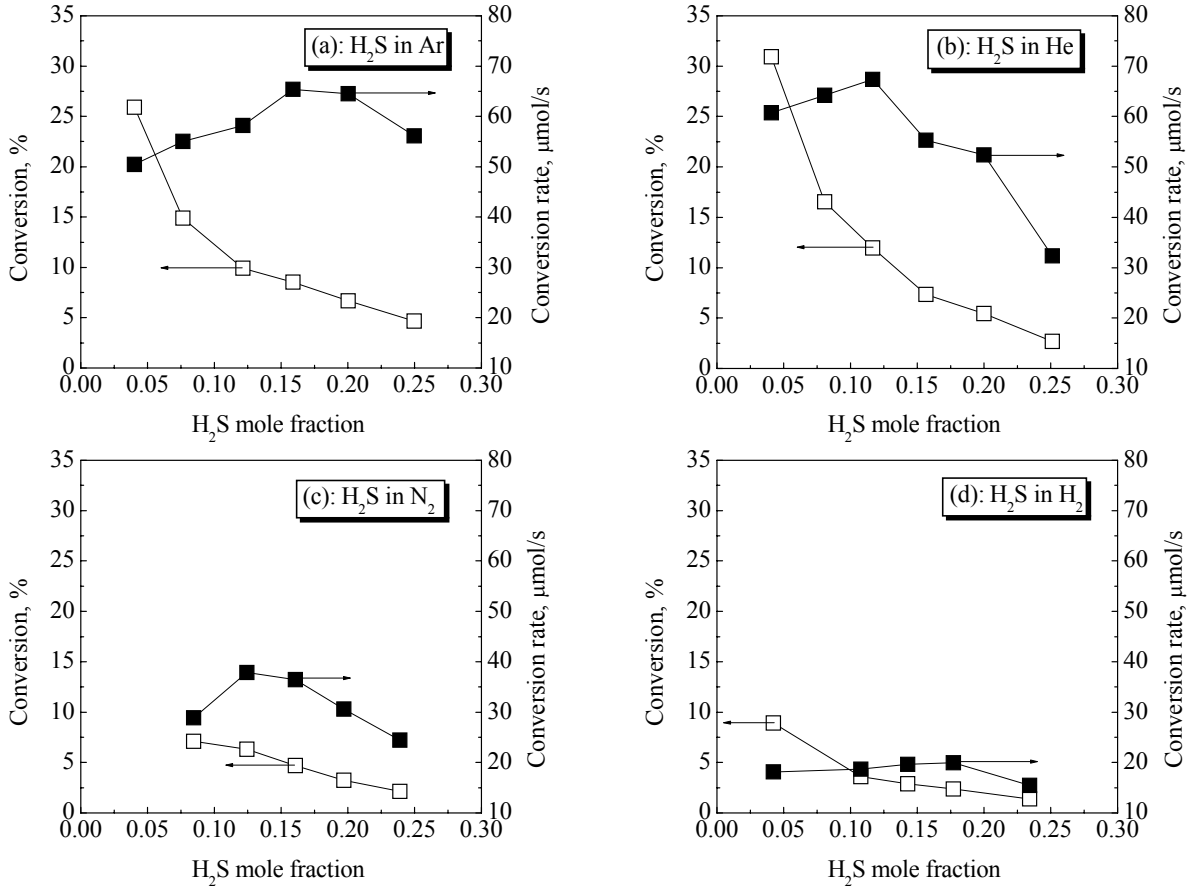

Figure 2.6. H_2S conversion and conversion rate as a function of H_2S mole fraction in different balance gases. (□): conversion, (■): conversion rate

Figures 2.7(a)-(d) show H_2S conversion and rate data as a function of initial H_2S mole fraction. Similar trends of conversion and rate for gas mixtures of H_2S in Ar, H_2S in He, H_2S in N_2, and H_2S in H_2 are found. H_2S conversion decreases with increasing H_2S mole fraction, while

the rate initially increases, reaches a maximum, and then decreases with increasing H_2S mole fraction.

There are four proposed mechanisms for H_2S conversion in nonthermal plasmas.

(I) Direct ionization of H_2S followed by dissociative recombination:[21,25]

$$e + H_2S \rightarrow H_2S^+ + 2e \quad \text{(R1)}$$

$$H_2S^+ + e \rightarrow HS + H \quad \text{(R2)}$$

(II) Ionization of the balance gas (M), leading to the charge transfer, and subsequent dissociative recombination:[1]

$$e + M \rightarrow M^+ + 2e \quad \text{(R3)}$$

$$M^+ + H_2S \rightarrow H_2S^+ + M \quad \text{(R4)}$$

$$H_2S^+ + e \rightarrow HS + H \quad \text{(R2)}$$

(III) Direct electron collision dissociation of H_2S:

$$e + H_2S \rightarrow HS + H + e \quad \text{(R5)}$$

(IV) Electron collision dissociation or excitation of the balance gas, which produces active species that contribute to H_2S dissociation:

$$e + M \rightarrow M^* + e \quad \text{(R6)}$$

$$M^* + H_2S \rightarrow H + HS + M \quad \text{(R7)}$$

Pathways (I) and (II) are unlikely for H_2S conversion for the following reasons:

(1) If pathway (I) is responsible for H_2S conversion, an increasing number of H_2S molecules should be ionized with increasing H_2S concentration, which should lead to increasing H_2S conversion rate with increasing H_2S concentration. This effect is not observed, as shown in Figure 2.6.

(2) If pathway (II) is responsible for H_2S conversion, then the ionization energies of the balance gases must be reasonably achieved within the reactor. However, this is not the case, as shown by the following example using He, which has an ionization energy of 24.6 eV/He or 2370 kJ/mol He. At 110 W power input, if the whole energy input is assumed to be absorbed by He to form He^+, the limiting conversion rate of H_2S is 46.3 μmol/s. However, the results presented in Figure 2.6(b) show that most H_2S conversion rates are larger than 46.3 μmol/s, which leaves pathway II unable to explain all of the observed H_2S conversion.

(3) As shown in our recent investigation,[44] the degree of ionization in the pulsed corona discharge is low. The major active species are produced through electron collision in the streamers, whose total volume is 10^{-4}-10^{-3} of the reactor volume.[35] In the streamer head, the concentration of ions (corresponding to concentration of electrons) is around 15 ppm.[44] If pathways (I) and (II) are responsible for H_2S conversion and all cations formed from reactions R1 and R3 contribute to H_2S conversion, the conversion of H_2S for initial mole fractions of 0.04 is 400 Hz × 4.25 s × 15 ppm × (10^{-4}-10^{-3}) /0.04 = 0.064-0.0064%, which is at least two orders of magnitude lower than conversion of H_2S observed during the experiments, as shown in Figure 2.6. Therefore, the observed H_2S conversion solely through ionic reactions is not possible.

Conversion of H_2S through pathways (III) and (IV) can be supported by the following points:

(1) As demonstrated by Eliasson and Kogelschatz,[18,19] the concentration of radicals and excited states formed from electron collision reactions in the streamer head are at least two orders of magnitude higher than that of ions. In the streamer channel, the concentration of radicals and excited states formed from electron collision reactions is at least four orders of magnitude higher than that of ions. Most reactions are known to occur in the streamer channel.[44]

Therefore, if reactions R5-R7 contribute to H_2S conversion, the conversion of H_2S for initial mole fractions of 0.04 is 400 Hz × 4.25 s × (10^4 × 15 ppm) × (10^{-4}-10^{-3})/0.04 = ~64%, which is higher than all the experimental results shown in Figure 2.6. This is reasonable because the efficiency of such plasma reactions is less than 100%.

(2) The occurrence of H_2S conversion through direct electron collision reaction R5 is suggested by the experimental data on H_2S conversion in He. Our previous study of Ar in PCDR's[46] showed that the main active species formed during electron collision reactions with Ar are excited states and not cations. By analogy, the main active species contributing to H_2S conversion formed from electron collision reaction with He are assumed to be excited states of He and the contribution of ions to H_2S conversion in He is excluded from consideration. The first electronic excited state of He, He(2^3S_1), has an excitation energy of 19.82 eV.[27] If the excited states of He were the only active species contributing to H_2S (R6 and R7), the highest conversion rate of H_2S in He is 110 W/(19.82 × 96.5 kJ/mol) = 57.5 μmol/s. However, for concentrations of H_2S in He less than 12%, the conversion rates of H_2S are all higher than 57.5 μmol/s, which indicates that direct electron collision reaction of H_2S (R5) must contribute to H_2S conversion in addition to the He excited states.

The observed maximum in H_2S conversion rate in Ar, He, N_2, and H_2 with increasing mole fraction of H_2S can be explained through pathways (III) and (IV). For H_2S in Ar, previous investigation[46] has shown that the major product for direct electron collisions with Ar is the lowest excited state of Ar, Ar($^3P_2$), which has an excitation energy of 11.55 eV.

$$e + Ar \rightarrow Ar(^3P_2) + e \qquad \text{(R8)}$$

Ar($^3P_2$) contributes to H_2S dissociation and H_2 dissociation as follows:[20,36]

$$Ar(^3P_2) + H_2S \rightarrow Ar + H + HS \qquad k = 5.18 \times 10^{14}\ cm^3 \cdot mol^{-1} \cdot s^{-1} \qquad (R9)$$

$$Ar(^3P_2) + H_2 \rightarrow Ar + H + H \qquad k = 3.97 \times 10^{13}\ cm^3 \cdot mol^{-1} \cdot s^{-1} \qquad (R10)$$

Similarly, the following reactions contribute to H_2S conversion for H_2S in He:[10,31,39]

$$e + He \rightarrow He(2^3S_1) + e \qquad (R11)$$

$$He(2^3S_1) + H_2S \rightarrow He + H + HS \qquad (R12)$$

$$He(2^3S_1) + H_2 \rightarrow He + H + H \qquad (R13)$$

There are no reports of measured or calculated rate constants for reactions R12 and R13.

For H_2S in N_2, the major products of electron collision reactions with N_2 are N radicals and $N_2(A)$, the first electronic excited state of N_2.[40]

$$e + N_2 \rightarrow N + N + e \qquad (R14)$$

$$e + N_2 \rightarrow N_2(A) + e \qquad (R15)$$

Previous investigation[41] has shown that the rate of electron collision reaction R15 is about 7 times higher than that of R14. These active species react with N_2, H_2S, and H_2 as follows:[2,22,23]

$$N + H_2 \rightarrow NH_2 \qquad k = 1.14 \times 10^4\ cm^3 \cdot mol^{-1} \cdot s^{-1} \qquad (R16)$$

$$N + N \rightarrow N_2 \qquad k = 8.54 \times 10^{10}\ cm^3 \cdot mol^{-1} \cdot s^{-1} \qquad (R17)$$

$$N_2(A) + H_2 \rightarrow N_2 + 2H \qquad k = 2.11 \times 10^9\ cm^3 \cdot mol^{-1} \cdot s^{-1} \qquad (R18)$$

$$N_2(A) + H_2S \rightarrow N_2 + H + HS \qquad k = 1.81 \times 10^{14}\ cm^3 \cdot mol^{-1} \cdot s^{-1} \qquad (R19)$$

There are no reports of reaction of H_2S and N. However, by analogy with the extremely low rate constant for the reaction of N with H_2O (4×10^3 $cm^3 \cdot mol^{-1} \cdot s^{-1}$ at 1073 K),[13] we presume that N does not contribute significantly to H_2S conversion and that N radicals predominantly recombine to N_2 because rate constant for this recombination reaction (R17) is about 8×10^6 higher than

that of R16. In addition, no nitrogen containing byproducts, such as ammonia, were detected, which confirms that the only products of H_2S conversion in N_2 are H_2 and S.

For H_2S in H_2, the major product of electron collision with H_2 is atomic H because the dissociation energy of H_2 (4.4 eV) is far less than the excitation energy of the first excited state of H_2 (11 eV),[30] which results in all excited states of H_2 preferentially dissociating to H radicals:

$$e + H_2 \rightarrow H + H + e \qquad \text{(R20)}$$

Atomic H further contributes to H_2S conversion and formation in an autocatalytic manner through the following sequence of reactions:[26,29,32]

$$H + H_2S \rightarrow H_2 + HS \qquad k = 4.46 \times 10^{11}\ cm^3 \cdot mol^{-1} \cdot s^{-1} \qquad \text{(R21)}$$

$$HS + HS \rightarrow H_2S + S \qquad k = 2.41 \times 10^{13}\ cm^3 \cdot mol^{-1} \cdot s^{-1} \qquad \text{(R22)}$$

$$S + HS \rightarrow S_2 + H \qquad k = 2.41 \times 10^{13}\ cm^3 \cdot mol^{-1} \cdot s^{-1} \qquad \text{(R23)}$$

At low H_2S concentrations, most electrons collide with the balance gas, which suggests that pathway (IV) through reactions R6 and R7 is the major pathway for H_2S conversion. R8 and R9 are responsible for initiating H_2S conversion in Ar, R11 and R12 are responsible for initiating H_2S conversion in He, R15 and R19 are responsible for initiating H_2S conversion in N_2, and R20 and R21 are responsible for initiating H_2S conversion in H_2. With increasing H_2S concentration, the H_2S conversion rate by reaction R5 increases. Moreover, the increasing rate of H_2S conversion through R5 is expected to be larger than the decreasing rate of M* formation through R6 (which further contributes to H_2S dissociation through R7) with increasing H_2S concentration because the dissociation energy of H_2S (3.4 eV) is far less than the excitation energy of Ar (11.55 eV for $Ar(^3P_2)$), He (19.82 eV for $He(2^3S_1)$), or N_2 (6.1 eV for $N_2(A)$), and the dissociation energy of H_2 (4.4 eV). This explains the initial increase in H_2S conversion rate with

increasing H_2S concentration, as shown in Figure 2.6. However, H_2S is electronegative.[12] The presence of an electronegative gas as a reactant reduces the discharge current in the reactor by capturing electrons. Thus, the electron concentration during discharge is reduced due to the high electron affinity of H_2S, which results in a deceasing rate of electron collision reactions, as observed previously.[42,43] With increasing H_2S concentration, the electronegative effect of H_2S becomes more prominent and finally results in decreasing rates of electron collision reactions (R5 and R6). These effects explain the maximum and subsequent decrease of H_2S conversion rates with increasing H_2S concentration shown in Figure 2.6.

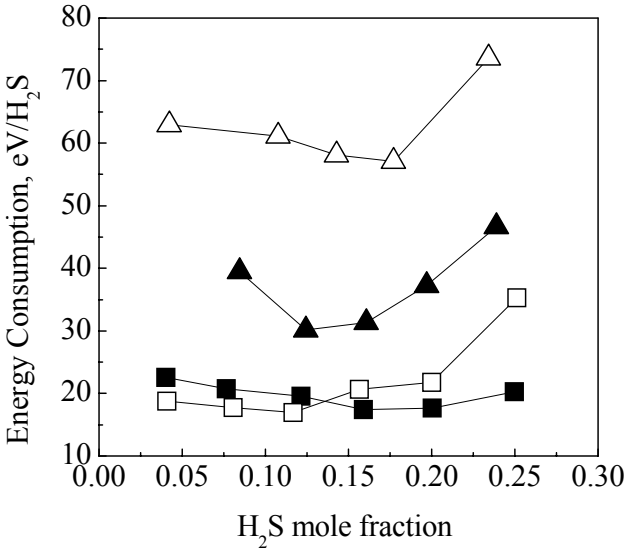

Figure 2.7. Energy consumption of H_2S conversion as a function of H_2S mole fraction in different balance gases. (■): H_2S in Ar, (□): H_2S in He, (▲): H_2S in N_2, (△): H_2S in H_2

Figure 2.7 shows energy consumption during H_2S conversion as a function of H_2S mole fraction in the four balance gases. The energy consumption of H_2S conversion initially decreases, reaches a minimum, and increases with increasing H_2S mole fraction, which is consistent with the trend of H_2S conversion rate shown in Figure 2.6. Energy consumption during H_2S conversion in H_2 is higher than in N_2 because the cross sectional area of molecular

H_2 is 1.86 times smaller than that of N_2 (as shown by the respective effective molecular radius of 1.35 versus 1.84 Å),[17] which causes a lower rate of electron collision reactions with H_2 compared to N_2 and results in more energy dissipation in H_2 compared to N_2. Energy consumption during H_2S conversion in Ar and He are the lowest of the tested gases and similar in magnitude.

Energy consumption during H_2S conversion in monatomic balance gases is far lower than in diatomic balances gas, which can be explained through analysis of electron collision processes for H_2S in the monatomic and diatomic balance gases. When an energetic electron collides with an atomic molecule, the electron predominantly experiences elastic collision without energy loss if the electron energy is less than the excitation energy of target atom. The electron is then further accelerated in the electric field and hence gains more energy. If the electron collides with H_2S in the next collision, H_2S can be dissociated easily because the electron has already experienced two accelerations over approximately two mean free path lengths of the gas molecules. When an energetic electron collides with a diatomic molecule, the electron can lose energy through the many energy levels available to diatomic molecules, including excitation, rotation, vibration, and dissociation, depending on the electron energy. For example, an energetic electron would be deactivated by contributing its energy to rotation and vibration of the diatomic molecule if the electron energy is less than excitation energy or dissociation energy. This implies that electrons cannot gain energy as efficiently in a diatomic balance gas compared to monatomic gases. The electron energy in atomic gases can be used more efficiently because there are no paths for energy loss to rotation and vibration. Therefore, energy efficiency of H_2S conversion in atomic balance gases is expected to be higher than that in diatomic balance gases, as observed in Figure 2.7.

The results in Figure 2.7 show that the lowest energy consumption (highest efficiency) of H_2S conversion is 17 eV/H_2S. This value is lower than the energy consumption reported in all previous investigations[1,15,16,21,25,28,33,34] except in microwave discharges at sub-atmospheric pressures (~4.5 eV/H_2S).[14] This result confirms that pulsed corona discharges are more efficient than other types and that relatively low energy consumption can be obtained at high pressures and H_2S concentrations. However, most hydrogen produced industrially by steam reforming of methane and other light alkanes has an energy consumption of 3.92 eV/H_2,[14] which is a factor of 4 less than the best (lowest) experimental values for energy consumption during H_2S conversion found during this portion of the investigation. However, as shown in Section 3, by optimizing reactor conditions, energy consumptions as low as ~7 eV/H_2 produced have been achieved, which is only a factor of less than 2 higher from being economically competitive with steam methane reforming as a method of H_2 production. Still, further improvements in plasma efficiency must be achieved before plasma processes will compete with current hydrogen production methods.

2.4 Conclusions

Breakdown voltages of H_2S in four balance gases (Ar, He, N_2 and H_2) measured at different H_2S concentrations and pressures are proportional to the partial pressures of H_2S and the respective balance gas. H_2S conversion rates and energy efficiencies depend on the balance gas and H_2S inlet concentrations. With increasing H_2S concentrations, H_2S conversion rates initially increase, reach a maximum, and then decrease. H_2S conversion in atomic balance gases, such as Ar and He, is more efficient than that in diatomic balance gases, such as N_2 and H_2. These observations can be explained by reaction mechanisms that involve electron collision reactions either with H_2S that cause direct dissociation or with the balance gas to produce active species in electronic

exited states that then relax by dissociating H_2S. The results show that nonthermal plasmas are effective for dissociating H_2S into hydrogen and sulfur, but further increases in energy efficiency are necessary.

2.5 References

1. Abolentsev, V.A., Korobtsev, S.V., Medvedev, D.D., Potapkin, B.V., Rusanon, V.D., Fridman, A.A., Shiryaevskii, V.L., 1995. Pulsed "wet" discharge as an effective means of gas purification from H2S and organosulfur impurities. High Energy Chemistry 29, 353.
2. Aleksandrov, E.N., Basevich, V.Y., Vedeneev, V.I., 1994. The elementary act of the reaction of nitrogen atoms with hydrogen in a gas phase. Khimicheskaya Fizika 13, 90.
3. Asisov, R.I., Vakar, A.K., Gutsol, A.F., Givotov, V.K., Krasheninnikov, E.G., Krotov, M.F., Rusanov, V.D., Fridman, A.A., Sholin, G.V., 1985. Plasmachemical methods of energy carrier production. International Journal of Hydrogen Energy 10, 475.
4. Averin, V.G., Potapkin, V.B., Rusanon, V.D., Fridman, A.A., Shiryaevskii, V.L., 1996. Dissociation of hydrogen sulfide molecules in a pulsed electric discharge. High Energy Chemistry 30, 125.
5. Bagautdinov, A.Z., Jivotov, V.K., Eremenko, J.I., Kalachev, I.A., Kozbagarov, A.I., Konstantinov, E.I., Musinov, S.A., Overchuk, K.I., Rusanon, V.D., Zoller, V.A., 1998. Plasmachemical hydrogen production from natural gases containing hydrogen sulfide. Hydrogen Energy Progress XII, Proceedings of the World Hydrogen Energy Conference, 12th, Buenos Aires, Argentina, 1, 683.
6. Bagautdinov, A.Z., Jivotov, V.K., Eremenko, J.I., Kalachev, I.A., Musinov, S.A., Pampushka, A.M., Rusanon, V.D., Zoller, V.A., 1993a. Natural hydrogen sulfide (H_2S) – source of hydrogen (plasma chemical dissociation). Frontier Science Series 7, 123.
7. Bagautdinov, A.Z., Zhivotov, V.K., Kalachev, I.A., Musinov, S.A., Pampushka, A.M., Rusanov, V.D., Tsoller, V.A., 1993b. Investigations of the Radial Distributions of Gas Flows in a High Power Microwave Discharge. High Energy Chemistry 27, 305.
8. Bagautdinov, A.Z., Jivotov, V.K., Eremenko, J.I., Kalachev, I.A., Musinov, S.A., Potapkin, B.V., Pampushka, A.M., Rusanov, V.D., Strelkova, M.I., Fridman, A.A., Zoller, V.A., 1995. Plasma chemical production of hydrogen from H_2S-containing gases in MCW discharge. International Journal of Hydrogen Energy 20, 193.
9. Bagautdinov, A.Z., Zhivotov, V.K., Musinov, S.V., Pampushka, A.M., Rusanov, V.D., Zoller, V.A., Epp, P.Y., 1992. Physicochemical processes during the dissociation of a hydrogen sulfide-carbon dioxide mixture in a microwave discharge. Khimiya Vysokikh Energii 26, 69.
10. Bevsek, H.M., Dunlavy, D.C., Siska, P.E., 1995. Nascent vibrational populations in He*(2 ^{1,3}S)+H_2, HD, D_2 Penning ionization from electron spectroscopy in crossed supersonic molecular beams. Journal of Chemical Physics 102, 133.
11. Blair, D.T.A., 1978. Breakdown Voltage Characteristics. In Electrical Breakdown of gases, Meek, J.M., Craggs, J.D., Eds., John Wiley & Sons: New York, 1978, p533.

12. Christophorou, L.G., Rodrigo, H., Marode, E., Bastien, F., 1987. Isotopic dependences of the dielectric strength of gases - new observations, classification, and possible origins. Journal of Physics D: Applied Physics 20, 1031.
13. Cohen, N., Westberg, K.R., 1991. Chemical kinetic data sheets for high-temperature reactions. Part II. Journal of Physical and Chemical Reference Data 20, 1211.
14. Cox, B.G., Clarke, P.F., Pruden, B.B., 1998. Economics of thermal dissociation of H_2S to produce hydrogen. International Journal of Hydrogen Energy 23, 531.
15. Dalaine, V., Cormier, J.M., Lefaucheux, P., 1998a. A gliding discharge applied to H_2S destruction. Journal of Applied Physics 83, 2435.
16. Dalaine, V., Cormier, J.M., Pellerin, S., Lefaucheux, P., 1998b. H_2S destruction in 50 Hz and 25 kHz gliding arc reactors. Journal of Applied Physics 84, 1215.
17. Daubert, T.E., Danner, R.P., 1997. Physical and Thermodynamic Properties of Pure Chemicals, Data Compilation; Taylor & Francis, Washington, DC.
18. Eliasson, B., Kogelschatz, U., 1986. Electron Impact Dissociation in Oxygen. Journal of Physics B 19, 1241.
19. Eliasson, B., Kogelschatz, U., 1991. Modeling and Applications of Silent Discharge Plasmas. IEEE Transactions on Plasma Science 19, 309.
20. Gundel, L.A., Setser, D.W., Clyne, M.A.A., Coxon, J.A., Nip, W., 1976. Rate constants for specific product channels from $Ar(^3P_{2,0})$ reactions and spectrometer calibration in the vacuum ultraviolet. Journal of Chemical Physics 64, 4390.
21. Helfritch, D.J., 1993. Pulsed corona discharge for hydrogen sulfide decomposition. IEEE Transactions on Industry Applications 29, 882.
22. Herron, J.T., 1999. Evaluated Chemical Kinetics Data for Reactions of $N(^2D)$, $N(^2P)$, and $N_2(A^3\Sigma_u^+)$ in the Gas Phase. Journal of Physical and Chemical Reference Data 28, 1453.
23. Kossyi, I.A., Kostinsky, A.Y., Matveyev, A.A., Silakov, V.P., 1992. Kinetic Scheme of the Non-equilibrium Discharge in Nitrogen-Oxygen Mixtures. Plasma Sources Science & Technology 1, 207.
24. Lide, D.R., 2003. CRC Handbook of Chemistry and Physics; CRC Press: Boca Raton, Florida.
25. Ma, H., Chen, P., Ruan, R., 2001. H_2S and NH_3 removal by silent discharge plasma and ozone combo-system. Plasma Chemistry and Plasma Processing 21, 611.
26. Peng, J., Hu, X., Marshall, P., 1999. Experimental and ab Initio Investigations of the Kinetics of the Reaction of H Atoms with H_2S. Journal of Physical Chemistry A 103, 5307.
27. Prestage, J.D., Johnson, C.E., Hinds, E.A., Pichanick, F.M.J., 1985. Precise study of hyperfine structure in the 2^3P state of ^3He. Physical Review A 32, 2712.
28. Ruan, R.R., Han, W., Ning, A., Chen, P.L., Goodrich, P.R., Zhang, R., 1999. Treatment of odorous and hazardous gases using non-thermal plasma. Journal of Advanced Oxidation Technologies 4, 328.
29. Schofield, K., 1973. Evaluated chemical kinetic rate constants for various gas phase reactions. Journal of Physical and Chemical Reference Data 2, 25.
30. Sharp, T.E., 1971. Potential-Energy Curves for Molecular Hydrogen and Its Ions. Atomic Data 2, 119.
31. Someda, K., Kondow, T., Kuchitsu, K., 1988. n-Distributions of atomic hydrogen(n) produced from water, water-d2, and hydrogen sulfide in collision with metastable helium atoms. Journal of Physical Chemistry 92, 6541.

32. Stachnik, R.A., Molina, M.J., 1987. Kinetics of the reactions of mercapto radicals with NO_2 and O_2. Journal of Physical Chemistry 91, 4603.
33. Traus, I., Suhr, H., 1992. Hydrogen sulfide dissociation in ozonizer discharges and operation of ozonizers at elevated temperatures. Plasma Chemistry and Plasma Processing 12, 275.
34. Traus, I., Suhr, H., Harry, J.E., Evans, D.R., 1993. Application of a rotating high-pressure glow discharge for the dissociation of hydrogen sulfide. Plasma Chemistry and Plasma Processing 13, 77.
35. van Veldhuizen, E.M., Rutgers, W.R., Bityurin, V.A., 1996. Energy efficiency of NO removal by pulsed corona discharges. Plasma Chemistry and Plasma Processing 16, 227.
36. Velazco, J.E., Kolts, J.H., Setser, D.W., 1978. Rate constants and quenching mechanisms for the metastable states of argon, krypton, and xenon. Journal of Chemical Physics 69, 4357.
37. Watson, J.T., 1997. Introduction to Mass Spectrometry, 3rd ed.; Lippincott-Raven, Philadelphia.
38. Wiseman, N., Douglas, W.J.M., 1972. Oxidation of hydrogen sulfide in a corona discharge. AIChE Symposium Series 68, 297.
39. Yencha, A.J., Wu, K.T., 1978. Energy transfer processes in reactions of $He(2^3S)$ with triatomic molecules. II. H_2O and H_2S. Chemical Physics 32, 247.
40. Zhao, G.-B., Hu, X., Argyle, M.D., Radosz, M., 2004. N Atom Radicals and $N_2(A^3\Sigma_u^+)$ Found to be Responsible for Nitrogen Oxides Conversion in Nonthermal Nitrogen Plasma. Industrial & Engineering Chemistry Research 43, 5077.
41. Zhao, G.-B., Garikipati, S.V.B.J., Hu, X., Argyle, M.D., Radosz, M., 2005. The Effect of Gas Pressure on NO Conversion Energy Efficiency in Nonthermal Nitrogen Plasma. Chemical Engineering Science 60, 1927.
42. Zhao, G.-B., Garikipati, S.V.B.J., Hu, X., Argyle, M.D., Radosz, M., 2005. Effect of Oxygen on Nonthermal-Plasma Reactions of Nitrogen Oxides in Nitrogen. AIChE J 51, 1800.
43. Zhao, G.-B., Hu, X., Argyle, M. D., Radosz, M., 2005. Effect of CO_2 on Nonthermal-Plasma Reactions of Nitrogen Oxides in N_2. Part II: Percent-level Concentrations. Industrial & Engineering Chemistry Research 44, 3935.
44. Zhao, G.-B., Argyle, M.D., Radosz, M., 2007. Optical Emission Study of Nonthermal Plasma Confirms Reaction Mechanisms Involving Neutral Rather than Charged Species. Journal of Applied Physics, 101(3), 033303(14).
45. Zhao, G.-B., John, S., Zhang, J.-J., Wang, L., Mukhnahallipatna, S., Hamann, J., Ackerman, J., Argyle, M.D., Plumb, O.A., 2006. Methane Conversion in Pulsed Corona Discharge Reactors. Chemical Engineering Journal 125, 67.
46. Zhao, G.-B., Argyle, M.D., Radosz, M., 2006. Effect of CO on Conversion of NO and N_2O in Nonthermal Argon Plasma. Journal of Applied Physics 99(11), 113302(14).

Section 3
Energy Efficiency of Pulsed Corona Decomposition of Hydrogen Sulfide

3.1 Introduction

Building on the results of Section 2, the reactor operating parameters that provided the highest energy efficiency for H_2S conversion were explored. At high H_2S concentrations (>16%), H_2S decomposition in Ar was found to give higher conversions and reaction rates, compared to that in He, N_2 and Ar. Therefore, Ar was selected as the balance gas for the majority of the experiments reported in this section. The electrical parameters of charge voltage (V), pulse-frequency (f), and pulse-forming capacitance (C) have been reported to have the largest influence on conversion in plasma reactors. For methane conversion,[1] the moles of methane converted per unit of energy supplied decreased with increasing charge voltage and increased with increasing pulse-frequency. For ppm-concentration H_2S destruction in an ozonizer,[2] H_2S conversion increased with charge voltage. Removal of ppm-concentrations of NO from nitrogen streams[3] increased with the pulse frequency and the capacitance ratio. In all of these studies, the total power supplied to the reactor changed as each of these parameters was varied because power supplied to the reactor (P) depends on all of them: $P = 0.5CV^2f$. This variation in power input makes it difficult to distinguish the effect of variation of each of these parameters from the overall change in power input. Therefore, we designed a series of experiments to determine the effect on H_2S conversion and energy efficiency, defined as energy consumed per molecule of H_2S converted, of varying each of these parameters at constant power input.

3.2 Experimental

The experimental system is similar to the one described in Figure 2.1, except for a modified cathode, new pulse-forming capacitors, and absence of the sulfur trap. The cathode was a stainless steel tube 0.024 m in diameter and 0.889 m long, with 7 quartz view ports and 6 ports for sampling and temperature measurement placed equidistantly along its length. The quartz view-ports had 0.01 m diameter circular viewing areas for visual inspection of the corona discharge. The sampling ports were initially connected to the mass spectrometer (MS) by stainless steel capillary tubing (0.00159 m outside diameter (OD) × 0.000572 m inside diameter (ID)) via a 7-way valve to measure gas concentration changes along the length of the tube. Steady-state data were difficult to obtain from these sample ports, so the gas was sampled from the outlet of the reactor. To perform quantitative measurements using the MS, an internal standard method[4] was used to calibrate the ion signal response at an m/z ratio of 34 for the H_2S mole fraction and the argon (Ar) was used as an internal standard. The stems of bimetallic thermometers were immersed about 0.025 m into tees connected to the cathode tube. The thermometers proved to be unresponsive and displayed near ambient temperatures even when the tube was hot to touch (although reactor temperatures probably did not exceed 350 K). Similar conversion of H_2S was obtained in geometrically similar cathode tubes with and without ports at similar values electrical parameters, indicating a negligible effect of the cathode viewports on the corona discharge. A sulfur trap was connected to the outlet of the reactor in the earlier setup to avoid blockage of the tubing by condensing sulfur. The 0.0064 m OD × 0.00386 m ID outlet tubing from the reactor was replaced with 0.00953 m OD × 0.00704 m ID tubing, which eliminated the need for the sulfur trap.

The pulse-forming capacitance could be increased in increments of 720 pF by added individual capacitors (TDK FHV-10AN). The reactor was oriented vertically, with the gas flow from top to bottom. The electrical system could deliver charge voltages from 6.9 kV to 30 kV at pulse frequencies from 0 to 1000 Hz. The anode was a stainless steel wire 0.001 m in diameter passing axially through the center of the tube. The gas flowing through the reactor tube was converted to a pulsed corona plasma by high voltage discharge from the reactor anode. The H_2S in Ar gas mixture was prepared by mixing ultra high purity (UHP) H_2S with the UHP Ar gas from calibrated mass flow controllers (Brooks MFC) to achieve the desired entering mole fractions. Gas mixtures flowed through PCDR at entrance conditions of ambient temperature (~300K) and a controlled pressure. The energy released by the capacitors per pulse was calculated from $\frac{1}{2}CV_c^2$, where C is the pulse forming capacitance, and V_c is the constant charge voltage before discharge. The power consumed, W ($J \cdot s^{-1}$), was calculated as the product of the input energy per pulse and the pulse frequency, $\frac{1}{2}fCV_c^2$, where f is the pulse frequency in Hz.

3.3 Results and discussion

Figure 3.1. Corona discharge as seen through a view port

3.3.1 Visual observations through the view ports on the corona reactor. The corona discharge around the wire could be easily seen through the view ports. The location of the brightest discharge depended on the type of gas, its concentration (in the case of mixtures), and charge voltage. In pure Ar, the brightest discharge occurred in the upper 0.3-0.6 m of the reactor, but it moved down to the lower 0.3-0.6 m section in pure nitrogen (N_2). The probable explanation for this effect is that Ar is a monatomic gas, while N_2 is a diatomic gas. As the gases travel through the cathode tube from top to bottom, the electrons are energized by the pulsed electric field between the wire and the tube. In a monatomic gas like Ar, an electron predominantly experiences elastic collisions with Ar atom without energy loss because the electron energy is less than the excitation energy of the target atom. The electron is then further accelerated and gains more energy in the electric field. If its energy becomes greater than the excitation energy (11.6 eV) of the lowest electronically excited state of Ar, Ar ($^3P_2$), it will experience an inelastic collision by transferring energy to excite the Ar atom and lose some kinetic energy. However, when an energetic electron collides with a diatomic molecule like N_2, the electron can lose energy through many processes, including dissociation to form two N radical, excitation (7.2 eV), or rotational or vibrational (1.7-3.5 eV) excitation of N_2, depending on electron energy. This implies that electron energy cannot be accumulated as efficiently in diatomic background gases. Therefore, the brightest discharge in N_2 occurs further down the length of the reactor compared to Ar because more energy input is required to form the required excited species to create the plasma. This explanation also explains the downward shift of the brightest discharge in Ar with increasing concentrations of a diatomic gas like H_2S. In H_2S-Ar mixtures, as the charge voltage is increased from 11 kV to 21 kV, the brightest streamers move from the lower portion of the tube to the upper portion. The increase in voltage causes an

increase in the electric field around the wire, which imparts more energy to the electrons, causing the corona discharge to occur earlier in the reactor.

The total volume of the reactor in which the corona discharge existed also varied with charge voltage. The discharge could be simultaneously seen in 2, 3 or sometimes 4 view ports at lower voltages (11 kV, 13 kV & 15 kV), while at higher voltages (17 kV, 19 kV & 21 kV), it was observed in only 1 or 2 view ports. This indicates that the plasma volume in the reactor increases with decreasing voltage and increasing frequency. Thus, the reactor volume is used more efficiently at those conditions, as indicated by increased conversion, discussed below.

3.3.2 H_2S conversion in Ar generally increases with decreasing charge voltage and increasing frequency at constant pulse capacitance (and power). Similar to the general results obtained for methane conversion (reported in Section 1), at any particular value of capacitance, the H_2S conversion generally decreased with decreasing pulse frequency and increasing charge voltage, at a constant power of 100 W. High pulse frequency and low charge voltage conditions were the best for H_2S conversion at high concentrations that would be found in many industrially relevant processes. This conclusion is supported by the results from several mixtures of H_2S and Ar (4%, 8% and 12%), as shown in Figure 3.2, which present H_2S conversion as a function of charge voltage for four capacitances. At lower concentrations, the trend of decreasing conversion with increasing charge voltage did not hold for three of the capacitances. Instead, conversion increased with increasing charge voltage for the three lowest capacitance values in 4% H_2S (shown in Figure 3.2(a)). These results suggest that there is a broad maximum in conversion as H_2S concentration increases, followed by the general trend of decreasing conversion with increasing charge voltage observed at higher H_2S concentrations (8% and 12% H_2S in Figures 3.2(b) and 3.2(c), respectively). Lower values of capacitance

(correlated with higher pulse frequencies) appear to always produce higher conversions (and thus higher energy efficiencies) under all tested conditions. Since high concentrations of H_2S (greater than ~6%, where this maxima appears to occur) are often more important in industrial applications, our study indicates that lower charge voltages will also maximize conversion and energy efficiency. However, for low concentrations (below ~6% H_2S), there appears to be an optimum charge voltage that will maximize conversion (and minimize energy consumption, see Section 3.3.3).

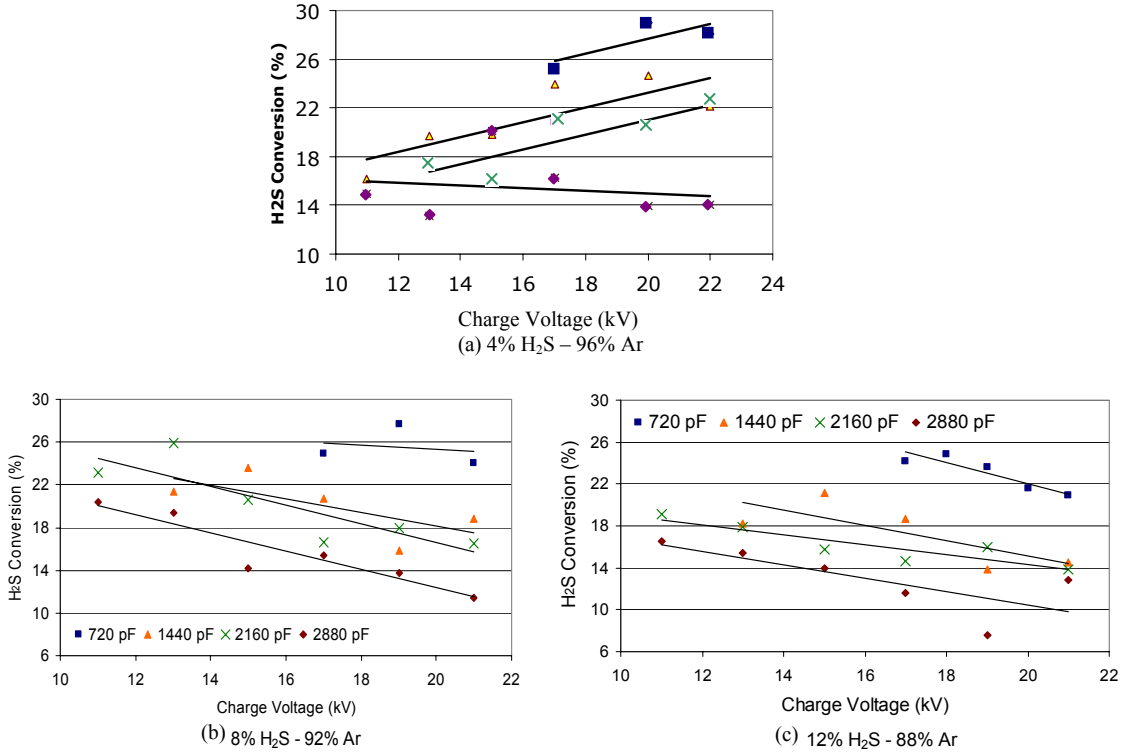

Figure 3.2. Conversion of H_2S as a function of charge voltage and capacitance. (a) 4% H_2S and 96% Ar; (b) 8% H_2S and 92% Ar; (c) 12% H_2S and 88% Ar. Data: 720 pF (■), 1440 pF (▲), 2160 pF (×), 2880 pF (♦)

Based on the study of pulsed corona discharges in air and flue gas, a difference in the streamer characteristics with increasing charge voltage has been reported.[5] Streamers are thin, ionized, luminous channels formed between the electrodes. Two types of streamers have been

reported: primary and secondary. In our case of a positive pulsed corona discharge, the streamers are directed from the wire (anode) to the tube (cathode). Secondary streamers develop when the primary streamers approach the cathode.[5] With increasing charge voltage, the average streamer propagation velocity increases with a concomitant decrease in the duration for primary streamer propagation.[5] The increase in streamer velocity with increase in voltage is corroborated by the discharge voltage waveform for methane.[6] As the primary streamers die out faster with increasing voltages, the secondary streamers start to develop at higher voltages. Thus, at higher charge voltages, both primary and secondary streamers are formed, while at lower charge voltages, only primary streamers are formed. This behavior is seen in both wire-plate and wire-cylinder reactors, irrespective of power system specifications.[5]

In air, the average electron energy for primary streamer heads is about 10 eV and for secondary streamer is around 1 eV.[5] Therefore, low charge voltage conditions produce more electrons with an average energy of 10 eV, which is closer to the excitation energy (11.55 eV) for the lowest excited state of Ar ($Ar(^3P_2)$) and higher than the electron energy range (8-9 eV)[7] in which the maxima in the absolute total electron-scattering cross section for H_2S occurs. These energies are more than sufficient to dissociate H_2S into HS and H because the H-SH bond strength at 298 K is 3.96 eV.[8] As discussed in Section 2, the excitation of Ar and the direct dissociation of H_2S by electron collision are proposed as the initiating steps of the two pathways responsible for H_2S decomposition in Ar.[9] One of the products of H_2S dissociation is HS, which has an electron affinity of 2.3 eV.[8] A high value of electron affinity indicates easy formation of HS^- ions:

$$HS + e \rightarrow HS^- \quad \Delta H° = 2.3 \text{ eV}$$

At electron energies ranging from 1.5 eV to 3.5 eV, HS^- formation has been reported with a strong resonance at 2.28 eV and a cross section equal to 180 x 10^{-20} cm^2.[10]

$$H_2S + e \rightarrow H + HS^-$$

Therefore, HS^- formation rates would increase at the low electron energies found in secondary streamers.

Such electron attachment processes are considered essential in weekly ionized plasmas, like corona discharges, with low electron concentration and low degree of ionization. These processes are first order with respect to electron concentration. The HS^- ion could be involved in ion cluster formation with H_2S:[11]

$$HS^- + H_2S \rightarrow (HS^- \bullet H_2S) \quad \Delta H° = 0.572 \text{ eV/molecule}$$

Energy utilization efficiency[12] is defined to be the ratio of the primary streamer energy to the total pulse discharge energy, where pulse discharge energy is calculated by integrating the discharge power waveform from an oscilloscope over the pulse duration. Two peaks have been reported in the voltage, current, and power waveforms, where the first and the second peaks represent the primary streamer and the secondary streamers, respectively. Therefore, the primary streamer energy can be calculated by integrating the first power peak. For SO_2 decomposition, the energy utilization efficiency decreased with increasing voltage.[13] Similarly, in our conditions at higher voltages, an increasing amount of energy could appears to be used for inefficient secondary streamer formation.

An earlier study[14] of positive streamers in ozone in a pulsed corona discharge system showed that as the applied voltage increases, the thickness, intensity, and velocity of the primary streamers increase. The number of streamers leaving the anode also increases, but the number reaching the cathode was independent of voltage. This implies that the total plasma volume

increases. In the same study, the pulse frequency up to 400 Hz was found to have no effect on the diameter, intensity and number of streamers. The increased plasma volume at higher voltages could cause increased conversion.

However, our data indicates that the increase in conversion due to larger plasma volume is offset by a decrease in conversion due to formation of energy-inefficient secondary streamers. Thus, although the power supplied to the pulsed corona reactor is the same, low voltage and high frequency conditions are desirable to increase H_2S decomposition rates and efficiencies.

3.3.3 Energy consumption for H_2S conversion in Ar decreases with decreasing pulse-forming capacitance at constant power input. Energy consumption per H_2S molecule decreases with decreasing pulse-forming capacitance at constant power, as shown in Figure 3.3. The lowest pulse forming capacitance (720 pF) yields the least energy consumption per H_2S molecule converted, which is also the highest energy efficiency per input power. This result is similar to the trend first identified during the methane experiments, as discussed with Figure 1.6(a) in Section 1. As in Figure 3.2(a), the 4% H_2S data shown in Figure 3.3(a) have opposing slopes for the three lowest values of capacitance. As explained previously, there are apparently minima in these data as a function of H_2S concentration. Below ~6% H_2S at the lower values of capacitance, energy consumption per converted H_2S molecule has passed the minimum and is increasing as charge voltage decreases. The energy consumptions per converted H_2S molecule are significantly higher for the 4% H_2S experiment (up to ~40 eV/H_2S, as shown in Figure 3.3(a)) compared to the other concentrations. All experiments were all conducted at constant power input of 100 W and constant total flow rate. As there was less H_2S flowing through the reactor at this low concentration, the energy consumption is quite high (and the energy efficiency is low). Conversely, for the 12% H_2S data shown in Figure 3.3(c), the energy consumptions are

½ to ¼ lower (and energy efficiency is proportionally higher) than the 4% H_2S data. Again, this result is in agreement with the methane data from Section 1 where energy efficiency increased (and energy consumption decreased) at higher flow rates (see Figure 1.8). In the H_2S case, the higher molar flow rates were associated with higher H_2S concentrations at a constant flow rate, but this still produced higher energy efficiencies (corresponding to lower energy consumptions).

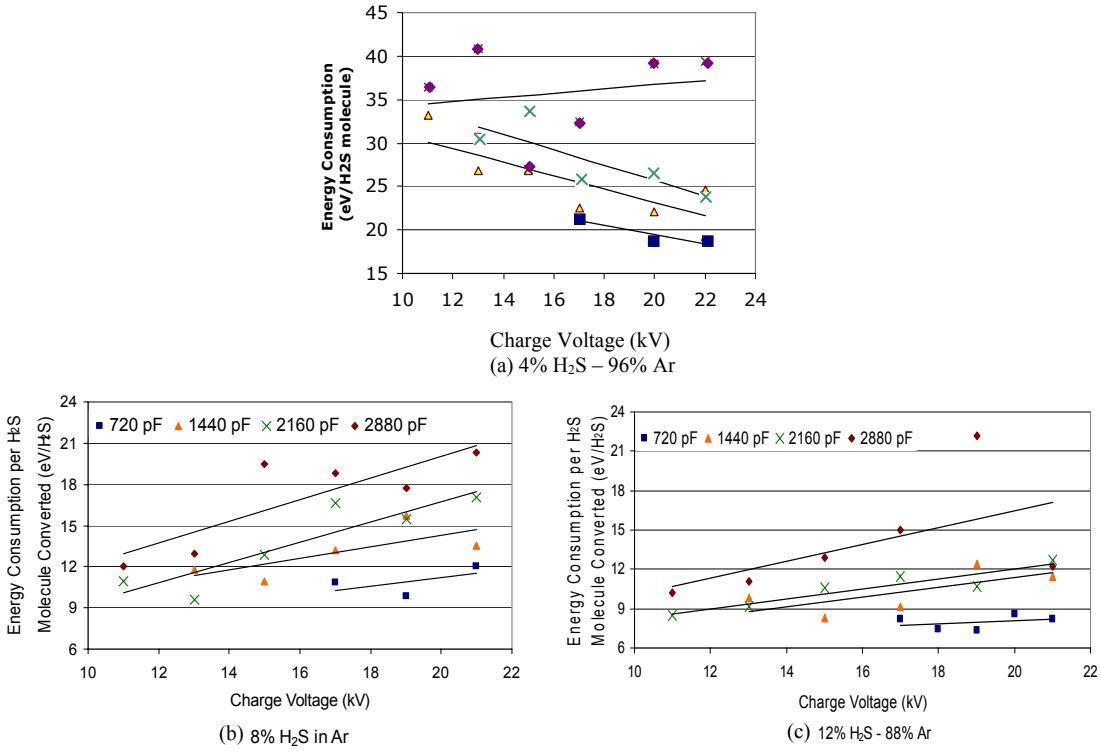

Figure 3.3. Energy consumption per H_2S molecule converted as a function of charge voltage and capacitance. (a) 4% H_2S and 96%, (b) 8% H_2S and 92% Ar, and (c) 12% H_2S and 88% Ar. 720 pF (■), 1440 pF (▲), 2160 pF (×), 2880 pF (♦)

This phenomenon can be explained by the optimum energy transfer condition proposed by Uhm *et al.*[15] and Mok.[3] In their analytical investigation of corona discharge systems[15], Uhm *et al.* obtained the optimum energy transfer condition as,

$$2\frac{C_e}{C_{R0}} = 1 + 2\frac{\ln(R_0/R_c)}{\ln(1.11\zeta)}$$

where C_e is the capacitance of the external circuit, C_{R0} is the initial capacitance of the reactor chamber, R_0 is the radius of the wire, R_c is the radius of the tube, and ζ is the normalized plasma mobility related to the ionization front velocity.

In Mok's experimental study of ppm-concentration NO decomposition in a wire-plate reactor,[3] C_{R0} was calculated by measuring the discharge voltage and current, when the charge voltage is lower than the corona onset value, as follows:

$$I_{cap} = C_{RO} \frac{dV}{dt}$$

where, I_{cap} is the capacitive current measured and dV/dt is the rate of change in discharge voltage. The charge voltage applied was lower than the corona onset value, so the measured current was only capacitive and did not include corona current. Mok found that the reactor capacitance increased and reached a value of three times the initial reactor capacitance during the corona discharge. Further, he found that the energy transferred from the pulse-forming capacitance to the reactor reached a maximum when the pulse-forming capacitance was three times the initial capacitance of the reactor. This was verified both by electrical measurements and by the NO decomposition experiment, by increasing pulse-forming capacitance. Therefore, Mok proposed the optimum energy transfer condition as,

$$\frac{\text{Pulse - forming capacitance } (C_P)}{\text{Initial capacitance of reactor } (C_{R0})} \approx 3$$

The initial capacitance the reactor (C_{R0}) can also be calculated using a capacitance formula for the wire-in-tube geometry as follows[16]:

$$C_{R0} = \frac{2\pi k \varepsilon_0 L}{\ln(R/r)} \approx 16.7\ pF$$

where, R is the cathode tube radius (0.012 m for our reactor), r is the anode wire diameter (0.00057 m), L is the reactor length (0.914 m), ε_0 is the permittivity of free space (8.854 x 10^{-12} F/m), and k is the dielectric constant of the mixture of H_2S and Ar (on order of 1 for the H_2S-Ar mixtures used in our experiments).

For our case of relatively high concentrations of H_2S in Ar at constant power, results similar to the ppm-concentration NO decomposition are obtained.[3] However, as the capacitance is increased in our study, the power remains constant by decreasing charge voltage and frequency, which was not done in Mok's work. Thus at 720 pF, a higher fraction of the energy supplied is transferred into the reactor, resulting in higher H_2S conversions and hence lower energy consumptions. Table 3.1 shows representative data for two different H_2S concentrations. As the capacitance ratio approaches the optimum energy transfer ratio, the energy consumption decreases.

Table 3.1. Effect of pulse-forming capacitance on energy consumption

Pulse-forming capacitance (C_P, pF)	720	1440	2160	2880
Capacitance ratio (C_P/C_{R0})	45	90	135	180
Energy consumption in 8% H_2S-92% Ar mixture at 17 kV (E, eV/H_2S molecule)	10.8	13.2	16.6	18.8
Energy consumption in 12% H_2S-88% Ar mixture at 17 kV (E, eV/H_2S molecule)	8.2	9.2	11.4	15.0

3.3.4 H_2S conversion in N_2-Ar mixtures as the balance gas. The experiments reported in Section 2 showed that H_2S conversion is higher in monatomic gases (Ar and He) than in diatomic gases (N_2 and H_2). At high H_2S concentrations (>16%), H_2S conversion in Ar was the highest of the four balance gases. Since Ar is more expensive than N_2, the process could be cheaper if Ar is diluted with N_2, although the Ar would be recycled with minimal losses. Further, a larger volume of the reactor might be occupied by the corona because Ar tends to form

a corona earlier in the reactor compared to N2, as discussed earlier in this section. H_2S decomposition was performed in several concentrations of Ar and N_2. The power, charge voltage, pulse-frequency, reactor pressure and total flow rate were kept constant at 80 W, 15 kV, 720 pF, 988 Hz, 8 psig, and 15 SCFH respectively. The MS was calibrated for H_2S concentrations ranging from 4% to 10% in 23% N_2 (balance Ar), 46% N_2 (balance Ar) and 69% N_2 (balance Ar). For the experimental data reported in Figure 3.4, H_2S concentration was kept constant at 8%, while N_2 concentrations were varied between 0% (92% Ar), 23% (69% Ar), 46% (46% Ar), and 69% (23% Ar). The H_2S conversion for the four mixtures is shown in the Figure 3.4. The H_2S conversion initially increases with increasing addition of N_2, peaks for the 46% N_2-46% Ar mixture, and then decreases. Based on our earlier experiments, the H_2S conversion with N_2 as the balance gas would be lower than with Ar as the balance gas. These preliminary results indicate dual benefits of using Ar-N_2 mixtures as balance gas: increasing conversion, probably due to more evenly distributed corona discharge in the reactor and potential cost reduction for using a cheaper gas.

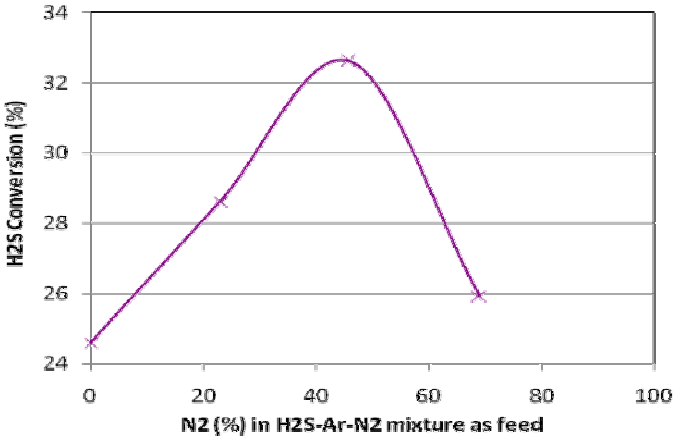

Figure 3.4. H_2S conversion in Ar-N_2 mixture as balance gas

3.3.5 Effect of flow rate on conversion. Figure 3.5 shows H_2S conversion and reaction rate for several flow rates of 16% H_2S in Ar. Overall conversion decreases with increasing flow rate, as expected because the residence time within the reactor is decreased and the specific energy density is reduced as more gas flows through the reactor. The reaction rate actually increases with increasing flow rate, but the increase does not keep pace with the increase in molar flow rate through the reactor, resulting in the decrease in overall conversion. However, the increasing reaction rate results in improved energy efficiency (or a decrease in energy consumption per H_2S molecule converted, as shown in Figure 3.6). The energy consumption decreases from nearly 40 eV/H_2S molecule to just less than 20 eV/H_2S. Similar data have been previously collected for lower H_2S concentrations (which have shown even higher energy efficiency), but these new data will help us more completely quantify the reaction kinetics and reactor performance.

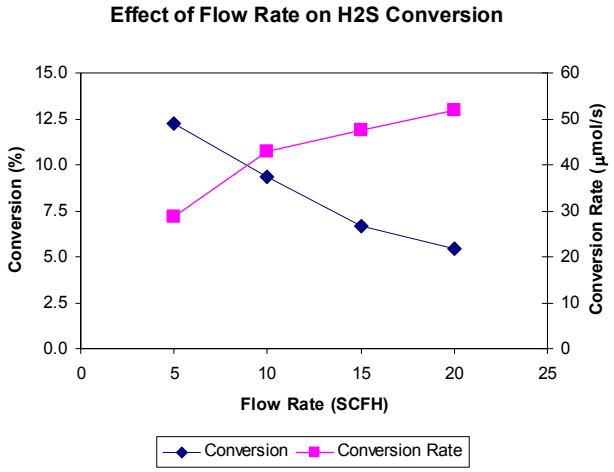

Figure 3.5. Overall H_2S conversion and H_2S conversion rate as a function of inlet flow rate. (16% H_2S balance Ar, 8 psig, 100 W power input, 1440 pF capacitance, 15 kV discharge voltage, 618 Hz pulse frequency).

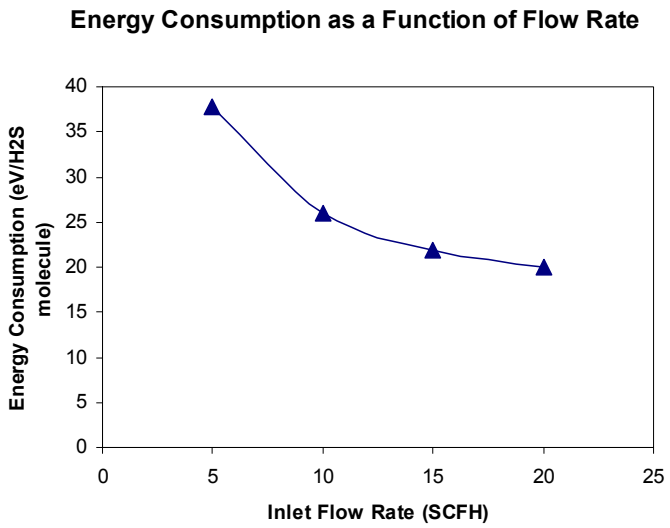

Figure 3.6. Energy consumption per H_2S molecule as a function of inlet flow rate (16% H_2S balance Ar, 8 psig, 100 W power input, 1440 pF capacitance, 15 kV discharge voltage, 618 Hz pulse frequency).

3.3.6 Effect of trigger waveform on H_2S conversion. The trigger signal generated by the synthesized function generator (SRS DS335) is adjustable in waveform and frequency. At constant charge voltage (15 kV), frequency (620 Hz) and capacitance (1440 pF), the effect on H_2S conversion of four waveforms (sinusoid, square, sinusoid triangle, and ramp) was investigated. The feed gas was a mixture of H_2S (8 mol%) in Ar. The sinusoid waveform produced the highest H_2S conversion (as shown in Figure 3.7 and Table 3.2), while the ramp waveform produced the lowest value, as reported earlier for dimethyl ether conversion.[17]

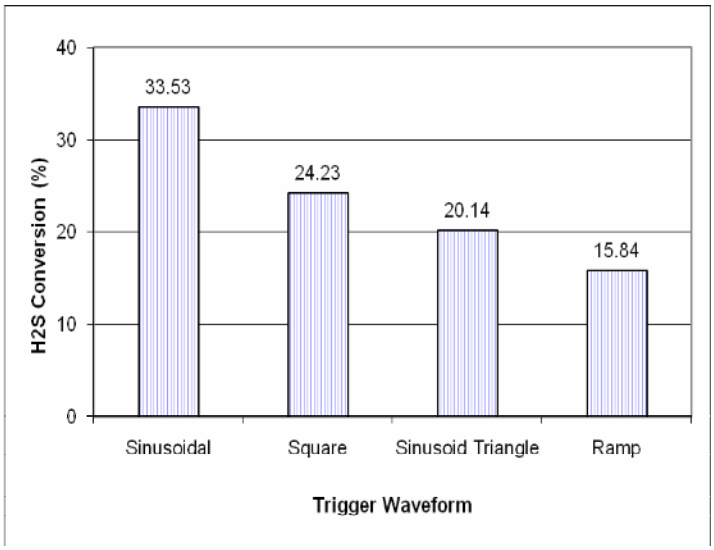

Figure 3.7. Effect of trigger waveform on H_2S conversion

Table 3.2. Trigger Waveform characteristics and H_2S conversion

No.	Wave	Amplitude (V_{RMS})	Offset (V_{pp})	Conversion (%)
1	Sinusoidal	3.5	1.6	33.53
2	Square	3.5	1.6	24.23
3	Sinusoid Triangle	3.5	1.6	20.14
4	Ramp	3.5	1.6	15.84
5	Noise	-	-	-

3.3.7 Effect of flow direction. Experiments exploring effect of flow direction on conversion led us to conclude that downward flow of gas gives slightly higher conversion. The results are as shown in Table 3.3:

Table 3.3. Effect of flow direction on H_2S conversion

Flow Direction	H_2S conc.(%)	Conversion (%)
↑	24.98	4.66
↑	23.43	6.31
↓	21.69	8.35
↓	21.69	6.67
↓	22.74	7.67
↓	22.93	8.80

All experiments had following conditions: reactants: 25% H_2S in Ar, total flow rate: 15 SCFH, charge voltage: 17 kV, reactor pressure: 8 psig, capacitance: 2160 pF, and pulse frequency: 360 Hz.

3.4 Conclusions

The various parameters studied in this section, including charge voltage, capacitance, and pulse frequency at constant reactor power input, mixtures of balance gases, reactant flow rate and direction, and pulse waveform all show optimization potential for future reactor operation. The most important conclusion is that low capacitance, low charge voltage, high pulse frequency operation produces the highest energy efficiency for H_2S conversion. While monatomic gases, such as argon, appear to be the best diluents, mixtures of argon and nitrogen may produce even higher H_2S conversions and energy efficiencies.

There is a trade-off between reactor flow rate and energy efficiency. Although higher energy efficiencies are obtained at higher flow rates, lower conversions are also achieved, resulting in the need for larger reactors and higher recycle rates. There will be an economic optimum between lower operating costs resulting from the higher energy efficiency operation and the higher capital cost resulting from higher flow rates. Pulse waveform can have a significant effect on energy efficiency. All experiments conducted in this study, except for the ones evaluating the effect of pulse waveform, were performed with square pulses. As significantly higher energy efficiencies were achieved with the sinusoidal waveform, this type of pulse trigger waveform should be used. Finally, flow direction relative to the direction of gravity does not appear to be an important parameter.

3.5 References

1. Yao,S.; Nakayama,A.; Suzuki, E., 2001. Methane conversion using a high-frequency pulsed plasma: Important factors. AICHE Journal, 47, 413.
2. Haas, L. A.; Khalafalla, S. E., 1973. Decomposition of hydrogen sulfide in an electrical discharge. U.S. Bureau of Mines Report of Investigation 7780.
3. Mok, Y. S., 2000. Efficient Energy Delivery Condition from Pulse Generation Circuit to Corona Discharge Reactor. Plasma Chemistry and Plasma Processing, 20, 353.
4. Watson, J.T., 1997. Introduction to Mass Spectrometry, 3rd ed.; Lippincott-Raven, Philadelphia.
5. Yan, K.; Hui, H.; Cui, M.; Miao, J.; Wu, X.; Bao, C.; Li, R., 1998. Corona Induced Non-Thermal Plasmas: Fundamental Study and Industrial Applications. Journal of Electrostatics, 44, 17.
6. Yao, S.; Nakayama, A.; Suzuki, E., 2001. Methane conversion using a high-frequency pulsed plasma: Discharge features. AIChE Journal, 47, 419.
7. Szmytkowski, C.; Możejko, P.; Krzysztofowicz, A., 2003. Measurements of absolute total cross sections for electron scattering from triatomic polar molecules: SO_2 and H_2S. Radiation Physics and Chemistry, 68, 307.
8. Lide, D.R. CRC Handbook of Chemistry and Physics; CRC Press LLC: United States of America, 2003, p9-66.
9. Zhao, G.-B.; John, S.; Zhang, J.-J.; Hamann, J. C.; Muknahallipatna, S. S.; Legowski, S.; Ackerman, J. F.; Argyle, M. D., 2007. Chemical Engineering Science, 62, 2216.
10. Rao, M. V. V. S.; Srivastava, S. K., 1993. Electron impact ionization and attachment cross sections for H_2S. Journal of Geophysical Research**,** 98, 13137.
11. Meot-Ner (Mautner), M. M.; Lias, S. G., "Binding Energies Between Ions and Molecules, and The Thermochemistry of Cluster Ions" in NIST Chemistry WebBook, NIST Standard Reference Database Number 69, Eds. P.J. Linstrom and W.G. Mallard, June 2005, National Institute of Standards and Technology, Gaithersburg MD, 20899 (http://webbook.nist.gov).
12. Bingyan, D.; Jie, L.; Yan, W.; Guofeng, L., 2005. Experimental Study of Secondary Streamer Energy in Pulsed Corona Discharge. Japanese Journal of Applied Physics, 44, 1959.
13. Mok, Y. S.; Ham, S. W.; Nam, I. S., Evaluation of Energy Utilization Efficiencies for SO_2 and NO Removal by Pulsed Corona Discharge Process. *Plasma Chemistry and Plasma Processing* **1998,** 18, (4), 535-550.
14. Winands, G. J. J.; Liu, Z.; Pemen, A. J. M.; van Heesch, E. J. M.; Yan, K; van Veldhuizen, E. M., 2006. Temporal development and chemical efficiency of positive streamers in a large scale wire-plate reactor as a function of voltage waveform parameters. J. Phys. D: Appl. Phys., 39, 3010.
15. Uhm, H. S.; Lee, W. M., 1997. An analytical theory of corona discharge plasmas Physics of Plasmas, 4, 3117.
16. Shin, D. N.; Park, S. W.; Hahn, J. W., 2000. Detection of OH(A2∑+) and O(1D) Emission Spectrum Generated in a Pulsed Corona Plasma. Bulletin of the Korean Chemical Society**,** 21, 228.
17. Zou, J.-J.; Zhang, Y.-P.; Liu, C.-J., 2007. Hydrogen production from dimethyl ether using corona discharge plasma. J. Power Sources, 163, 653.

Section 4
Hydrogen Permeable Membranes

4.1 Introduction

Plasma is a source of radicals, ions, and excited atoms and molecules. CH_4 and H_2S decomposition in our plasma reactor forms H atoms because the average electron energy in corona discharges (10 eV) is greater than the dissociation energy for hydrogen molecule (4.4 eV) and the energy for direct electron collision dissociation of CH_4 (~8 eV) and H_2S (~4eV), during which H atoms are formed. Metal membranes have been reported to be superpermeable to H atoms. Experimentally,[1] there is a substantial increase in the permeation flux through a metallic membrane exposed to an incident flux of hydrogen atoms compared to a similar flux of hydrogen molecules. Pick and Sonnenberg[2] attributed the higher flux to two major causes:

- The sticking probability for atomic hydrogen is much higher than that for hydrogen molecules: unpaired d-electrons in transition metals are responsible for the strong chemisorption of hydrogen on such surfaces. However, the presence of electronegative atoms due to impurities on the surface can nullify the influence of incompletely filled d-bands. Thus, the sticking probability for the dissociative chemisorption of hydrogen molecules, which is close to unity on clean surfaces, drops to zero in the presence of even 0.5 monolayers of adsorbed species, suggesting that they increase the potential barrier for the process. On the other hand, the adsorption of hydrogen atoms is not influenced by these impurities.
- Atomic hydrogen requires only one empty site on the surface as opposed to two for the dissociative adsorption of molecular hydrogen. This removes the geometric requirement that two sites be within one hydrogen bond length of each other and that the approaching

hydrogen be aligned with these sites. This distinction, is however, only important for higher coverages of the membrane surface.

4.2 Experimental

High-purity hydrogen could be produced in our reactor by the use of the cathode or the anode as a metallic membrane. Hydrogen removal would also drive the reaction toward completion by removing one of the products and prevent reformation of H_2S. Further, the energy efficiency of the process would improve by preventing ineffective electron collision reactions, such as those with molecular hydrogen or H_2S that has previously decomposed but reformed by the reverse reaction. Unfortunately, the membrane development that was a key part of this project was unsuccessful.

4.2.1 Type 1 Thermal and Type 2 Super-permeable metal structure. Stainless steel, platinum-coated stainless steel, and niobium were used as cathode tube materials (thickness 0.5-0.7 mm) without any protective refractory sulfide coating. Methane decomposition experiments carried out with these cathode tubes showed no hydrogen permeation. The hydrogen concentration in methane decomposition experiments was as high as 40% and the reactor pressure was 12 psig. Hydrogen sulfide decomposition in these tubes also showed no hydrogen permeation.

4.2.2 Type 3 Metal infiltrated ceramic membrane. A 0.61 m long metal infiltrated ceramic membrane tube was fabricated by joining 4 0.15 m long porous alumina tube with average pore diameter of 200 nm. A vanadium coating on each of the 4 tubes was prepared by chemical vapor deposition (CVD) of vanadium oxytrichloride on the inside of the tubes, with hydrogen as the reductant, as shown in Figure 4.1.

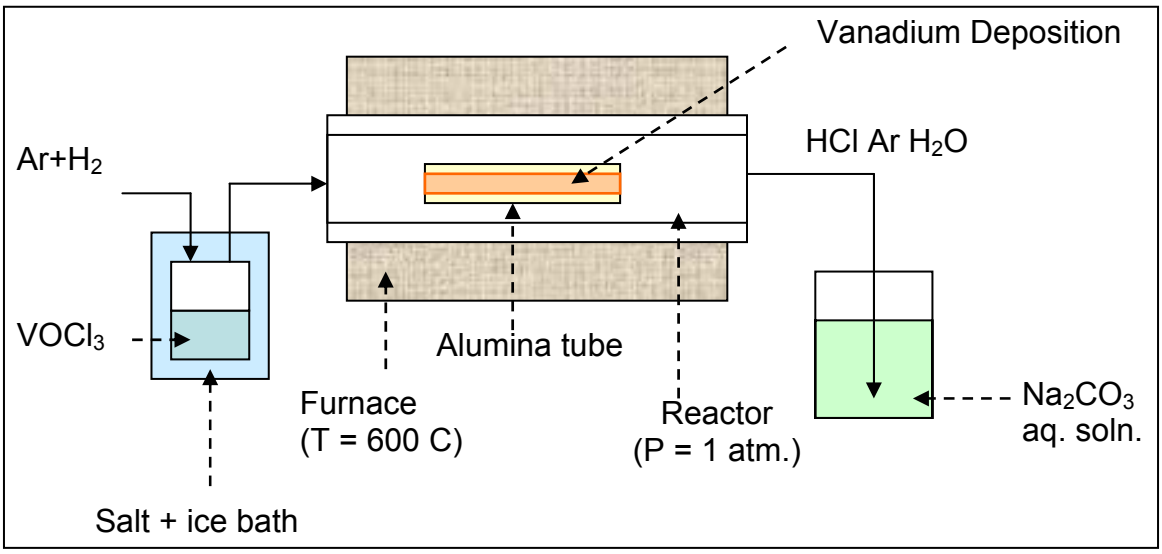

Figure 4.1. The chemical vapor deposition reactor

Initially, vanadium was deposited on silicon wafer to test the quality of deposition. The average deposition rate was 0.29 mg/cm^2·hr and X-ray diffraction analysis indicated presence of both V and V_2O_3. A similar deposition rate was obtained when a 2 cm diameter stainless steel tube was used as the substrate.

The tubes were prepared for CVD by ultrasonic cleaning in distilled water, which removed surface deposits of alumina powder and revealed cracks (manufacturing defects). The cracks were then sealed with an alumina-based adhesive, cured at high temperature, and checking for leakage. After repeating these steps until leaks could not be detected, the tubes were coated with vanadium for 2 h and checked for leakage with argon gas. If they failed the leak test, the chemical vapor deposition process was repeated again. Each tube underwent chemical vapor deposition for 8 h. They were then joined with the alumina-based adhesive and cured at high temperature. A picture of the resulting tube is shown in Figure 4.2. The silver gray areas are vanadium that has diffused completely through the tube. The dark gray and white areas are ceramic cement used to seal cracks and seams in the tubes.

Figure 4.2. Vanadium-infiltrated alumina membrane tube

4.3 Results and Discussion

With minor modifications to the reactor flanges and connections, this membrane tube was installed in the reactor. Initially, a corona discharge was not produced in the reactor. Apparently, the thin layer of ceramic cement joining the four sections together was sufficiently electrically insulating to prevent conduction of charge along this cathode. However, after installing a 0.005 m stainless steel wire as the cathode on the inside wall of the membrane tube, a corona was produced in pure H_2 in the reactor. N_2 flowing outside the membrane was used as the sweep gas. A steady presence of H_2 was detected in N_2 even without discharge, indicating a leak and no increase in H_2 permeation was found in the presence of discharge.

A mixture of Ar & H_2 was introduced through the inside of the cathode tube, with N_2 again used as a sweep gas outside the tube (on the shell side). Figure 4.3 compares the H_2 concentration in the tube side and the shell side. Again, the sweep gas contained H_2, even in absence of the corona discharge, indicating a selective leakage of H_2 through microscopic defects. The membrane tube was then heated to 339 K (66°C), but no significant change in enrichment was observed, indicating that selective leakage of H_2 and not molecular permeation was the dominant means of H_2 transport across the membrane.

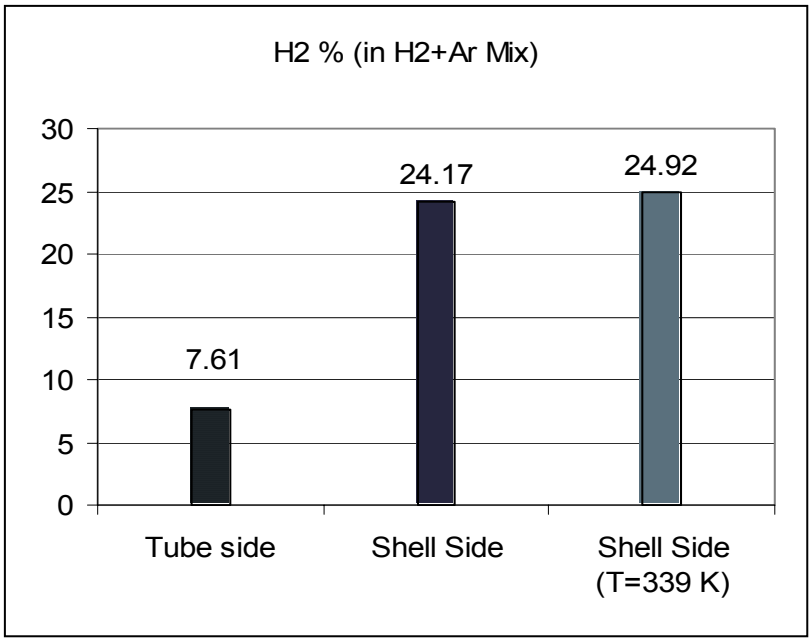

Figure 4.3. Hydrogen enrichment in vanadium-infiltrated alumina membrane tube

4.3.1 Plasma-driven permeation. Group V transition metals, notably niobium, vanadium, and to a lesser extent, tantalum, have been reported as superior membrane materials for plasma driven permeation, even exceeding palladium.[4] A test cell was fabricated to evaluate the superpermeable properties of these group V transition metal membranes. A schematic of the cell is shown in Figure 4.4.

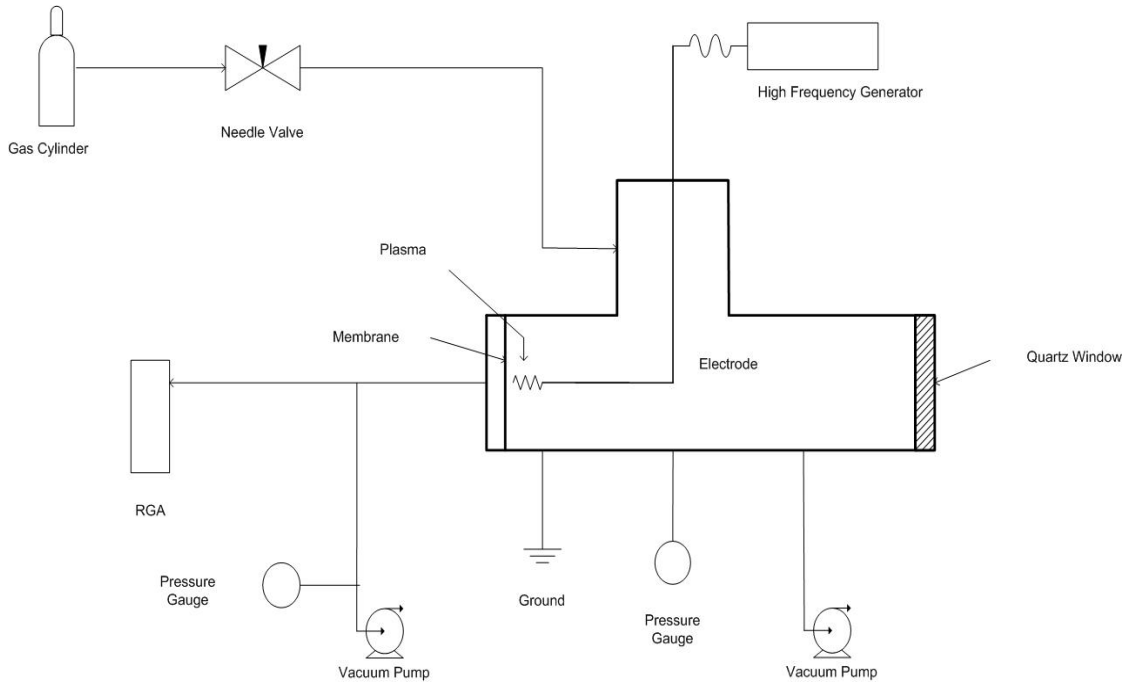

Figure 4.4. Test cell for evaluating plasma-driven permeation

The cell is 0.038 m in diameter with a flat metallic membrane as one electrode and a small sphere as the other electrode. The distance between the two electrodes was adjustable. A high frequency generator was used as a source of plasma. The plasma is a type of glow discharge in hydrogen gas at low pressure, which is why two vacuum pumps were used. The pressure inside the cell is still higher than the pressure on the permeate side of the membrane leading to the mass spectrometer analyzer (labeled as RGA in Figure 4.4), resulting in a net thermodynamic driving force for hydrogen permeation. Although the cell does not produce a pulsed corona discharge plasma, it still produced hydrogen atoms and permitted investigation of the superpermeability phenomenon.

For the vanadium and niobium membranes (150 μm thick), the upstream pressures ranged from about 1 torr to 900 torr and both glow and corona discharges (at higher pressures) could be seen. The pressure downstream of the membrane was maintained between 1 torr to 100

torr. Membrane temperatures of as high as about 773 K were achieved by wrapping a heating tape around the test cell. A thin tantalum membrane (3 μm thick) was tested at ambient temperature as well as at 430 K with the upstream pressure was about 4 torr, while the lowest downstream pressure was about 600 mtorr. However, no hydrogen permeation was detected during experiments with any of these foil membranes. Plasma-driven permeation has been reported at pressures up to only about 10 mtorr.[3]

4.3.2 Atomic hydrogen permeation. A resistively-heated tungsten filament was used to produce hydrogen atoms in hydrogen/argon mixtures at pressures between 4 torr and 7 torr near a vanadium membrane surface. The maximum filament temperature was calculated as about 2200 K as it failed at higher temperatures due to formation of tungsten oxide from leaked oxygen. The theoretical degree of hydrogen dissociation is between 4 and 5% at these pressures. Again, no hydrogen permeation was observed. Earlier work[4] with tungsten filaments as atomizers carried out at 30 mtorr reported superpermeation. This pressure could not be achieved with the vacuum pumps shown in Figure 4.5.

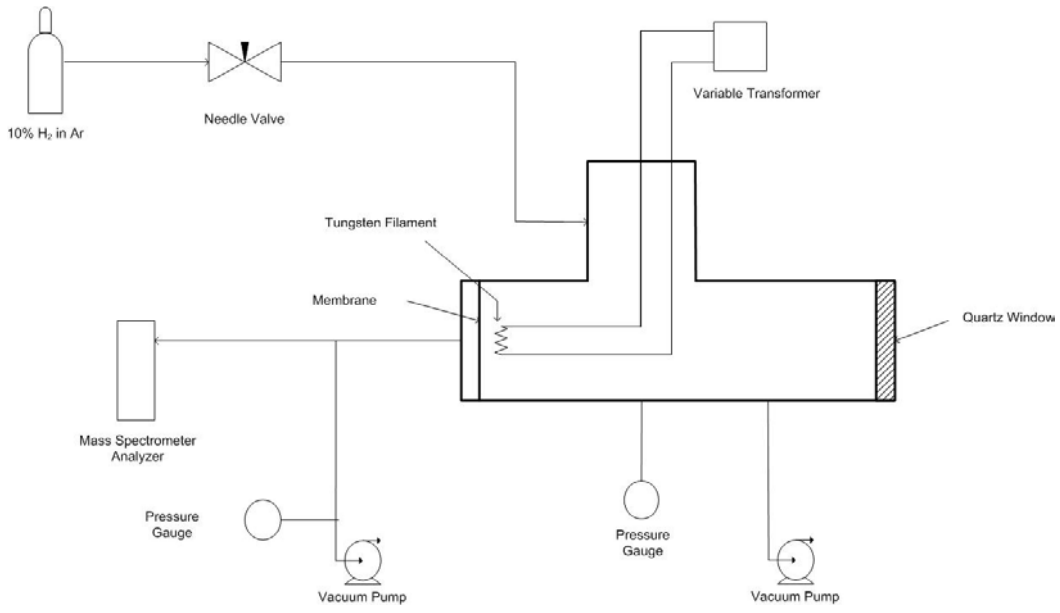

Figure 4.5. Test cell for evaluating atomic hydrogen permeation

4.3.3 Molecular hydrogen permeation. The same test cell was modified to test thermal molecular hydrogen permeation, in the absence of a plasma, as shown in Figure 4.6. The tantalum membrane was heated to 520 K with an upstream hydrogen pressure between 250 and1000 torr and a downstream pressure between 100-1000 torr. No molecular H_2 was detected permeating through the membrane at lower pressures, while at higher pressures both H_2 and Ar were seen indicating a leak through the membrane. The vanadium membrane was tested at 673 K with upstream pressure between 3 and 1000 torr and downstream pressure between 400-2000 mtorr. Again, the membrane failed at the sealing surface. Dilation of vanadium and palladium membranes due to absorption of hydrogen has been reported.[5] Absorption of hydrogen in palladium at temperatures lower than 573 K is known to cause an irreversible phase transformation.[6] Similar effects in these membranes may explain the lack of molecular permeation.

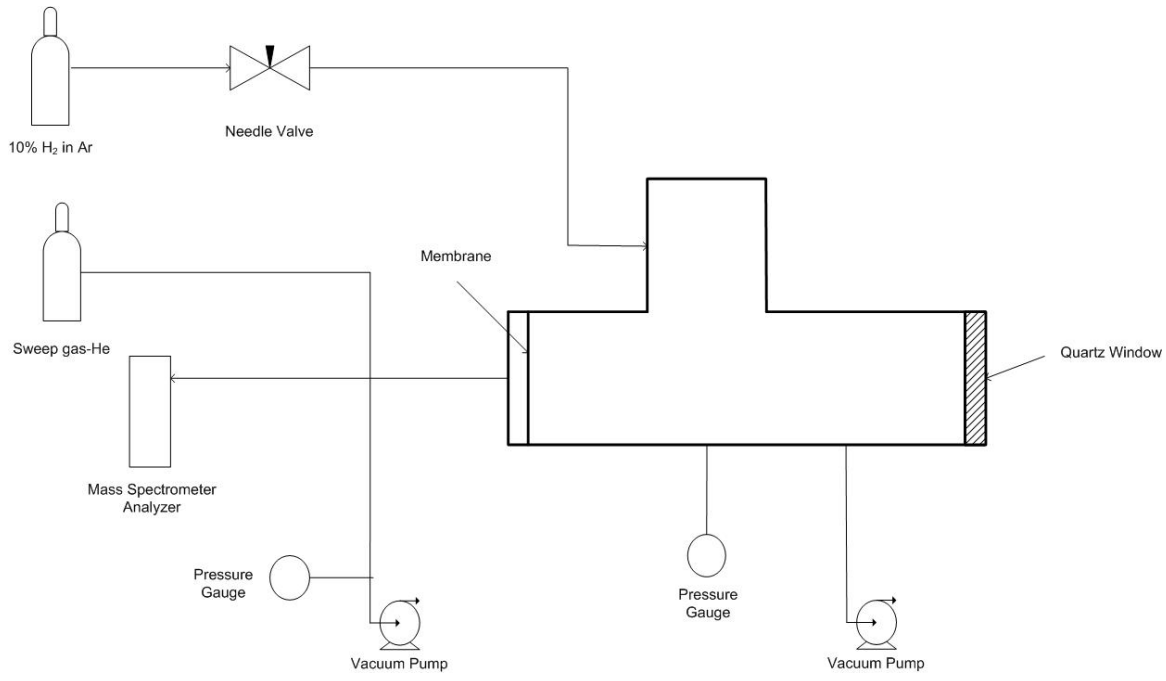

Figure 4.6. Test cell for evaluating molecular hydrogen permeation

4.3.4 Hydrogen atom recombination kinetics. In atomic permeation experiments using the resistively-heated tungsten filament, the theoretical degree of hydrogen dissociation was calculated to be 5% at a filament temperature of 2200 K and at a pressure of 7 torr. The feed gas mixture contained 10% H_2 and 90% Ar. Hence, about 5000 ppm of H atoms were estimated to be generated in the test cell.

For three-body reactions, the reaction rate can be expressed as

$$r_H = \frac{dC_H}{dt} = 2k \cdot C_H{}^2 C_M \tag{1}$$

where C_H is the concentration of atomic hydrogen in $mol \cdot cm^{-3}$; k is the rate constant in $cm^6 \cdot mol^{-1} \cdot s^{-1}$; C_M is the concentration of background gas in $mol \cdot cm^{-3}$; and t is time in seconds.

From Equation (1), we have

$$x = \frac{2k \cdot C_M \cdot C_H{}^0 \cdot t}{1 + 2k \cdot C_M \cdot C_H{}^0 \cdot t} \tag{2}$$

where x is the conversion of atomic hydrogen; $C_H{}^0$ is the initial concentration of atomic hydrogen in $mol \cdot cm^{-3}$.

For atomic hydrogen recombination reactions in the gas mixture with a major component of argon, k is about $6.5298 \times 10^{17}/T$ $cm^6 \cdot mol^{-2} \cdot s^{-1}$.[7] Assuming that the reaction occurs at 300 K and 7 torr, C_M is about 0.3366×10^{-6} $mol \cdot cm^{-3}$. Substituting k and C_M into Equation 2, we got

$$x = \frac{1.4653 \times 10^9 \cdot C_H{}^0 \cdot t}{1 + 1.4653 \times 10^9 \cdot C_H{}^0 \cdot t} = \frac{5.931 \times 10^4 \cdot C_H{}^{p0} \cdot t}{1 + 5.931 \times 10^4 \cdot C_H{}^{p0} \cdot t} \tag{3}$$

where $C_H{}^{p0}$ is the initial concentration of atomic hydrogen in ppm.

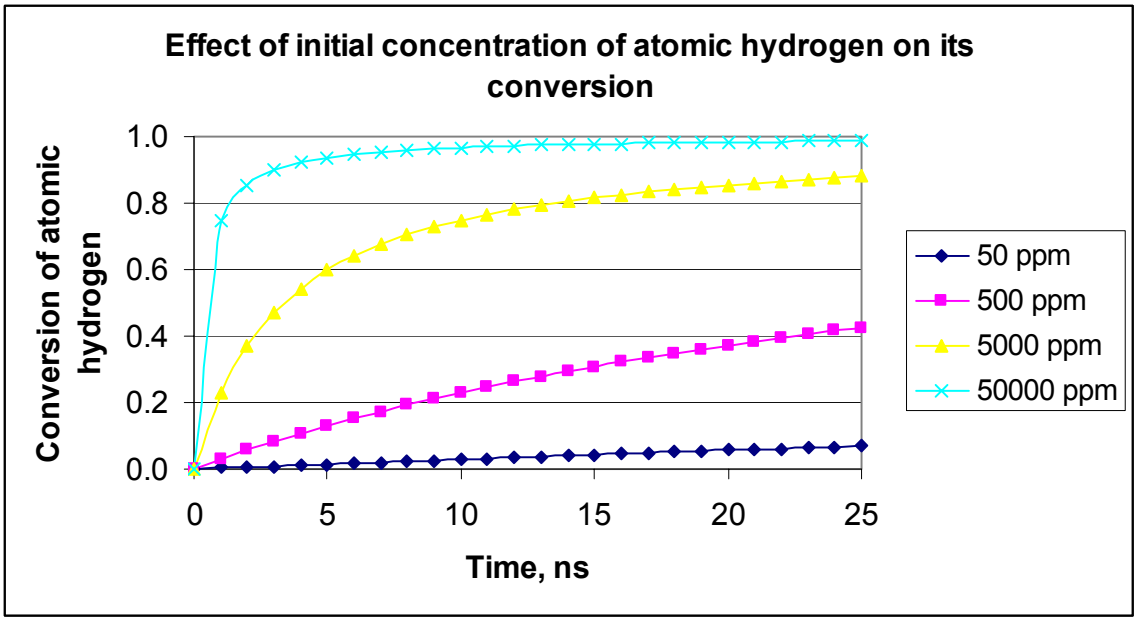

Figure 4.7. Atomic hydrogen recombination

As shown in Figure 4.7, higher atomic hydrogen concentrations lead to shorter lifetimes of the atomic hydrogen (or faster rates of conversion of atomic hydrogen back to molecular hydrogen). For 5000 ppm atomic hydrogen formed in the corona discharge, 80% can recombine in less than 15 ns. The atomic hydrogen recombination rate increases with atomic hydrogen concentration or partial pressure. The high hydrogen recombination rate at higher hydrogen partial pressures (for example upto about 5 psig in methane decomposition experiments) would not leave any atomic hydrogen available for superpermeation. Therefore, to reduce the time available for recombination, hydrogen atoms should be generated as close to the membrane as possible. The electric field is strongest near the anode and hence the concentration of radicals and excited species is also highest near the anode. By replacing the anode wire with a niobium membrane tube as shown in Figures 4.8 and 4.9, we hope to generate atomic hydrogen species close to the membrane. However, the probability for success remains low, due to moderately high pressures and short atomic hydrogen lifetimes that our experimental conditions dictate.

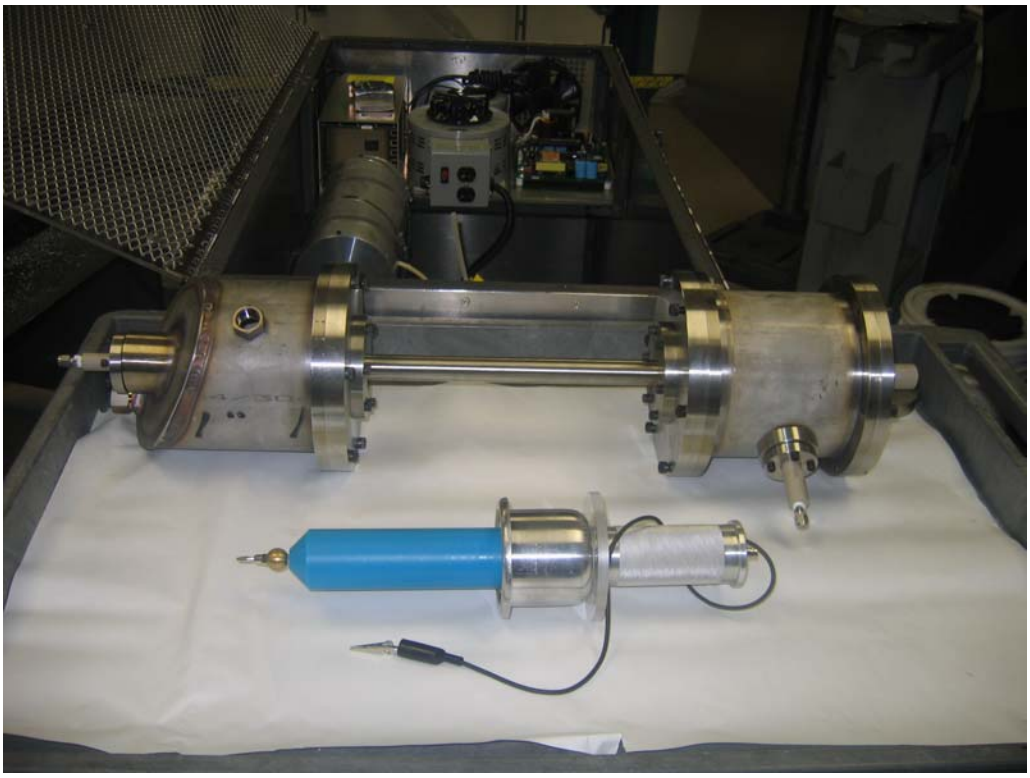

Figure 4.8. Reactor with the electrical components

Figure 4.9. Anode tube

4.4 Conclusions

Plasma-driven permeation, or superpermeability, was proposed as a key element of this research. However, no superpermeation was detected through a variety of experiments, as described in this section. The most likely explanation is that superpermeability cannot be achieved at pressures near atmospheric because the lifetime of atomic hydrogen is too short to permit significant numbers of H atoms to reach the surface of the membrane. A secondary effect may be the surface preparation of the membranes, which are generally specially cleaned using ion sputtering at high vacuum conditions. However, these conditions are not possible under the industrially relevant conditions of this study. A third generation reactor has been constructed, with the anode as the membrane, as a final effort to detect superpermeation, by creating the H atoms as close to the membrane surface as possible. This reactor was not complete as the project ended, but it will be tested and the results will be reported in the appropriate venue.

Acknowledgments

This work was supported by CITGO, the Department of Energy (DE-FC26-03NT41963) and the University of Wyoming Research Office. The authors acknowledge that the intellectual force that initiated the project was that of Professor Pradeep Agarwal, who passed away in September 2002. The guidance provided by Mr. Steve Fischer of CITGO is deeply appreciated. In addition, the authors gratefully acknowledge experimental assistance provided by Mr. R. Borgialli.

4.5 References:

1. Pick M. A., 1987. The dependence of the hydrogen concentration in metals on the surface of impurities. Journal of Nuclear Materials, 145-147, 297
2. Pick M. A.; Sonnenberg, K., 1985. A model for atomic hydrogen-metal interactions – Application to recycling, recombination and permeation. Journal of Nuclear Materials, 131, 208.
3. Busnyuk, A.; Nakamura, Y.; Nakahara, Y.; Suzuki, H.; Ohyabu, N.; Livshits, A., 2001. Membrane bias effects on plasma-driven permeation of hydrogen through niobium membrane. Journal of Nuclear Materials, 290-293, 57.
4. Livshits, A.; Ohyabu, N.; Notkin, M.; Alimov, V.; Suzuki, H.; Samartsev, A.; Solovyov, M.; Grigoriadi, A.; Glebovsky, A.; Busnyuk, A.; Doroshin, A.; Komatsu, K., 1997. Application of superpermeable membranes in fusion: The flux density problem and experimental progress. Journal of Nuclear Materials, 241-243, 1203.
5. Misako, U.; Kazuaki, M.; Naomi, K.; Hiroki, Y., 2006. Hydrogen Purification Technology-Development of Hydrogen Permeation Membrane. IHI Engineering Review, 39, 1, 40.
6. Philpott, J. E., 1985. Hydrogen Diffusion Technology- Commercial Applications of Palladium Membranes. Platinum Metals Review, 29, 12.
7. Baulch, D. L.; Cobos, C. J.; Cox, R. A.; Esser, C.; Frank, P.; Just, T.; Kerr, J. A.; Pilling, M. J.; Troe, J., 1992. Evaluated kinetic data for combustion modeling. J. Physical and Chemical Reference Data, 21, 411.